Electronic properties of metal-In_2O_3 interfaces

DISSERTATION

zur Erlangung des akademischen Grades
doctor rerum naturalium
(Dr. rer. nat.)
im Fach Physik
Spezialisierung: Experimentalphysik
eingereicht an der
Mathematisch-Naturwissenschaftlichen Fakultät
Humboldt-Universität zu Berlin

von
Frau M.Sc. Maryam Nazarzadehmoafi

Präsident der Humboldt-Universität zu Berlin:
Prof. Dr.–Ing. Dr. Sabine Kunst
Dekan der Mathematisch-Naturwissenschaftlichen Fakultät:
Prof. Dr. Elmar Kulke

Gutachter:
1. Prof. Dr. Recardo Manzke
2. Prof. W. Ted Masselink
3. Prof. James S. Speck

eingereicht am: 07.07.2016
Tag der mündlichen Prüfung: 22.02.2017

Zusammenfassung

Das Verhalten der elektronischen Eigenschaften von gespaltenen, aus der Schmelze gezüchteten In_2O_3-(111) Kristallen wurde bei Deposition von Edelmetallen, In und Sn mittels winkelaufgelöster Photoelektronen-Spektroskopie untersucht.
Die Stöchiometrie, strukturelle Qualität und Kristall-Orientierung, die Oberflächenmorphologie und die Elektronenkonzentration wurden jeweils mittels energiedispersiver Röntgenspektroskopie, Laue-Beugung, Raster Tunnel-Mikroskopie (STM) und Hall-Effekt untersucht. Die Ähnlichkeit der fundamentalen und Oberflächen-Bandlücken kann auf das fast flache Verhalten der Bänder auf der gespaltenen Oberfläche der Kristalle zurückgeführt werden. Die Grenzflächen von Ag und Au/In_2O_3 zeigen Schottky-Verhalten, während ein ohmscher in Cu, In und Sn /In_2O_3-Kontakten beobachtet wurde. Aufgrund der Übereinstimmung zwischen optischen und Oberflächen-Bandlücken, der Bildung eines Gleichrichterkontaktes und des Auftretens der Oberflächenphotospannung auf der frischen Kristalloberfläche kann gefolgert werden, dass SEAL nicht eine intrinsische Eigenschaft der gespaltenen Oberfläche der untersuchten Kristalle ist. Des Weiteren wurden bei dicker Au- und Cu-Beschichtung von In_2O_3 bei Raumtemperatur Shockley-artige Oberflächenzustände beobachtet. Zusätzlich wurde die erste Phase des Wachstums von Cu und In auf In_2O_3 von der Ausbildung eines 2-dimensionalen Elektrongases (2DEG) begleitet, welches bei dickeren Schichten verschwand, die von dem auf reinen Oberflächen von dünnen In_2O_3-Filmen gemessenen 2DEG verschieden sind. Nach Messung der Austrittarbeit von In_2O_3 und den jeweils untersuchten Metallen in situ und unter Verwendung der Schottky-Mott-Regel trat außer bei Ag/In_2O_3 eine deutliche Abweichung auf. Die experimentellen Ergebnisse stimmen auch mit fortgeschrittenen Theorien, die auf dem Elektronegativitätskonzept und MIGS–Modellen basieren, nicht überein.

Schlagwörter:
Transparente elektrisch leitfähige Oxide, Surface accumulation layer, winkelaufgelöster Photoelektronen-Spektroskopie, Metall-Halbleiter-Kontakte, Barrierenhöhe

Abstract

The behavior of the electronic properties of as-cleaved melt-grown In_2O_3 (111) single crystals was studied upon noble metals, In and Sn deposition using angle-resolved photoemission spectroscopy.

The stoichiometry, structural quality and crystal orientation, surface morphology, and the electron concentration were examined by energy dispersive X-ray spectroscopy, Laue diffraction, scanning tunneling microscopy (STM), and Hall-effect measurement, respectively. The similarity of the measured-fundamental and surface-band gaps reveals the nearly flat behavior of the bands at the as-cleaved surface of the crystals. Ag and Au/In_2O_3 interfaces show Schottky behavior, while an ohmic one was observed in Cu, In, and Sn/In_2O_3 contacts. From agreement of the bulk and surface band gaps, rectifying contact formation as well as the occurrence of photovoltage effect at the pristine surface of the crystals, it can be deduced that SEAL is not an intrinsic property of the as-cleaved surface of the studied crystals. Moreover, for thick Au and Cu overlayer regime at room temperature, Shockley-like surface states were observed. Additionally, the initial stage of Cu and In growth on In_2O_3 was accompanied by the formation of a two dimensional electron gas (2DEG) fading away for higher coverages which are not associated with the earlier-detected 2DEG at the surface of In_2O_3 thin films. The application of the Schottky-Mott rule, using in situ-measured work functions of In_2O_3 and the metals, showed a strong disagreement for all the interfaces except for Ag/In_2O_3. The experimental data also disagree with more advanced theories based on the electronegativity concept and metal-induced gap states models.

Keywords:

Transparent conductive oxides, Surface accumulation layer, Angle-resolved photoemission spectroscopy, Metal-semiconductor contacts, Barrier height

Acknowledgement

Joining to the scientific team of EES as a PhD student at the Humboldt University of Berlin was really appropriate opportunity to gain working experience in a scientific group together with different people from various backgrounds, and also provided me valuable experiences of studies. This doctoral work would have been possible unless the precious support of many people who helped me to shape up my academic career. I would like to extend my sincerest thanks and appreciation to those people.

First and foremost, I would like to express my sincere gratitude to my supervisor Prof. Dr. Recardo Manzke. He gave me the chance to work in his scientific group. He supported me academically and emotionally through the rough road to finish this thesis. I owe my deepest gratitude to him for his limitless patience, enthusiasm, and immense knowledge. His guidance helped me in all the time of research and accomplishment of this thesis. He cares a great deal about the welfare and success of every one of his group members, both professionally and personally. It is an honor for me to count myself amongst his students.

I am especially grateful to Dr. Mattia Mulazzi, advisor and mentor for my PhD study. I am indebted to him for the immeasurable amount of support, frequent and fruitful scientific discussions, motivation and guidance he has provided throughout this study. During these years, he also gave me the moral support and the freedom I needed to move on.

A very special appreciation and thanks to Dr. habil. Christoph Janowitz for numerous scientific discussions, which offered me new prospects during this study. Without his flexibility, genuine support, and encouragement, this thesis would not have been materialized.

It is a pleasure to convey my gratitude to people from Leibniz-Institut Kristallzüchtung. To Dr. Zbigniew Galazka for his high quality and purity melt-grown In_2O_3 single crystals which were grown from melt for the first time. To Dr. Klaus Irmscher for the Hall effect measurements.

I am very thankful to Prof. W. Ted Masselink (Humboldt University of Berlin) and Prof. Dr. James S. Speck (University of California) for referring this thesis.

Many thanks to Mrs. Dagmar Kaiser not only for her help in the chemistry laboratory but also her permanent assistance and care about me. It is difficult to put into words my gratitude to my former colleagues Dr. Helmut Dwelk and Dr. Mohamed Moustafa for their constant help and invaluable advice regarding my residence in Berlin. I acknowledge Mrs. Alica Krapf for fruitful discussions regarding chemical aspect of the results. I am thankful to Mr. Stephan Schmidt for the technical support.

I am grateful to B. Sc. Andreas Siebert for the STM measurements. I would like to thank Sharif University of Technology of Iran for assisting me to conduct the optical transmission measurements. I am thankful to Dr. Peter Schäfer for the EDX characterization of the samples. I thank Florian Neske who worked and joined me in this research.

This work has been, in part, conducted at the "Berliner Elektronenspeicherring-Gesellschaft für Synchrotronstrahlung'' (BESSY II). I would like to acknowledge the staff of BESSY, particularly Mr. Olaf Pawliski for the technical support. Thanks to Dipl.-Phys. Valentina Scherer, Florian Titze and Stephan Machulik for their kind support during ARPES measurements at BESSY. I am grateful to Jürgen Sölle for his contribution in the crystal preparation. I would like to thank honorary all my present and former colleagues in the research group. This work was financially supported by the DFG (German Research Foundation) under Project No. MA2371/8-1. This work would not have been possible without the financial assistance of Komission für Frauenförderung of Humboldt University and the Caroline von Humboldt scholarship. Therefore, I would like to express my sincere gratitude for their help.

Last but not least, many thanks to whole of my family. I would like to thank my parents and my siblings for making me who I am. Special recognition goes out to my lovely husband, i.e. my best friend for his constant support, encouragement, and endurance during my pursuit of the PhD. I could not have completed this journey without him by my side.

Table of contents

Chapter 1
Introduction

Semiconductor materials are the cornerstone of state-of-the-art technology, as they are the building blocks of essentially any electronic device, such as transistors, power devices, solar cells, and light emitting diodes (LEDs). Researchers have introduced a new class of semiconductors, transparent conductive oxides (TCOs) e.g. ZnO, Ga_2O_3 and In_2O_3, which are promising alternatives for conventional semiconductors like Si, GaAs and GaN notably for application in transparent electronic and high-power devices. Despite the growing number of their practical applications in solar cells and flat panel displays [1, 2] due to their simultaneous high electrical conductivity and visual transparency, the full understanding of the origin of this peculiar combination is still lacking. One of the main reasons hindering the use of TCOs as active components in electronic devices is their application in amorphous or poly-crystalline form to reduce production costs. Therefore, high quality and purity single-crystals with well-defined contact properties are interesting from the fundamental point of view to gain insight into the origin of the conduction and improve the device performance. Various fundamental properties for many members of the TCO family, especially In_2O_3 are still controversially discussed. For instance, it has recently been reported that the fundamental band gap of In_2O_3 is around 1 eV smaller [3-5] than the commonly quoted-band gap of 3.75 eV [6]. The other crucial issue for In_2O_3 is the identification of a near-E_F state, which is usually ascribed to the pronounced downward band bending and consequently to the surface electron accumulation layer (SEAL) in In_2O_3 thin films [7-10]. Moreover, observation of the three dimensional character of the near-E_F emission at as-cleaved surface of CVT-grown In_2O_3 bulk single crystals contradicts the presence of an accumulation layer at the surface of this material [5]. Whether the origin of the SEAL

is either intrinsic or extrinsic due to surface defects [11, 12], adsorbates and impurities in growth ambient [13], or to the particular sample preparation and processing [14] is still an unsolved question. Although this behavior is favorable for ohmic contact formation, rectifying contacts are also necessary for space-charge region based characterization and device applications like field-effect transistors and Schottky diodes. Thus, the challenge of the Schottky contact formation on this material has brought significant attention towards studies of metal-In_2O_3 contacts. Different groups investigated the formation of contacts and characterized them. For example, Bierwagen et al. [10] observed the formation of a non-ideal Hg/In_2O_3 Schottky contact on In_2O_3 thin films by oxygen plasma treatment. In a more recent work von Wenckstern et al. [15] succeeded to form Pt, Pd, and Au Schottky contacts on undoped and Mg and Sn doped In_2O_3 thin films with the help of a reactive sputtering process in an O_2/Ar atmosphere. Therefore, they concluded such treatments likely remove the oxygen vacancies and subsequently the SEAL [10, 15].

Furthermore, the study of metal-TCOs interfaces and their optimization according to the desired applications have recently become the focus of research with the advent of additional novel transparent electronic and optoelectronic devices, such as last generation of light emitting diodes, gas sensors, field effect transistors, spintronic devices, and UV photodetectors [1, 16-20].The metal-semiconductor contacts and their barrier heights are commonly measured by I-V and C-V characteristic which do not provide information about the different stages of the interface evolution. On the other hand, thanks to angle-resolved photoemission spectroscopy (ARPES), one can obtain information of the electronic properties of the contact during the growth of a metal on the semiconductor at the microscopic level. Such experiments additionally can spur and help theorists to improve and refine the available theoretical approaches, which are not usually capable to predict barrier heights on transparent conductive oxides [15, 21].

This work is a comprehensive study of the electronic properties of metal-In_2O_3 (111) interfaces by stepwise metal (Ag, Au, Cu, Sn, and In) deposition on the ultra-high vacuum cleaved (111) surface of melt-grown In_2O_3 single crystals, followed by ARPES experiments [22, 23].

In the second chapter, at first a review on the properties of the TCO material class is presented, followed by a list of the models used to interpret the origin of the electrical conduction, and the optical properties. At the end of Chapter 2, the structural properties of In_2O_3 are given. A brief introductory to the innovative method by which the melt-grown single crystals were grown as well as their characterization is outlined in third chapter. Chapter 4 is devoted to the results of the Hall-effect measurements and optical transmission properties of the crystals which are under study in the present thesis. Chapter 5 focusses on the principle of ARPES technique and the general introduction of the theoretical aspects of this method, and the experimental ARPES setup used for this work and the sample preparation. Chapter 6 presents an overview on the electronic properties and SEAL in In_2O_3, and it is followed by the discussion about the experimental In 4d semi-core level spectra as well as valence band. The introductory remarks on the Schottky-Mott rule and the metal induced gap states (MIGS)-based model, the details of the metal/In_2O_3 interfaces and the comparison of the experimental results and the aforementioned rule and theoretical model are given in Chapter 7. Lastly, the conclusion is presented in Chapter 8.

Chapter 2
Transparent conductive oxides (TCOs)

2.1 Introduction

Transparent conductive oxides (TCOs) are an exceptional class of materials exhibiting properties, which basing on simple argument, should mutually forbid each other, i.e. high electrical conductivity and transparency in visible light range. It is known that conventional wide band gap semiconductors are insulator, while conductors are visually opaque. An insulator, in other words a material with filled valence band and empty conduction band, shows transparency. On the other hand, high electrical conductivity requires that the Fermi level lies within the band with high concentration. Therefore, this family is an exception of this rule. However, transparent conducting materials include not only TCOs but also extremely thin films of metals [24-27], carbon nanotubes [28], and graphene [29].

Multifunctional properties of oxide-based materials, such as high mobility [30], ferroelectricity, ferromagnetic behavior [31], superconductivity, reveal their potential for electronic device applications [32]. TCOs consist of binary compounds, such as In_2O_3, Ga_2O_3, SnO_2, TiO_2, and ZnO, ternary compounds like Cd_2SnO_4, $CdIn_2O_4$, and $MgIn_2O_4$, and multi compounds, such as $Zn_2In_2O_5$-$MgIn_2O_4$, and In_2O_3-Ga_2O_3-ZnO [33]. Metal oxides possess a wide band gap of at least 3 eV which causes low absorption in the visible range. This class of materials is made of rather large metal cations with electron configuration of (n-1) d^{10} ns^0 ($n \geq 4$) and small oxygen anions [34]. It is generally known that the size mismatch of their heavy metal cations (HMCs) and oxygen anions leads to the importance of the O-vacancies in their conductivity [35].

The performance of the metal oxides is associated with the electron behavior in their valence and conduction bands [36, 37]. The maximum of their valence band (VBM) is predominantly composed of O 2p states, while the conduction band minimum (CBM) is typically derived from the metal s band leading to ionic bonding [32]. The large band gap of TCOs, therefore, originates from deep lying O 2p states of their valence band (VB). VB states are identified by their small dispersion, large effective masses, and high density of states [38]. As the conduction band (CB) of these materials arises from metal states, they show electron-related properties depending on the metallic component of the compound. TCOs are mainly n-type because the O-vacancies and cation interstitials can easily form in the oxides [32] and causing concerns about the possibility to obtain p-type TCOs.

The aim of this chapter is to provide an overview of the applications and the fundamental properties of TCOs, especially of In_2O_3.

2.2 Applications

Simultaneous visual transparency and high electrical conductivity were observed for the first time in CdO in 1907 [39]. Over half a century, ZnO, Sn-doped In_2O_3 (ITO), In_2O_3 and SnO_2 had wide range of applications as transparent conducting oxides. However, the rate of TCOs discovery increased dramatically after 1995 [32]. As depicted in Figure 2.1, many of the late- and post-transition metals oxides exhibit this unique behavior.

TCOs like ZnO, In_2O_3, Ga_2O_3 and SnO_2 are widely applied materials in electronics and optoelectronics, such as window layers of solar cells, electrodes for displays, organic light emitting diodes (OLEDs), and thin film transistors [1, 2, 42]. The most popular TCO, which has a widespread of applications especially in display technology, is Sn-doped In_2O_3.

The energy consumption and demand drastically increased in the last decades as a result of a global industrial development, which led to a serious increase in the atmospheric CO_2 levels. As high levels of CO_2 induce strong climate changes, it has been understood that industrialization must be sustainable, i.e. the consumption of energy and materials must lie within the limits of the natural resources regeneration. In this context, TCOs are

crucial components of a number of ''green'' technologies like for the above-mentioned applications and also novel transparent electronics, such as oxide-based transistors and new flexible and smart devices, e.g. smart phones, touch-panel displays.

Oxide based thin films transistors (TFTs) are one of the potential candidates for new class of transparent electronics and possible alternative to amorphous Si-TFTs which are vastly applied in flat panel displays because of their high mobility and lower production costs.

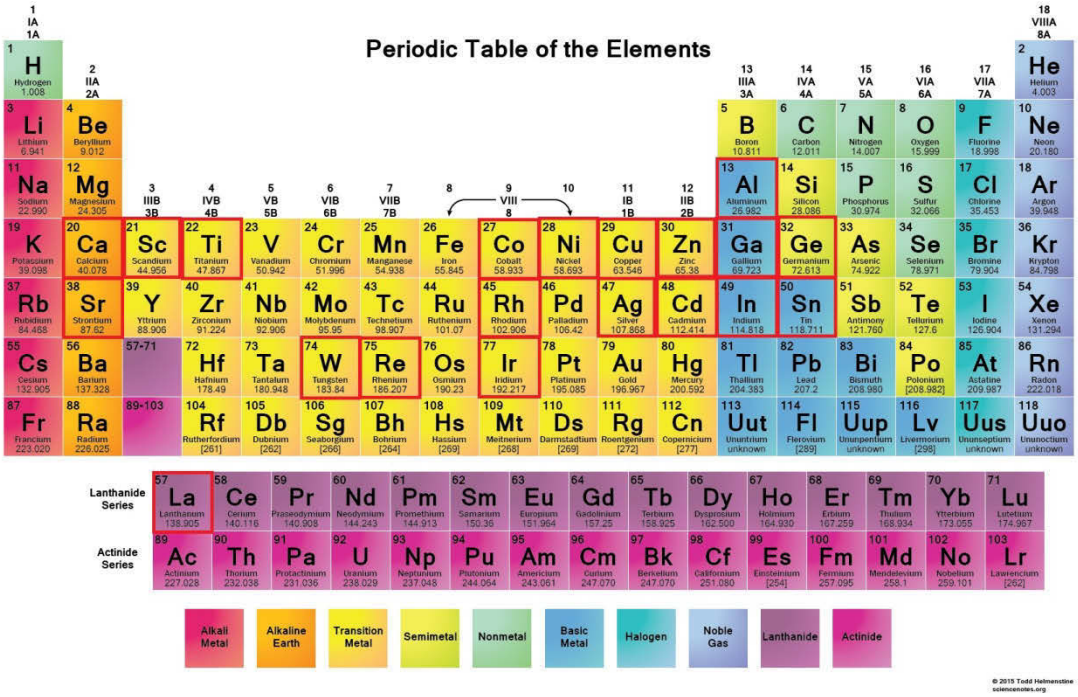

Figure 2.1: Periodic table with associated elements as cations in transparent conductive oxides compounds, marked with red box. From Ref. [32].

TFTs based on oxides consist of conducting TCOs and amorphous semi-insulating high mobility TCOs [32].

In addition, it is essential and difficult to tune and optimize TCOs' contradicting properties for any desirable application. So, it is another reason which drives researchers to study this family.

2.3 Electrical conductivity of TCOs

TCOs are among the wide band-gap materials, exceeding 3 eV, with the brightest application spectrum. These materials are electrically conductive with conductivity σ in the range of 10^2 to 10^6 S. The conductivity is given by

$$\sigma = ne\mu \tag{2.1}$$

where n, e, and μ ($e\tau/m^*$, τ is relaxation time and m^* effective mass of charge carrier) are the charge density, electron charge, and the mobility of charge carriers, respectively. Their conductivity is limited by the interdependence of charge carrier density and mobility. Electron scattering at ionized impurities limits the carrier transport and reduces the mobility at higher electron concentration, and it also limits their attainable concentration. Therefore, higher doping levels will not increase the carrier concentration, but will lead to a lower optical transmission in the near-infrared region [43]. Additionally, higher doping can result in dopants clustering and consequently higher scattering rate [44] and to a non-parabolic conduction band minimum [45].

Moreover, this category of materials generally exhibits intrinsically n-type conductivity, in other words they are unintentionally doped (UID). Semiconductor industry demands to control and optimize TCOs' conductivity in line with desirable device performance. However, the origin of their conductivity is still vague despite the intense scientific efforts.

2.3.1 Potential origin of the n-type conductivity in TCOs

As mentioned above, semiconducting oxides are commonly n-type and the source of their high unintentionally electron concentration remains unclear. The electron-hole generation in their VB is probably impeded by their intrinsic compensating centers and consequently limiting their obtainable carrier concentration [44]. Therefore, the Fermi level lies close to the CBM [45-49]. However, there might be other possibilities that must be considered to clarify the size of the conductivity. One of them could be the well-known contribution of impurities coming from the growth environment (like crucible or transport gas). For instance, hydrogen is ubiquitous in the growth atmosphere and acts as compensating acceptor in n-type semiconductors [35]. On the other hand,

several theoretical and experimental studies demonstrated that the shallow donor nature of hydrogen in conducting oxides, such as ZnO [50-54], In_2O_3 and SnO_2 [55, 56], CdO [57], and Ga_2O_3 [58]. For example, observation of high UID concentration in In_2O_3 films which were sputtered in water-containing atmosphere [59, 60], as well as increase of electron concentration of In_2O_3 single crystals after annealing in hydrogen [61] reveal that hydrogen behaves as a donor . Even in the absence of H, TCOs show high conductivity, so H cannot be the dominant factor controlling their n-type conductivity. Presence of other impurities like Iodine in chemical vapor transport [5] or Mg and Pb in the ambient during In_2O_3 growth could influence the conductivity [13]. However, high-quality single crystals also show intrinsic n-type conductivity. Figure 2.2 demonstrates a summary of the electron concentration and mobility of high-quality In_2O_3 single crystals. Besides the ionized impurity scattering, other scattering mechanisms, e.g. phonon scattering impact on the carrier mobility [62].

In addition to the concentration of impurities from growth environment, native defects are known to involve in UID electron concentration of this class of materials.

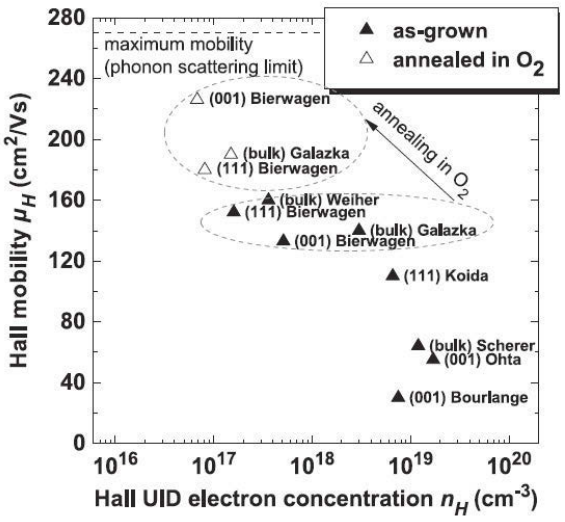

Figure 2.2: Summary of the Hall mobility and electron concentration of UID In_2O_3 single crystalline bulks and thin films. Figure adopted from Ref. [63].

Their common native defects are as follows [35]:

1- Oxygen vacancies (V_O)
2- Cation interstitials
3- Cation vacancies

4- Oxygen interstitial (O_i)

5- Defect complexes

Thanks to the theoretical calculation of the defect formation energies and charge transition levels within the frame work of density functional theory (DFT), much information about point defects was gained. However, because of methodological issues, i.e. the application of different corrections for supercell errors, these calculations posed new problems. Intrinsic donor defect V_O was found to be located below the conduction band minimum, which cannot have contribution to the conduction and creating high electron concentration of oxides [56, 64-67]. This theoretical finding is consistent with the optical-measurement results of Evans et al. [68] as well as the electron paramagnetic resonance (EPR) data of Vlasenko et al. [69]. Fig. 2.3 shows the Fermi level dependence (E_F) of the calculated defect-formation energy for native and extrinsic donor defects (Sn_{In} in In_2O_3 and Al_{Zn} in ZnO) under metal (here In and Zn) and oxygen-rich conditions by Lany et al. [66]. As depicted in this figure, none of the intrinsic point defects can produce the high electron densities of ZnO and In_2O_3. For example, it displays that V_O is a deep donor, and cannot contribute to conductivity under equilibrium conditions. Lany et al. also proposed that the neutral V_O^0 has a deep and non-conductive state in contrast to the excited V_O which has a metastable shallow state, and the excited V_O can cause photoconductivity. Thus, they concluded that this model can explain the contradicting coexistence of transparency and high electrical conductivity [66]. It is noteworthy that for this interpretation to hold, a band-gap value of 3.5 eV for In_2O_3 needed to be used, while its fundamental band gap was found to be around 2.7-2.9 eV by optical measurements [3, 4, 69, 70], angle resolved photoemission spectroscopy (ARPES) [5], and X-ray photoelectron spectroscopy (XPS) [71]. We stress that no experimental evidence for this theory has been found to date.

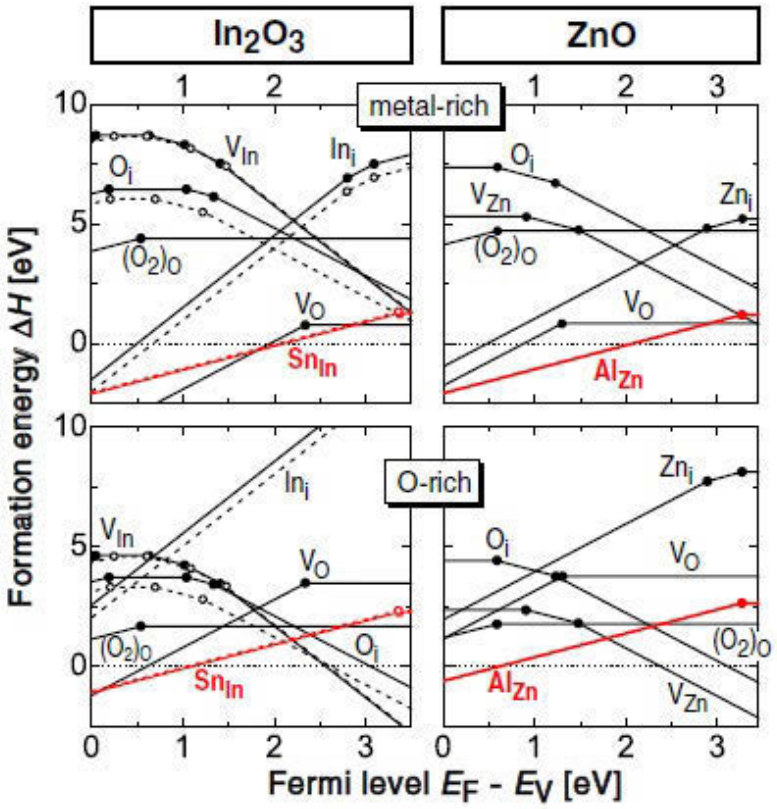

Figure 2.3: Dependence of calculated defect-formation energy with Fermi level for In_2O_3 and ZnO for metal and oxygen-rich conditions [66].

On the other hand, the DFT studies with generalized-gradient approximation (GGA) of Agoston et al. on indium oxide showed that the intrinsic donor oxygen vacancies and also interstitial indium defects are shallow, and they can contribute to the n-type conductivity. The reason is that positive charge states are favorable for Fermi energies within the gap. They also identified that V_O should be the major responsible for n-type conductivity of In_2O_3 due to its low formation energy [72]. In addition, a theoretical approach suggested that the shallow donor level can be because of the complex formation of multiple point defects [73]. By hybrid functional calculation, Varley et al. [38] also realized that self-trapped holes (STH) formation (localized small polarons are energetically more favorable than delocalized holes in oxides) prevents p-type conductivity in oxides even in the absence of compensating centers. The relaxed configuration of the STH in some oxides is illustrated in Fig. 2.4.

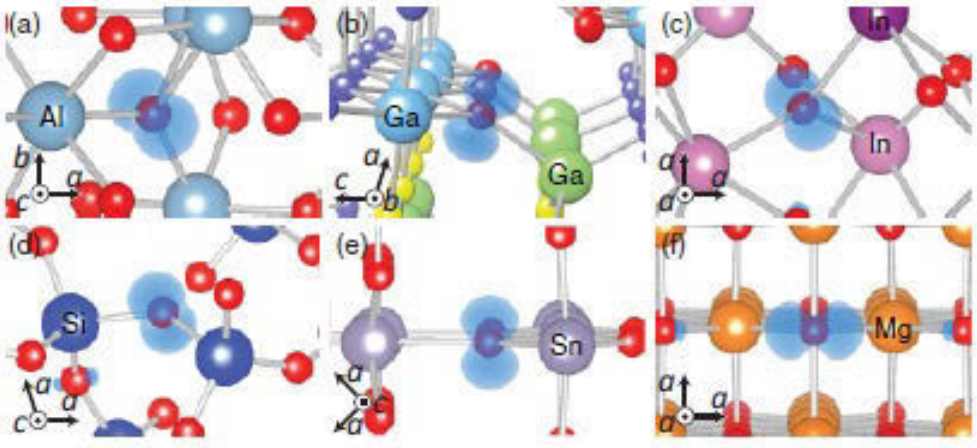

Figure 2.4: Relaxed configuration of the self-trapped holes in a set of oxides a) α-Al_2O_3, b) β-Ga_2O_3, c) bcc-In_2O_3, d) α-SiO_2, e) rutile SnO_2, and f) MgO. The symmetrically inequivalent sites of gallium and oxygen in β-Ga_2O_3 and indium in bcc-In_2O_3 are depicted with different colors. The polaron wave function is shown by the charge density isosurfaces at 10% of their maximum value [38].

There are also several paradoxical experimental results: on the one hand, some studies show the quantity of oxygen vacancies V_O is very low in as-grown ZnO, and it was induced after particle irradiation [69, 74]. On the other hand, the following observations confirm the contribution of this native defect to the conductivity of oxides:

- The presence of V_O in ZnO without particle irradiation [75]
- High quantity of oxygen vacancies in In_2O_3 as well as SnO_2 poly-crystals [76, 77]
- An increase in electron concentration with decreasing oxygen pressure in In_2O_3 films [78]
- A drop of V_O after annealing in oxidizing condition at elevated temperature in In_2O_3 bulk single crystals [61]

Cation interstitials, as donor-like defects, are also suggested to be a likely source of n-type conductivity by theoretical and experimental findings. For example, Interstitial Sn in SnO_2 [79] and Zn in ZnO [80] are theoretically found to be the possible cause of the conductivity in this category of materials. However, later theoretical results showed that the above-mentioned interstitials may be unstable centers due to their high formation energies and the low energy barrier for migration [5, 81-83]. Rapid diffusion of Zn in ZnO, which was observed by secondary ion mass spectroscopy [84], confirms instability

of these centers. Although intrinsic acceptor defects, i.e. cation vacancies and oxygen interstitials do not contribute to n-type conductivity, they serve as compensating centers and limit TCOs electron concentration. By positron annihilation spectroscopy, it was realized that cation vacancy is the major compensating center in as-grown and electron-irradiated ZnO films [74, 85] as well as in Mg and Sn-doped In_2O_3 single crystal thin films after oxygen annealing [86]. The possible role of the defect complexes is not clear due to complexity of their identification. It was pointed out that the interaction between V_O and cation interstitial in ZnO [87] and also In_2O_3 [73] reduces the energy formation, and make these complexes play a possible role in the conductivity. Likewise, it was reported in SnO_2 that V_O and Sn complexes can be responsible for n-type conductivity [88, 35].

2.4 Optical properties of TCOs

The optical transmission and electrical conductivity are interconnected in this material class, and the optical transparency window usually becomes narrower for higher concentration. Therefore, these properties need to be set and controlled depending on the function the material must perform. An ideal transparent material possesses low absorption in near ultraviolet (UV), visible and near infrared (NIR) region. Different types of optical absorption like fundamental absorption, impurity absorption, free carrier absorption, intraband transitions, exciton absorption, and donor–acceptor transitions can occur in a semiconductor [33].

The absorption coefficient α (in the case of the fundamental absorption mechanism involving a direct transition from the valence to the conduction band) for $E>E_g$, i.e. $\lambda<\lambda_g$ is expressed by:

$$\alpha(E) = \frac{A}{E}(\mathrm{E} - E_g)^{\frac{1}{2}} \tag{2.2}$$

where E, E_g, and A are photon energy, band gap energy and a proportionality constant [33]. The transmission is limited in the near UV by E_g because the photons with energy higher than the energy band gap of TCOs will be absorbed.

For heavily doped semiconductors, the Fermi level is located within the conduction band with the lowest-lying states of CBM being populated. This is the case of a degenerate semiconductor. According to the Mott's criterion [89, 90] degeneracy is reached at a critical carrier density n_C at densities higher of which the lowest states of CBM start to be filled. n_C is given by [89, 90]

$$n_C^{\frac{1}{3}} a_H^* = 0.25 \tag{2.3}$$

In this equation, aH* is the mean ground state Bohr radius. The photon energy should be higher than fundamental band gap (Eg0) in order to excite an electron from VB to CB. Upon higher concentration, UV absorption edge will be pushed to higher energy as a result of the shift of the Fermi energy to higher energy and accordingly population of the states close to the CB. This shift of the edge is called Burstein-Moss (B-M) effect (ΔE_g^{BM}), and it is defined by [91]

$$\Delta E_g^{BM} = \frac{\hbar^2 k_F^2}{2m_{vc}^*} = \left(\frac{h^2}{2m_{vc}^*}\right)\left(\frac{3n}{8\pi}\right)^{\frac{2}{3}} \tag{2.4}$$

where k_F, m_{vc}^* are the Fermi wave vector, and reduced effective mass. m_{vc}^* is derived from valence band and conduction band effective masses m_v^* and m_c^* by the equation $((m_{vc}^*)^{-1}=(m_v^*)^{-1}+(m_c^*)^{-1})$. So, the optical band gap will be written [92]

$$E_g = E_{g0} + \Delta E_g^{BM} \tag{2.5}$$

Fig. 2.5 illustrates the schematic parabolic bands of a TCO and fundamental gap E_{g0} and the vertical optical transition, indicating the optical gap is enlarged by the B-M shift for high enough concentration [33]. However, the measured band gap shift is generally lower than predicted one by equation (2.4) because of a competing mechanism called band-gap shrinkage [6, 93, 94].

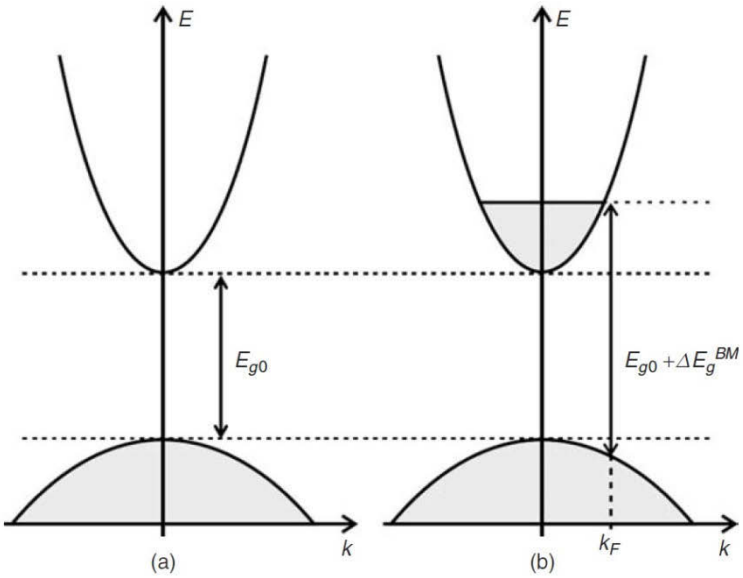

Figure 2.5: The schematic parabolic valence and conduction bands of a TCO with fundamental gap E_{g0} and the vertical optical transition, also showing the broadening of the optical gap of a highly doped TCO by Burstein-Moss shift due to the occupation of the lowest states of the conduction band [33].

The band gap renormalization model [6, 94] calculates that the band-gap shrinkage (Δ_{RN}) occurs because the valence band maximum (VBM) increases and CBM decreases as a result of the electron-impurity scattering and also the Coulomb interaction between the electrons filling the CB. Thus, then the net band gap change will be $\Delta E_g = \Delta E_g^{BM} - \Delta_{RN}$ (see Fig. 2.6).

At higher wavelengths, NIR region, the optical transmittance is limited by reflection at plasma frequency. Application of the Drude model leads to the following equation for the frequency-dependent conductivity

$$\sigma(\omega) = \varepsilon_0 \varepsilon_\infty {\omega_p}^2 \tau \frac{1+i\omega\tau}{1+\omega^2\tau^2} \tag{2.6}$$

here ε_0, ε_∞, ω are vacuum permittivity, high-frequency, and angular frequency of a time-dependent electric field, respectively. ω_p is the plasmon frequency and is given by the following expression [95]:

$$\omega_p = \left(\frac{ne^2}{\varepsilon_0 \varepsilon_\infty m_e^*}\right)^{\frac{1}{2}} \tag{2.7}$$

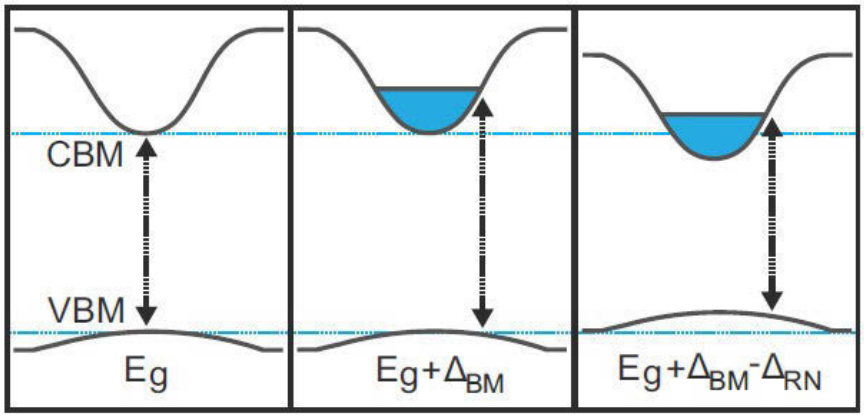

Figure 2.6: The effect of charge carriers on optical transition from valence band to conduction band for highly doped semiconductor. The band gap is reduced by Δ_{RN} [96].

In this equation, n and m_e^* are free-electron concentration of the semiconductor and effective mass. The plasma-wave length $\lambda_p=(2\pi c/\omega_p)$. Heavy doping causes the narrowing of the transparency window due to the increasing of the plasma frequency, which is not desirable for some of the applications, such as solar cell transparent contacts. Thus, the optical window of TCOs is set to these boundaries λ_p and λ_g, as schematically depicted in Figure 2.7.

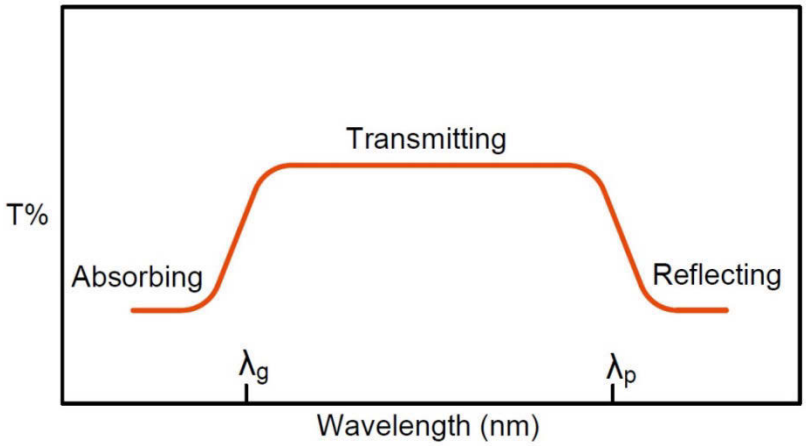

Figure 2.7: Schematic image of the wave length dependence of optical transmittance of a TCO and its boundaries at λ_g and λ_p. From [97].

2.5 n-type In_2O_3

In_2O_3 (indium sesquioxide) is a prototypical and technologically important member of the transparent conductive oxides. Low-quality materials are usually used for typical applications as transparent conductive oxide contacts in order to decrease synthesize costs. However, indium sesquioxide has a potential to be applied in transparent electronics devices in the form of single-crystalline material. Some technological steps are however necessary in order to obtain In_2O_3 single-crystals of the same quality, purity and controlled carrier concentration in as GaAs and GaN [10].

Although n-type resistivity of this material is altered by 9 orders of magnitude upon donor and acceptor doping, no evidence of p-type conductivity has been observed in this compound so far [62]. Despite the still lacking p-type conductivity, the conductivity is tunable upon exposure to oxidizing and reducing conditions, making In_2O_3 an attractive material chemical gas sensing applications [98-101].

In_2O_3 mostly crystallizes in the stable body centered cubic bixbyite structure with space group $Ia\bar{3}$, which is the subject of the present work. The other In_2O_3 polytype is rhombohedral corundum structure with space group $R\bar{3}c$. The latter crystal structure is metastable, but it can found in nanostructures or be epitaxially grown on the c-plane of sapphire in special conditions [62, 95]. Low quality materials, deposited as amorphous and polycrystalline thin layers or thick films, are commonly prepared by laser ablation, magnetron sputtering, and pressing pellets [33, 13]. The lack of high quality crystals hindered understanding of the fundamental properties of In_2O_3 for decades. The main obstacles of TCOs growth are their instability at elevated temperature as well as their high melting point [22]. High quality bulk single crystal and thin films were epitaxially grown by different growth techniques, e.g. molecular beam epitaxy (MBE) [22, 102-104], metal-organic chemical vapor deposition (MOCVD) [105], pulsed laser deposition (PLD) [106] and chemical vapor transport (CVT) [5]. Very high oxygen decomposition pressure impedes the growth of some of the oxides, such as In_2O_3, from melt. By means of the state-of art and innovative growth technique, called Levitation-Assisted Self-Seeding Crystal Growth Method, cooperation partners at the Leibniz Institute for Crystal Growth (Leibniz-Institut für Kristallzüchtung, IKZ) successfully overcame this problem and grew high-quality bulk single-crystals from the melt [22, 23]. In addition, the size of

the obtained samples is large enough to be used as the substrate in applications. In this thesis, these high-quality melt-grown bulk single-crystals were applied.

2.5.1 Crystal structure

As mentioned above, In_2O_3 crystallizes in two different polymorphs: rhombohedral and bcc bixbyite structures (see Fig. 2.8). The meta-stable rhombohedral structure can be characterized by a hexagonal unit cell with a=b=5.476 Å and c=14.51 Å, and 6 formula units per hexagonal cell.

The stable Indium oxide has a body-centered cubic structure with lattice parameter 10.117 Å (twice larger than ordinary fluorite materials) [107]. Its Miller indices obey the constraint: h+k+l=2n, and 0kl if k, l=2n [107]. Each cubic unit cell consists of 16 formula units. It has 80 atoms per unit cell, and it is derived from a 2×2×2 supercell of fluorite structure (CaF_2). 25% of oxygen atoms are removed from fluorite structure to preserve an ordered structure. It contains two inequivalent Indium atoms which occupy two different lattice positions. 48 equivalent oxygen atoms fill the edge positions Wycoff 48e, and 8 indium atoms and 24 ones occupy respectively In-b (Wycoff 8a) and In-d (Wycoff 24d) sites. The atomic positions in bcc structure are shown in table 2.1.

Table 2.1: Positional parameter for bixbyite- In_2O_3, obtained from DFT calculations [108].

Atom	Site	x	Y	Z
In-b	8a	0.2500	0.2500	0.2500
In-d	24d	0.4665	0.0000	0.2500
O	48e	0.3900	0.1544	0.3820

As depicted in Fig. 2.9, the In-b position is located at the body diagonal of the two oxygen vacancies with the same bonding length In-O of 2.161 Å, while the In-d one is surrounded by two V_O at the face diagonal of the cube with three different bonding In-O lengths of 2.133, 2.187, and 2.247 Å [95].

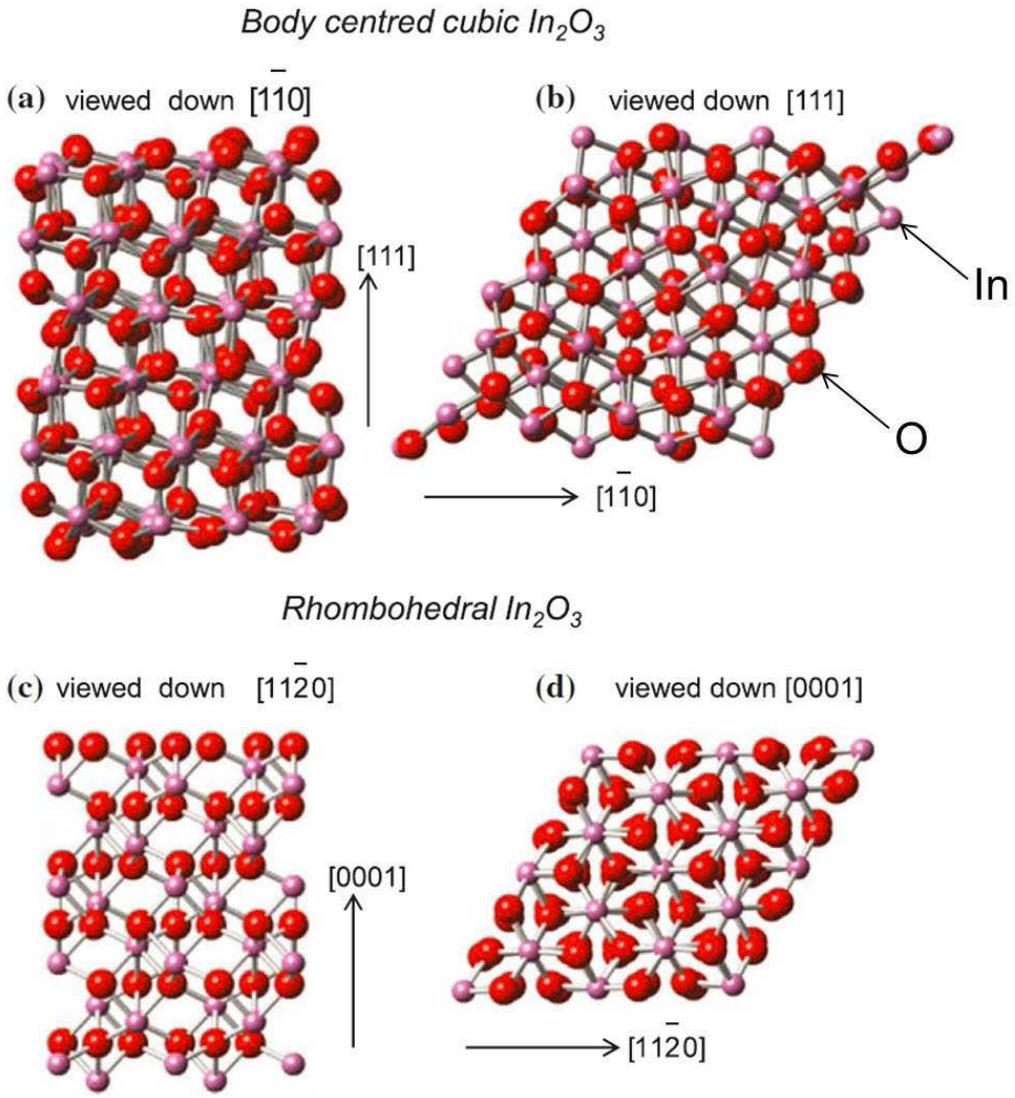

Figure 2.8: Crystal structure of a) and b) bcc-In_2O_3 and c) and d) rh-In_2O_3. From [95].

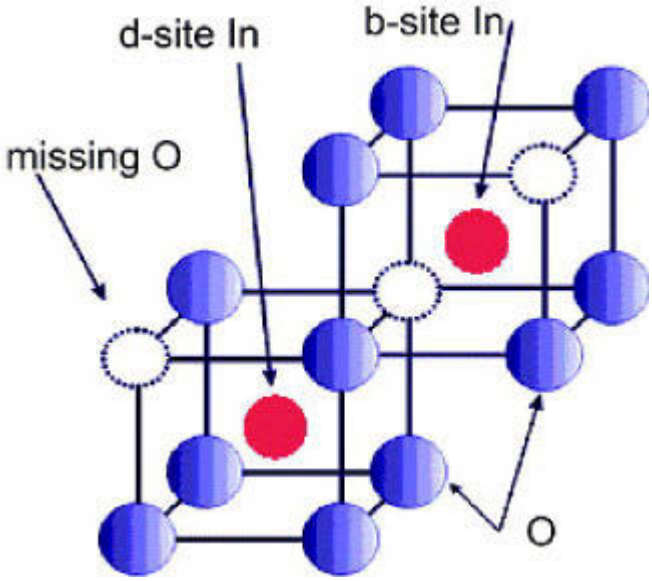

Figure 2.9: Local crystal structure of bcc-In_2O_3. In, O atoms and oxygen vacancies are presented with red, blue, and open balls, respectively. From [109].

Figure 2.10 represents the Brillouine zone (BZ) for bcc-In_2O_3 on the left side, the symmetry crystallographic directions of ΓP <111> and ΓN <1$\bar{1}$0> are denoted by blue and green arrows, respectively.

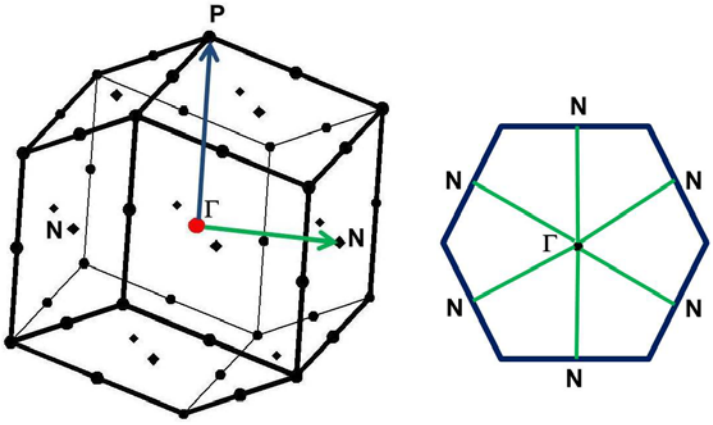

Figure 2.10: Left: The sketch of the Brillouin zone of bcc-In_2O_3 and two symmetry directions ΓP (blue arrow) and ΓN (green arrow). Right: Crystallographic plane ΓN.

The right side of this figure illustrates the crystallographic ΓN plane as well as all six ΓN directions. This plane is orthogonal to ΓP direction [5].

2.5.2 Energetics of surfaces and surface structures

The bixbyite indium oxide possesses three low-index surfaces: (001), (110), and (111). Figure 2.11 represents these surfaces and the similar views of the fluorite surfaces as well the relaxed energies of stoichiometric terminations of bulk structure and their associated relaxation energies were determined by means of periodic slab calculation within DFT framework [95]. According to Tasker classification [95], the (001) surface of fluorite is a ‘’Type III’’ ionic surface with changing anion and cation planes, which leads to a surface dipole. The shift of the half of the outermost ions to the other side of slab, i.e. microfaceting gives rise to the polar surface formation [95]. On the other hand, the (110) is a stable ‘’Type III’’ surface which is composed of neutral ionic layers. The ‘’Type II’’ (111) surface is derived from quadrupolar grouping of anionic and cationic layers, which repeat one after each other. In fact, each (111) unit cell is composed of repeating quadrupolar units with a total formula $\{[O^{2-}]_{12}^{24-}\ [In^{3+}]_{16}^{48+}\ [O^{2-}]_{12}^{24-}\}$.

The structural vacancies and relaxations in atomic positions in the bixbyite-In_2O_3 cause slight disorder in cation layers and consequently minor differences in the appearance of the surfaces with respect to the fluorite structure ones. The (111) surface has the lowest surface energy, so it is the most stable one compared to the other surfaces in this structure [110-112]. A single In-O bond length will be broken by cleavage along the (111) plane, and afterwards the contraction of the <111> In-O bond by around 9 % in subsurface layers leads to enough relaxation of the surface [95].

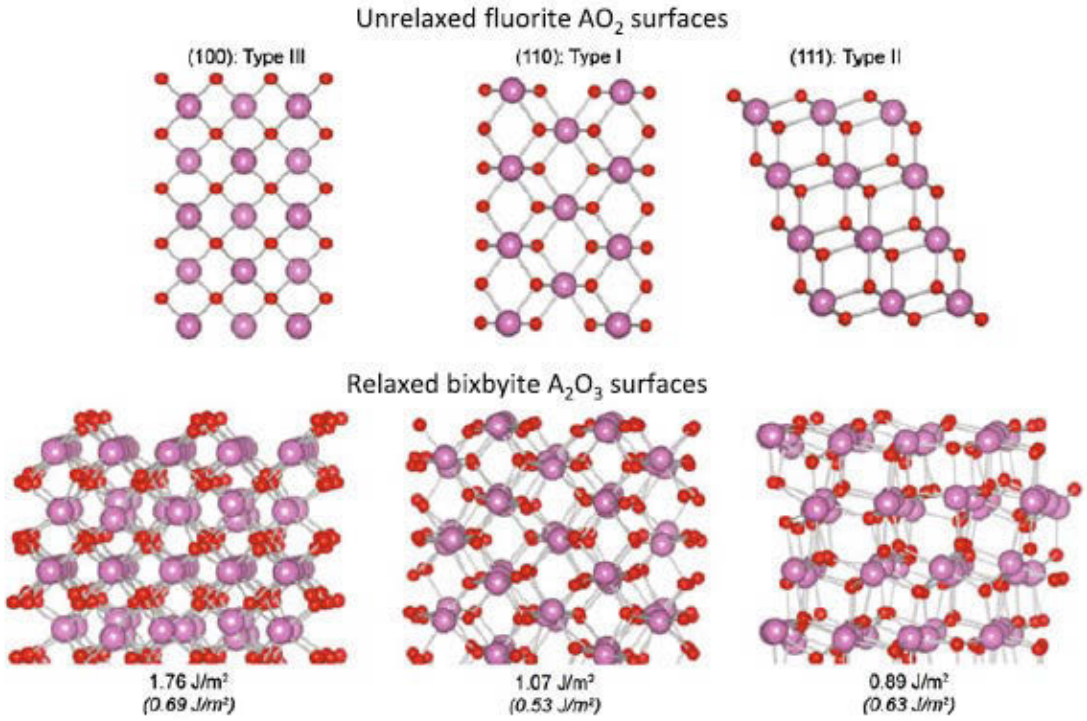

Figure 2.11: Adopted from [95]: The schematic representation of the surface structures of the pristine low index termination of the fluorite (AO_2) in the upper part, and bixbyite-In_2O_3 (A_2O_3) in the lower part, determined by density-functional calculations. Cations and anions are denoted by large and small balls, respectively. The relaxed energy of terminations and also relaxation energy in the parentheses are included.

Chapter 3
Crystal growth and characterization

In this chapter the crystal growth method of the In_2O_3 bulk single crystals and their characterization will be described. The samples were grown from the melt by a novel method called Levitation-Assisted Self-Seeding Crystal Growth Method (LASSCGM) by Dr. Zbigniew Galazka at IKZ institute [22, 23]. The sample preparation will be presented briefly and the sample analysis will be discussed.

3.1 Crystal growth

Self-seeded In_2O_3 bulk single crystals have been prepared by various methods, from the vapor phase of indium and ambient oxygen [113], chemical vapor transport (CVT) [5], electrolysis [114], and flux method [13, 115]. The high purity In_2O_3 bulk single crystals which are the subject of this thesis were grown from melt through innovative growth technique, Levitation-Assisted Self-Seeding crystal growth method [22]. The advantage of the obtained crystals from this technique is their low unintentional electron concentration and their larger size, which can be used as a substrate for homoepitaxial growth.

3.1.1 Levitation-Assisted Self-Seeding Crystal Growth Method

The main obstacles, which impede obtaining TCO bulk single crystal from melt, are two issues:

1- The thermo-chemical instability of this category of materials at elevated temperatures, i.e. over 1500 ^{0}C
2- Their high melting points (over 1800 ^{0}C) and consequently the type of metal crucible used for the growth

High oxygen partial pressure is needed to overcome the instability of oxides. For the case of β-Ga_2O_3 and ZnO, the oxygen partial pressure supplied by self-adjusting atmosphere in the presence of CO_2, through decomposition of CO_2 to CO and O_2. However, this way cannot provide enough oxygen partial pressure as a result of high oxygen decomposition pressure of In_2O_3 and its much greater instability in comparison to afore-mentioned oxides.

The only option for crucible type is iridium (Ir), which can resist in the oxides growth conditions.

Thanks to the new method of growth (LASSCGM), these constraints could be removed. This technique benefits from the high activity and the high corresponding concentration of indium liquid compared with the other liquid metals in the other oxide melts [22]. Therefore, there is a high probability of the eutectic formation between liquid In and the metal crucible, here In-Ir alloy. As a result of the presence of liquid indium in the melt, the In_2O_3 melt also becomes electrically conductive. Thus, the conductive In_2O_3 melt could be coupled to electromagnetic field generated from an RF coil, and subsequently leading to the float of at least a portion of In_2O_3 melt.

Some necessary perquisites for the growth condition must be considered which are as follows:

1- The thickness d of the metal crucible must be smaller than the penetration depth of the electromagnetic fields δ, i.e. $d \leq \delta = \sqrt{\frac{1}{(\pi f \mu \sigma)}}$ (f, μ, and σ are respectively frequency of RF coil, permeability and the electrical conductivity of the crucible).
2- The configuration of the crucible and the RF coil should be appropriately dependent.
3- Since the melt must be electrically conductive, the concentration of oxygen is restricted.

4- Openings, which should be 5 to 15 % of the crucible cross section, must be considered on the crucible cover to evacuate decomposition materials originated from CO_2 decomposition and provide low temperature gradients in the crucible.
5- A part of In_2O_3 melt must be levitated through a liquid neck creation, i.e. a seed formation throughout crystallization process.

Figures 3.1(a) to (e) display the simplified image of the fundamental stages of the LASSCGM with the major parts, Ir-crucible that contains In_2O_3 starting material, Ir-lid with evacuation openings, and RF coil which produces electromagnetic field. As depicted in panel (a) of this figure, the insulator In_2O_3 is warmed up through heat conduction and radiation from the crucible wall, which is heated up by the RF coil. The insulator In_2O_3 starting material decomposes and also becomes conductive in the hottest region of crucible as a result of the eddy currents induced at elevated temperature (higher than 1800 ^{0}C), see Fig. 3.1(b). At the melting point of indium oxide (1925^{0}C), the higher conductivity of In_2O_3 and subsequently an increase of affected charges by the eddy currents lead to the ease of charge melting. A magnetic field is produced by conducting charges of In_2O_3 liquid which opposes the magnetic field from the coil. Therefore, the In_2O_3 liquid may levitate relative to the crucible-coil position due to the resulting forces overcoming gravity. In order to form a neck with appropriate shape between the suspended melt and the deposited melt at the bottom of the crucible, the float of melt is controlled through configuration and absolute temperature of evacuation openings and thermal insulation of the crucible top.

The reason of importance of the neck's shape is that there is a risk of inappropriate breakdown for a very thin neck, and a thick one prevents growth of the single crystal. In order to obtain suitable neck shapes, three different strategies can be used:
First of all, the growth geometry is accurately designed to let the melt levitate without overheating. Secondly, a thicker neck is prepared, and afterwards it is thinned down by separating the two parts of melts by overheating and therefore inducing higher levitation forces.

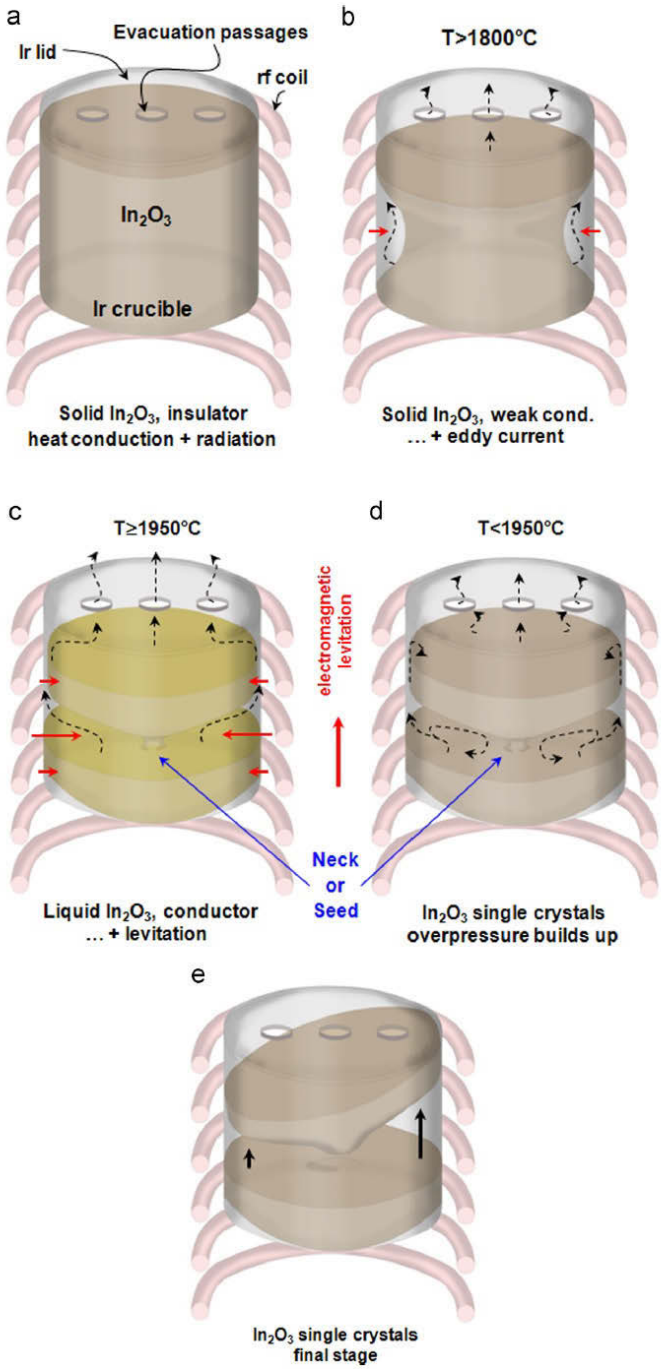

Figure 3.1: Simplified fundamental stages of Levitation-Assisted Self-Seeding Crystal Growth Method. a) Solid In_2O_3 starting material and before warming up. b) In_2O_3 before melting. c) Molten In_2O_3. d) In_2O_3 single crystals after crystallization. e) Final stage of the growth of In_2O_3 single crystals. The eddy current, decomposition products, and overpressure are denoted by horizontal solid, dashed, and vertical solid arrows, respectively. From [22].

Lastly, the neck becomes thin by soaking, i.e. leaving the melt at a temperature higher than the melting point for a certain time, which leads to the decomposition of the melt.

The levitation improves the electrical conductivity of In_2O_3 liquid. The occurrence of levitation is detected by monitoring the temperature profile.

In order to control the mass loss of In_2O_3 because of the high decomposition rate after overheating, the growth system must be cooled down instantly to the point of solidification and hardening. Throughout the solidification point, two single-crystals shape on the opposite sides of the neck. Breaking the neck before the crystallization impedes the single-crystal formation, but if it occurs, polycrystals will form. These polycrystals are composed of needle-shaped and vertically arranged single crystals which show cross-sectional honeycomb like structure. Decomposition happens specifically, at the upper surface of the bottom crystal, which is quite hotter compared to the top one after solidification as a result of the high temperature. The screening effect and consequently reduction of the electrostatic potential may cause a residual melt on the top of the hot crystal. Decomposition products condensate on the upper surface of the top crystal, and fill the gap between this crystal and the wall of the crucible. This crystal is pushed upwards because of the resulting overpressure around the neck. The occurrence of this process is accompanied by coming out smoke from the openings of crucible. In the case of a successful levitation of the melt, an oscillation can be observed in the temperature behavior during this stage of growth. It is noteworthy that the neck size and the geometry of evacuation openings are critical in this growth technique: The top and bottom crystals will be broken as a result of a thin neck. Evacuation openings also play a crucial role in low temperature gradients maintenance throughout melting process and evacuation of decomposition products during and after the solidification. One should consider this point in openings design, since a partial blocking of the openings due to the condensation of decomposition materials can reduce the evacuation rate and cause explosion because of the overpressure.

A successful levitation results in two crystals which are attached by the seed, and dropped in the crucible. In this case, the Ir-crucible remains clean after the growth, and it can be used for the growth 40 times without cleaning. In contrast, an unsuccessful levitation causes severe damage of crucible due to the solidification of the whole charge and In-Ir eutectic formation.

In addition to high quality and purity of the obtained single crystals, the simplicity and reasonable efficiency of crystallization (30-50%) are the other advantages of this growth method. Figures 3.2(a) and (b) show the two gained single crystals. The thickness of the top and the bottom crystals are generally in the range of 5 to 15 mm, which depends on the quantity of In_2O_3 starting material and decomposed products, and relative crucible-coil position. The (111) face is shown by arrow in Fig. 3.2(a). The diameter of the bulk crystals is typically around one inch. The greenish-yellow deposit on the upper surface of the top crystal originates from the condensation of the decomposed materials during solidification.

The as-grown crystals are opaque and dark as shown in Fig. 3.2(c), and upon annealing in oxidizing condition they become yellowish and transparent, see figure 3.2 (d). The dark color of the as-grown crystals was found to be stem from the existence of the In-nanoparticles, which cause a severe light absorption or scattering.

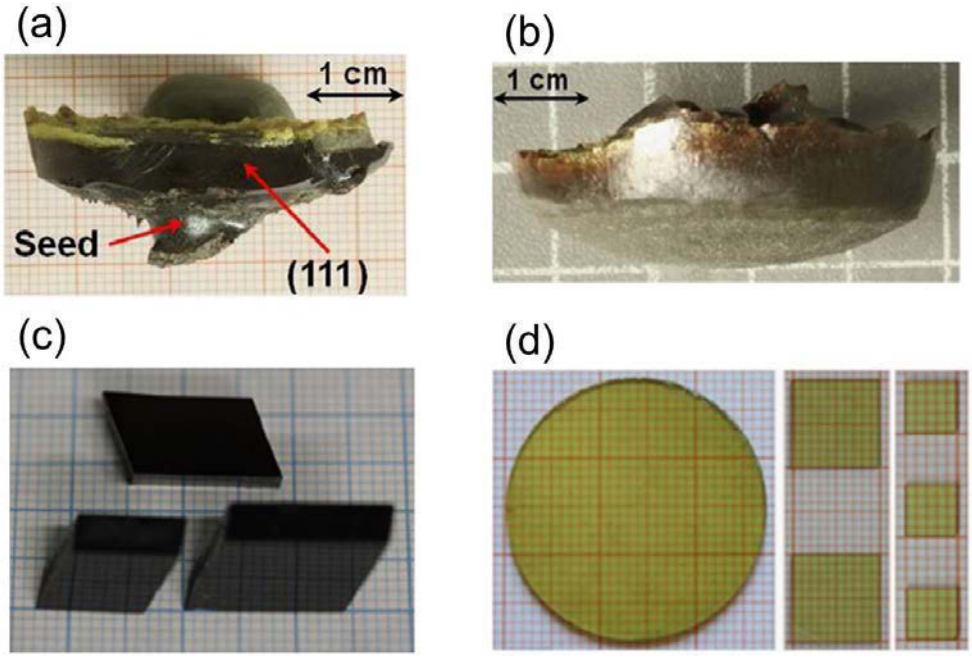

Figure 3.2: Obtained bulk single crystal by LASSCGM: a) Top crystal. b) Bottom crystal. c) Dark as-grown crystals slabs. d) As-cut annealed single crystals in oxidizing condition.

Adopted from [22].

The studied crystals in the present work were annealed in O_2 atmosphere for at least 10 hour at 800-1000 ^{0}C. For more details about the crystal growth instrumentation, see Ref. [22, 23, 61].

3.2 Characterization

The annealed-melt grown In_2O_3 samples were analyzed by different techniques. The chemical stoichiometry, structural quality and crystal orientation, and atomic scale of the surface image were checked by energy dispersive X-ray spectroscopy (EDX), Laue diffraction and scanning tunneling microscopy (STM), respectively. The mentioned methods as well as the obtained results for the crystals will be outlined in this section.

3.2.1 Energy Dispersive X-ray Spectroscopy

Energy dispersive X-ray spectroscopy is an analytical method used to assess the chemical composition of the samples. This method is based on the interaction between the X-ray excitation and a matter. This characterization benefits from the fundamental point that each element has unique and discrete energy levels and can be therefore identified by a specific set of peaks in the X-ray emission spectrum.

When a sample is subject to the high energy of electron beam or electromagnetic radiation, the electrons in the inner shell such as K, excite and are ejected to vacuum and therefore vacancies are created. The electrons from outer shell, e.g. L shell, occupy the vacant sites. As a result of this transition, a characteristic X-ray radiation is emitted or the released energy transfers to another electron and leads to removal of the electron from atom (Auger-Meitner effect). Fig. 3.3 shows the schematic image of this process.

This technique is limited to elements with atomic number $4<Z<92$. As the higher atomic number is, the lower the probability of Auger effect is. X-ray emission is prevailing for $Z>30$. So, the accuracy of this characterization is higher.

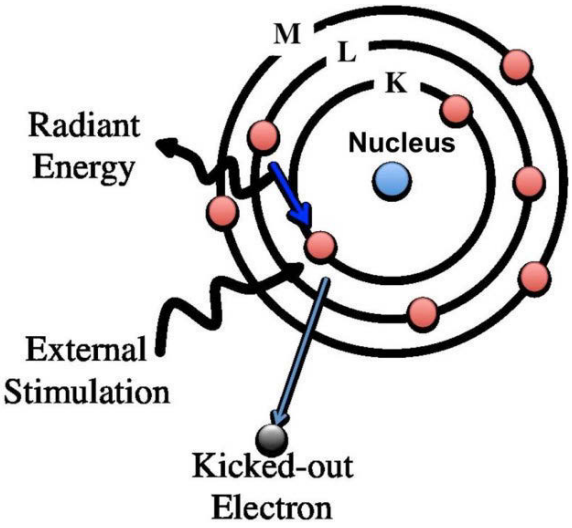

Figure 3.3: Schematic diagram of EDX: An external X-ray source ejects an inner-shell electron and leaving a vacancy, which is occupied by an outer-shell electron and resulting in a photon in X-ray range. From [116].

The resulting lines of the emitted photon are measured by a semiconductor detector lying after a monochromator resolving the different emission energies. The components and their concentrations are derived using the PUzaf [117] correction by commercial software.

In the present work, the samples were excited by a beam of 20 keV. Table 3.1 lists the chemical content of the In_2O_3 melt-grown single crystal as an example.

Table 3.1: Concentration of the In_2O_3 melt-grown single crystals obtained from EDX measurement

Sample	In composition	O composition
In_2O_3	1.90±0.082	3.10±0.175

3.2.2 Laue diffraction

Von Laue pioneered the qualitative analysis for crystal structure using X-ray diffraction experiments in 1912 [116] taking his name. The Laue method is primarily used to determine the structural quality and orientation of a single crystal. Identification of the crystal orientation is essential for the band structure investigation of the crystals using ARPES measurements. The samples thus were characterized by the Laue

diffraction. In this method, a continuous X-ray (Bremsstrahlung) with energies up to 40 k eV impinges on a fixed crystal. The range of the wave lengths of the incident beam should be large enough that some reciprocal lattice points lay in the constructed Ewald spheres, and not so large that too many Bragg reflections appear in the diffraction pattern and consequently render the interpretation difficult.

Due to the comparable wave length of the photon energy with the atomic distances, diffraction occurs if the Laue condition ($\overrightarrow{K_1}$-$\overrightarrow{K_0}$=$\vec{G}$) is fulfilled, where $\overrightarrow{K_1}$, $\overrightarrow{K_0}$, and $\vec{G}$ are wave vectors of incoming light, the diffracted one, and reciprocal lattice vector, respectively. The beam penetrates into the sample, so the bulk structure is studied by this method. Also, the shape and size of the diffraction spots show the quality of the examined crystal. A conventional unfiltered radiation from a copper target tube, i.e. Cu cathode, was used for Laue pattern in the present study. If the X-ray beam includes wavelengths for which the Ewald conditions is satisfied for each set of the crystal planes, the corresponding-reflected beams will be diffracted and recorded photographically on X-ray sensitive negative or Polaroid. Therefore, regular pattern of spots are produced on the film as a result of the diffracted beams. This technique can be operated in two modes: back-reflection and transmission modes. In the former mode the radiation is reflected from a fixed crystal, and the photographic film is located between the X-ray tube and the sample crystal, while in the latter one the radiation is transmitted through the sample and the film is placed behind the crystal. Here, the experiment was conducted in the back-reflection mode.

The schematic Laue-experimental setup in back-reflection mode is shown in Figure 3.4.

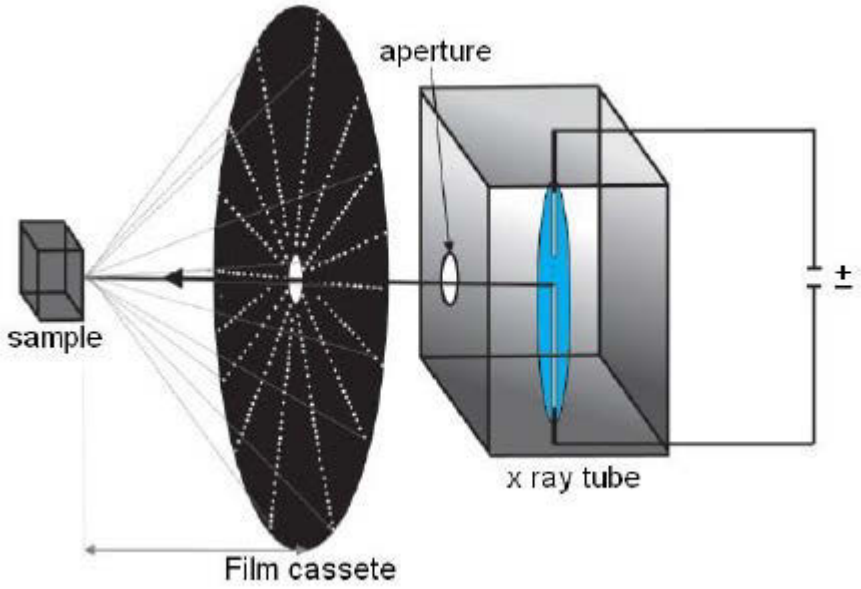

Figure 3.4: Schematic Laue set up, which includes X-ray tube as a source and film for recording the resulted pattern. From [118].

Fig. 3.5 depicts Laue diffraction pattern of the <111> surface of a melt-grown In_2O_3 single crystals. Clear three- fold symmetry of the [111] direction of the bcc structure can be seen which eases the orientation of the sample. Under reference to Laue Atlas [119],

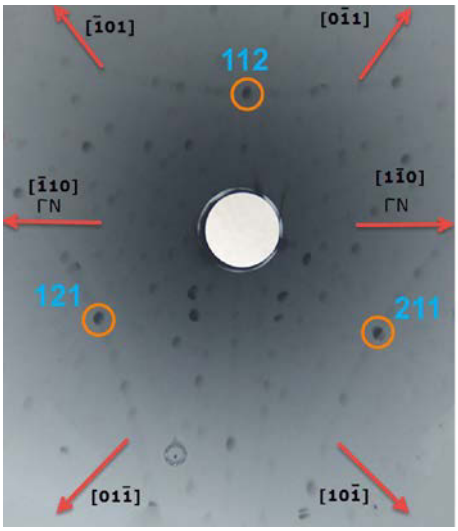

Figure 3.5: Laue pattern of a melt-grown In_2O_3 single-crystal.

the 112, 121, 211 reflections and all six crystallographic $[1\bar{1}0]$ directions, were measured.

3.2.3 Scanning tunneling microscopy (STM)

The advent of the scanning tunneling microscopy was a revolution in contemporary science and technology since it provided an opportunity to image individual atoms and molecules. This technique was established at IBM Zürich by Gerd Binning and Heinrich Rohrer [120]. STM is an electron microscope able to reach atomic resolution by scanning using a tip (ending ideally with a single atom) on a surface. This method is based on the quantum electron tunneling between two separated electrodes due to application of the biased voltage. One of the electrodes is shaped as a sharp tip. The tip is held about a few angstroms from the sample until current flows between them. A property of this current is that it is exponentially dependent on the distance between the electrodes. This invention made the study of the electronic density of states at the atomic scale possible because the current depends on the electronic properties of the sample. Fig. 3.6 represents the schematic diagram of a STM. As shown in this diagram, a biased voltage of V is applied to the sample and the tip, when moving along the z direction. The tip and the specimen are different materials. Thus, they have different work functions Φ_T and Φ_s, respectively. The Fermi energy becomes constant at equilibrium which leads to the formation of an electric field in the vacuum levels across the gap region. The resulting potential in this region is quite larger than the thermal energy kT. By quantum tunneling process and in an unpolarized tip-sample junction the electron can tunnel through the barrier from tip to sample or from the sample to the tip. Thus, the net resulting current is zero in this situation. On the other hand, a net current exists by application of a biased voltage of V to the tip and the sample which leads to the shift of the Fermi energy of the sample by –eV. By means of the time-dependent perturbation method and considering the isolated sample and tip as the unperturbed system, the tunneling current can be quantified [121, 122]. For the case of the elastic tunneling, the transition probability $\omega_{\mu\nu}$ from the sample state ψ_ν to the tip state χ_ν can be obtained by using the one-particle Schrödinger equations for the tip and the sample and employing the Fermi golden rule:

$$\omega_{\mu\nu} = \frac{2\pi}{\hbar} \left| M_{\mu\nu} \right|_0^2 \delta(E_\nu - E_\mu) \tag{3.1}$$

Where matrix element $M_{\mu\nu}$ is given by:

$$M_{\mu\nu} = \int x_\nu^*(x) u_T(x) \Psi_\mu(x) d^3x \tag{3.2}$$

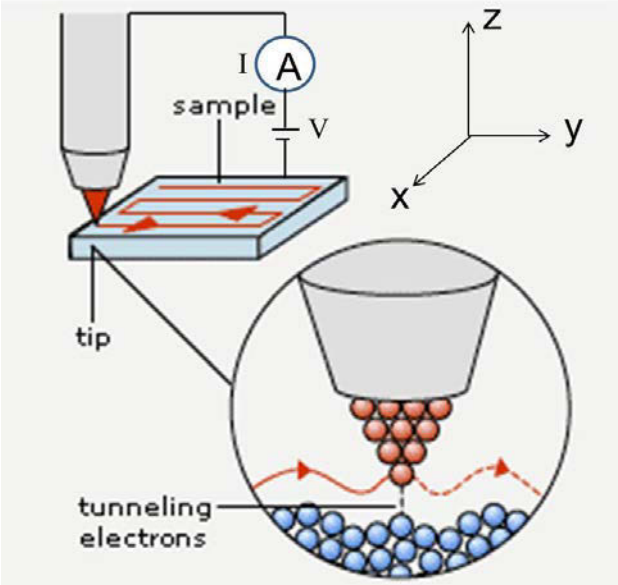

Figure 3.6: Schematic representation of a STM. From [123].

here, u_T is the electron potential in the tip. The delta function in the equation (3.1) indicates that only electron tunneling occurs between levels of equal energy. The total current is determined by summing the transition probability over all the possible ψ_μ and χ_ν states and the multiplication of the result by the electron charge e. After changing the sum into an integral over energies using the density of states and applying the Fermi-Dirac distribution and a few approximations, the total tunneling current results in:

$$I = \frac{4\pi e}{\hbar} \int_0^{eV} \rho_T(E_F^T - eV + \epsilon) \rho_S(E_F^S + \epsilon) e^{-2ks} \mathrm{d}\epsilon \tag{3.3}$$

where E_F is the Fermi energy, ρ_T and ρ_S are the tip and sample density of states, respectively. $k = \sqrt{\frac{2m}{\hbar^2}(\Phi_{eff} - \varepsilon)}$ (in which $\Phi_{eff}(V) = (\Phi_T + \Phi_S + eV)/2$). The index T and S denote the tip and sample, respectively, and s is the tip-sample separation.

A piezoelectric actuator is generally used to accurately detect the movement of the tip with respect to the sample. The outer surface of the piezoelectric is usually composed of the four electrode sections with the same area. In order to move the piezoelectric tube laterally, the piezoelectric tube is bent by applying opposite voltages between the inner

and the opposite sections of the outer electrodes, while for the movement along the z direction both electrodes must be polarized with the same voltage. In practice Besocke-beetle scanners are commonly used consisting in a piezo tube acting as a scanner which carries the tip and is placed at the center of a coarse position device, and surrounded by three more piezoelectric tubes to ease the larger displacements of the tip relative to the sample and exchange of the sample and tip as well. The Besocke-beetle includes a base plate with three 120° sections of a shallow ramp, see Fig. 3.7.

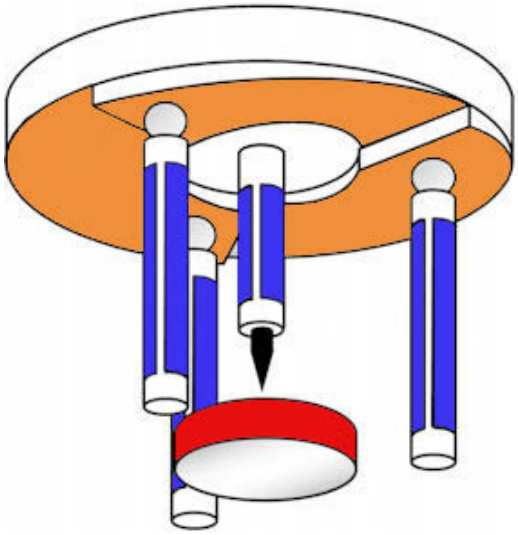

Figure 3.7: Schematic design of a Besocke-beetle scanner. Adopted from [124].

This microscopy is regularly employed to image the structural properties of surfaces. The first STM images were acquired on the CaIrSn4 and Au in 1982 [124]. In order to produce images, the tunneling current as a function of the tip position is recorded in two different modes: constant height and constant current modes which are displayed in figure 3.8. In the constant height mode, the z section of the scanner is held fixed along with the tip movement over the sample at the constant bias voltage, and the STM image is generated as a result of variation of the tunneling current due to the variation of the tip-sample separation. In the other mode the z section of the piezo scanner is moved by the electronic feedback to keep the tunneling current constant, whereas the scanner moves over the surface in x and y directions. The feedback signal is recorded and used to produce topographic images [124].

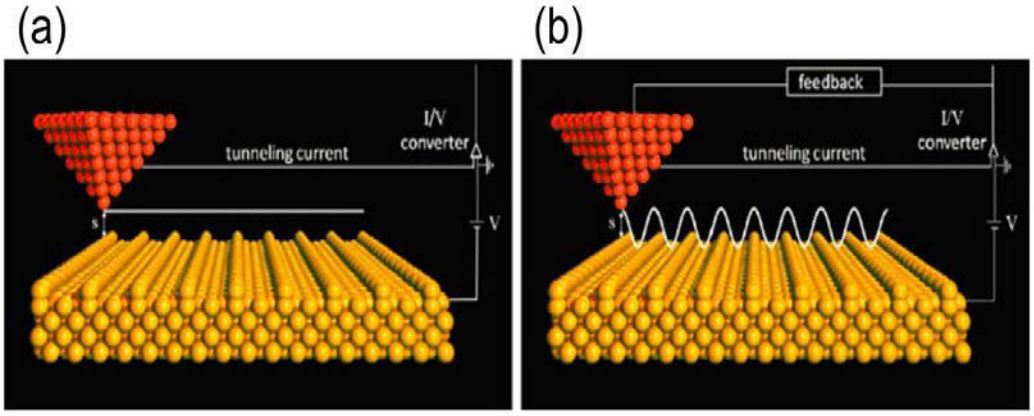

Figure 3.8: Different operation modes of the STM: (a) Constant height (b) Constant current modes. The path of the tip movement is shown by thick lines. From [124].

The atomic resolution of the topographic images and accuracy of the scanning tunneling spectroscopies fundamentally depend on the sharpness and shape of the tip. They are frequently prepared by manually cutting a thin Pt-Ir wire or electrochemically etching a tungsten wire. In the present work, platinum-iridium tips were used. The quality of tips was improved by shaping procedures by inducing pulses and crashing them into metal surfaces, here gold surface. Afterwards, its atomic resolution was checked on graphite to test ability of the prepared tip to resolve single atoms on the surface of this crystal.

STM is also really sensitive to mechanical noises and vibration sources, which should be eliminated to the highest extent. To this aim, various strategies can be applied, such as suspension springs, eddy current dampers, minimizing low frequencies mechanical noises by setting up a small and stiff STM system with a high resonance frequency and using an STM with a heavy body [124].

In the present work, the STM measurements were carried out by means of UHV-scanning tunneling microscope constructed by Omicron Nano Technology GmbH, Germany and using manually-cut Pt-Ir tips at a base pressure of 10^{-10} mbar at room temperature. The samples were cleaved along (111) plane before the experiment in the preparation chamber in the pressure better than 2×10^{-10} mbar. The images were recorded in the constant-current mode with the sample bias of +1.1 V and tunneling current of 0.2 nA and the loop gain of 5-6 %.

The STM image of as-cleaved melt-grown In_2O_3 (111) bulk single crystals is shown in Fig. 3.9. As demonstrated in this figure, flat surface with large uniform terraces and straight step edges are identified in contrast to the observed smaller and wavy ones in references [101, 102]. The height of the steps 0.28 nm is in accordance with the aforementioned references [101, 102] as well as the calculated value of the height of one layer h ($h = \frac{a}{2\sqrt{3}} = 0.292\ nm$, where a is the lattice constant of the bulk unit cell of bcc-In_2O_3).

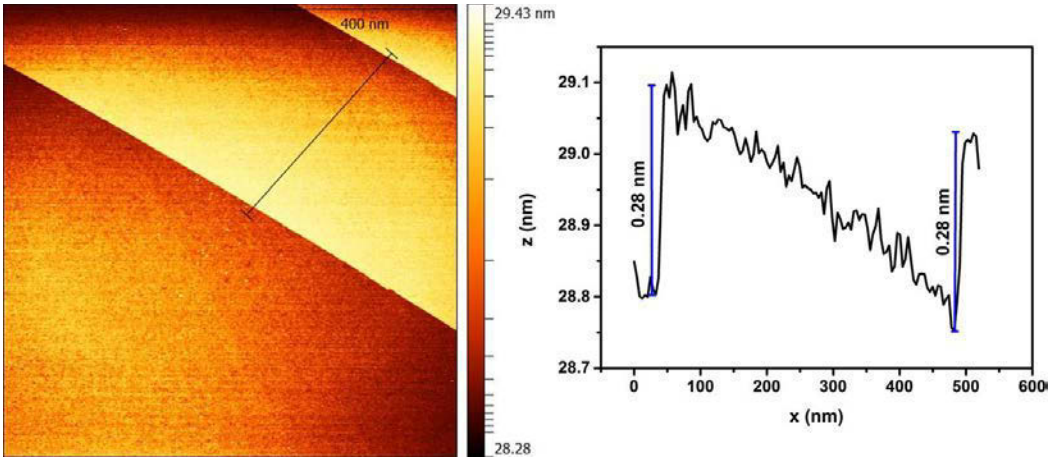

Figure 3.9: Left: STM pattern of (111) surface of melt-grown In_2O_3, showing the presence of terraces at the surface which were separated by steps with straight line edges. Right: The height profile across two steps, denoted by black line in the left STM image, the height of the steps is around 0.28 nm.

Figure 3.10 (a) displays a 50×50 nm^2-STM photograph of the studied crystals. By help of 2D Fourier transformation (2D-FT) and Fourier filtering, it is possible to extract pure structural information from the images. The image obtained by 2D-FT is shown in the panel (b) of Fig. 3.10. The central and brighter part of the Fourier-transformed image corresponds to the large frequencies, while the outer part associates with lower frequencies and the roughness of surface in real space.

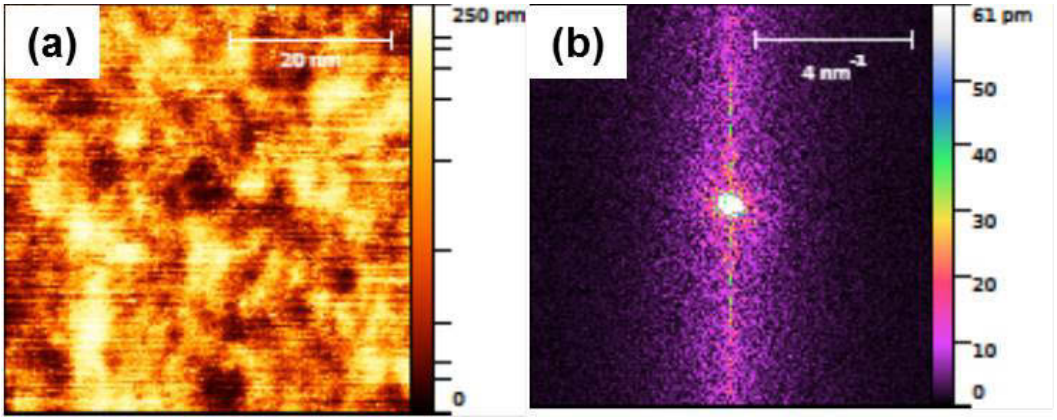

Figure 3.10: (a) a 50×50 nm^2-STM photograph of as-cleaved melt-grown In_2O_3 (111). (b) 2D-FT image of (a).

By 2D-FT filtering and in fact back-transformation, one can separate these two parts. Figures 3.11 (a) and (b) display the chosen part of the 2D-FT and its back-Fourier transform, respectively. In Fig. 3.11 (c) the line profile of the black line in back-FT STM image is presented. The peaks are separated every 1.41 nm distance. This value agrees very well with the lattice parameter of the hexagonal unit cell of In_2O_3 [101]. Fig. 3.11 (d) shows the STM photograph in panel (b) in magnification. In this image one can see the periodic structure of the In_2O_3 and hexagonal arrangement of the surface comparable with the DFT-calculated unit cell of oxidized In_2O_3 (111) with lattice parameter of 1.43 nm, depicted in Fig. 3.11 (e), adopted from Ref. [101]. In this image, the six and five-fold coordinated In atoms and four and three-fold coordinated O atoms are labeled by In(6c), In(5c), O(4c), and O(3c), respectively. The high-symmetry positions are denoted by A, B, and C, which correspond to the center of the In (5c)-O (3c) rings, the center of In (6c) atom and the center of the In(5c)-O(4c) rings.

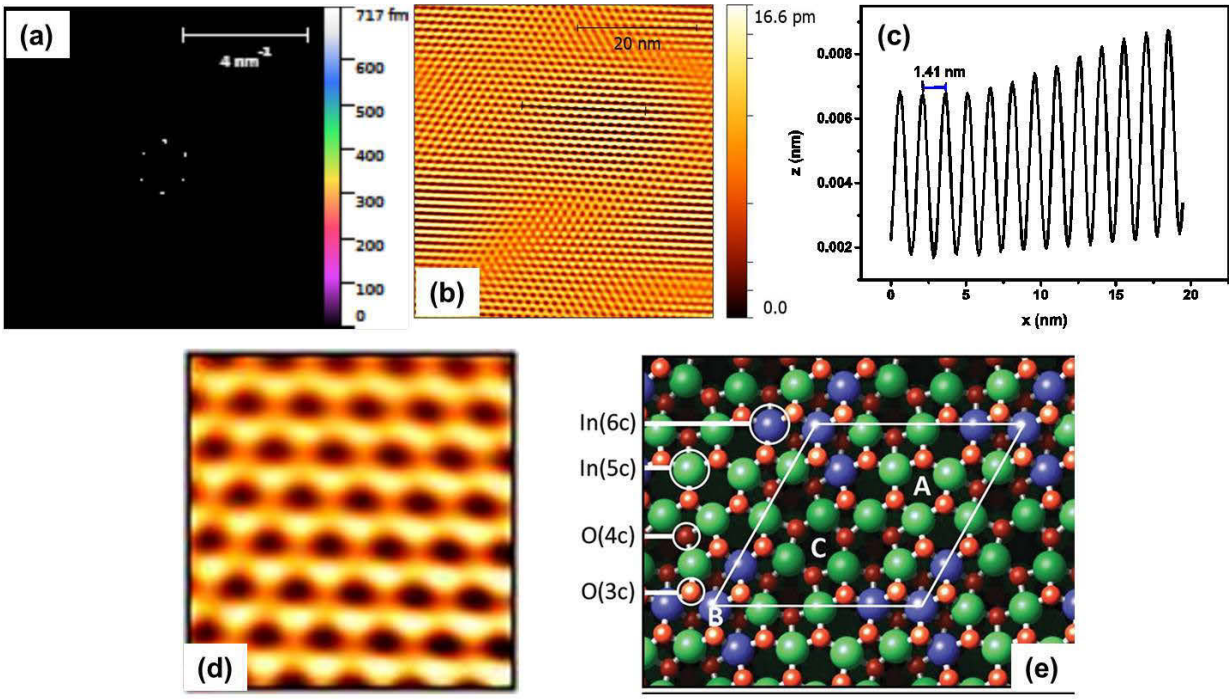

Figure 3.11: (a) The selected part of the 2D-FT of the STM image of the In_2O_3 (111) crystal. (b) The back-FT of the chosen part in (a). (c) Height profile across the black spots (peaks in (c), which are separated every 1.41 nm distance. (d) The magnified STM image in (b). (e) The DFT-obtained hexagonal unit cell of an oxidized In_2O_3 (111), the high-symmetry position are denoted by A, B and C [101].

Chapter 4
Electrical and optical characterizations of In_2O_3

As aforementioned, high quality and purity In_2O_3 can become a new transparent semiconductor and can be used in novel and high-performance electronic devices. Design and optimum performance of such devices require accurate knowledge of electrical and optical properties of their components. Electrical characterizations provide important information of the transport properties, such as resistivity, electron concentration and mobility. In this chapter, a brief introduction of the Hall-effect measurement and the results of that of the high quality and purity melt-grown In_2O_3 bulk single crystals will be presented at first. Afterwards, the determination of fundamental band gap of the crystals will be discussed by using optical transmission measurements. The band gap will be compared with the one obtained from surface sensitive technique, ARPES, within the next chapters.

4.1 The electrical characterization

Charges can transport through the semiconductors as a result of the electric field. Important semiconductor devices like transistors, diodes and solar cells are based on the transport of charge. Therefore, it is necessary to know about the transport properties of the studied crystals which also were used for metal-In_2O_3 interfaces, and their results will be presented within the next chapters. The unintentionally high conductivity of the TCOs eases ohmic contacts preparation and subsequently the measurement of their

electrical properties. In this section, the theory and also the experimental results of the Hall-effect characterization will be outlined.

4.1.1 The Hall-effect

The Hall-effect is the most widely used method to obtain the carrier concentration of the material and its type directly. This effect was discovered by Edwin Hall in 1879 [125]. As depicted in Fig. 4.1, when transverse electric current passes through an electrically conductive sample along the x-axis and in the presence of a magnetic field perpendicular to the current, a voltage difference V_H and subsequently electric field E_H is produced across the sample because of the Lorentz force ($qv \times B$). E_H causes the displacement of the carriers in a direction perpendicular to the magnetic field and the current. The resulted force of the Hall voltage is in the opposite direction of the Lorentz force, and at equilibrium they are equal:

$$ev_d B = -eE_H \rightarrow E_H = -v_d B \tag{4.1}$$

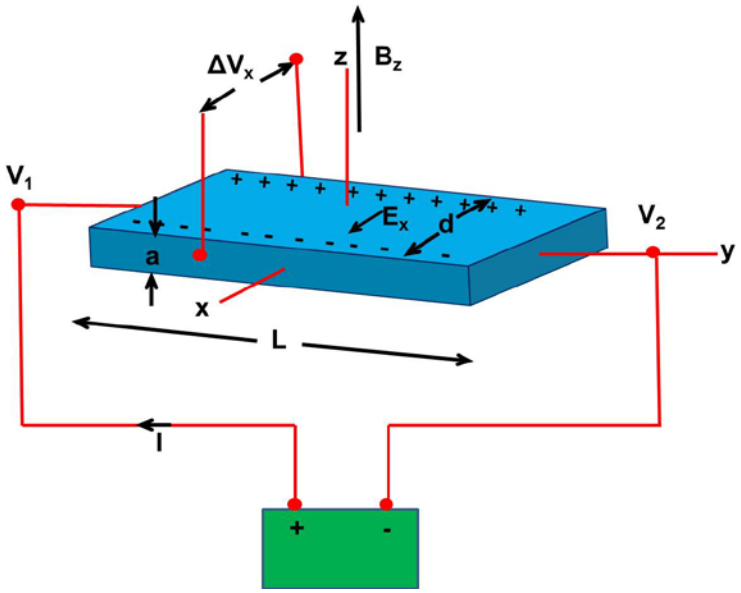

Figure 4.1: Schematic diagram of the Hall-effect measurement [126]

Since $j = env_d$ (v_d drift velocity) the Hall voltage is given by:

$$V_H = \frac{-Bjd}{en} = \frac{R_H BI}{a} \rightarrow R_H = -\frac{1}{ne} \tag{4.2}$$

where R_H, B, I, d and a are the Hall coefficient, magnetic field, current, width and the thickness of the studied sample, respectively. In fact, the Hall coefficient is the ratio of the transverse electric field to the product of current density and magnetic field [127]. As shown in equation (4.2), the concentration and the type of the charge carriers can be determined by the Hall measurement.

Paul Drude proposed a model of electrical conduction, named Drude model [128]. In this model electron-electron interactions was not taken into account, and it is based on the assumption that the magnetic field is weak. Therefore, these assumptions lead to equality of the rate of the momentum variation of the electrons movement in the external magnetic field with that because of the scattering, which means

$$\left[\frac{dp}{dt}\right]_{\text{scattering}} = \left[\frac{dp}{dt}\right]_{\text{field}} \Rightarrow \frac{P}{\tau_m} = e(E + \frac{P}{m} \times B) \tag{4.3}$$

where τ_m is relaxation time. Thus

$$\begin{aligned} \frac{p_x}{\tau_m} &= -eE_x - \frac{ep_y B}{m} \\ \frac{p_y}{\tau_m} &= -eE_y + \frac{ep_x B}{m} \end{aligned} \tag{4.4}$$

By multiplication of equation (4.4) by $=\frac{-ne\tau_m}{m}$, and as $j=enV_d$, and conductivity $\sigma = \frac{ne^2\tau_m}{m}$, equation (4.4) leads to the following tensor

$$\begin{bmatrix} E_x \\ E_y \end{bmatrix} = \sigma^{-1} \begin{bmatrix} 1 & \omega_C\tau_m \\ -\omega_C\tau_m & 1 \end{bmatrix} \begin{bmatrix} j_x \\ j_y \end{bmatrix} \tag{4.5}$$

where $\omega_C = \frac{eB}{m}$.

For $j_y=0$, the Hall field is:

$$E_y = -\left(\frac{\omega_C\tau_m}{\sigma}\right) j_x = -\left(\frac{B}{ne}\right) j_x \tag{4.6}$$

So, it results in the equation (4.2), i.e. $R_H=-1/ne$. According to this equation, the Hall coefficient depends only on the carrier concentration and its type. In contrast to the

prediction of that, this coefficient depends on magnetic field, temperature and the accuracy of sample preparation [129].

The common sample configuration geometries which are used for the Hall measurement are Hall bar and van der Pauw method. Since the latter method was used here to acquire the electron concentration, it will be outlined briefly in this section.

The van der Pauw contact arrangement can be used for the homogenous and isotropic sample even with arbitrary shape with uniform thickness [130]. It is usually needed to make four point contacts on the sample rims. The conventional configurations of this method are displayed Fig. 4.2. By measuring the sample thickness one can obtain the volume values for the resistivity and electron concentration. In this method the measurement should be done in two distinct series with the magnetic field in the positive and negative directions of z-axis. Also, the magnitude of current and magnetic field must be kept constant during the measurements. The current is applied to two adjacent contacts like I_{12}, and the voltage of two other contacts like V_{34} (V4-V3) will be recorded. The sheet resistivity is given by

$$R_{sh} = \frac{\pi}{2\ln(2)}\left(\frac{V_{43}}{I_{12}} + \frac{V_{14}}{I_{23}}\right)f \qquad (4.7)$$

In this equation f is a factor which varies from unity as the resistance ratio $R_{43,12}$ /$R_{14,23}$ does [33, 131]

The Hall voltage is obtained by using the following equation:

$$V_H = \frac{V_{13} + V_{24} + V_{31} + V_{42}}{8} \qquad (4.8)$$

where $V_{ij}=V_{ij,P}-V_{ij,N}$ and $V_{ij,P}$ and $V_{ij,N}$ are the voltage difference of contacts number i and j for the positive (denoted by subscript P) and negative magnetic field (denoted by subscript N), respectively. The concentration of sheet is obtained by using $n_{sh} = \frac{IB}{e|V_H|}$ [132].

The electrical properties of the melt-grown crystals also were studied using van der Pauw method by Dr. Kalus Irmscher at IKZ. The point-like ohmic contacts were made using In-Ga eutectic on the sample's corners in van der Pauw arrangement. The typical size of samples was 3×5×0.5 mm^3.

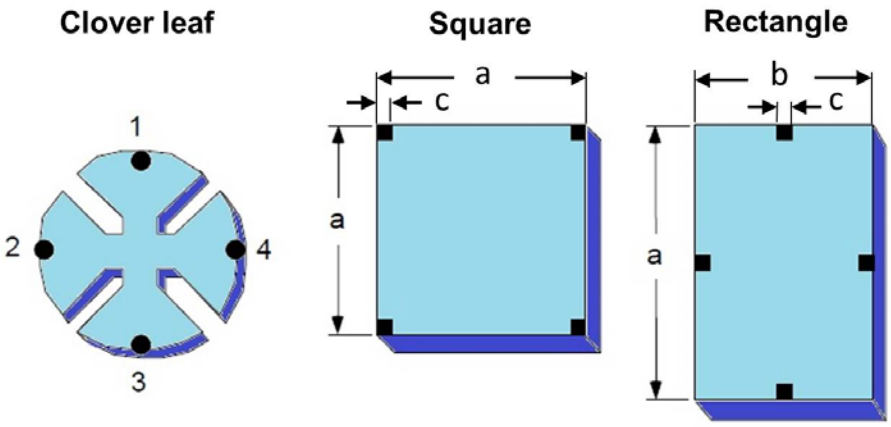

Figure 4.2: Typical geometries of Van der pauw method. From [126].

Fig. 4.3 shows one example of the electron concentration of the samples on the reciprocal temperature scale obtained by van der Pauw method at IKZ institute. The electron concentration of the samples were obtained to be 2 to 3×10^{17} at room temperature, and around 1.5×10^{17} at temperature around 150 K. In order to study metal-In_2O_3 contacts, the metals were evaporated on the studied crystals at these two temperatures which will be discussed in the next chapters. For more and detailed

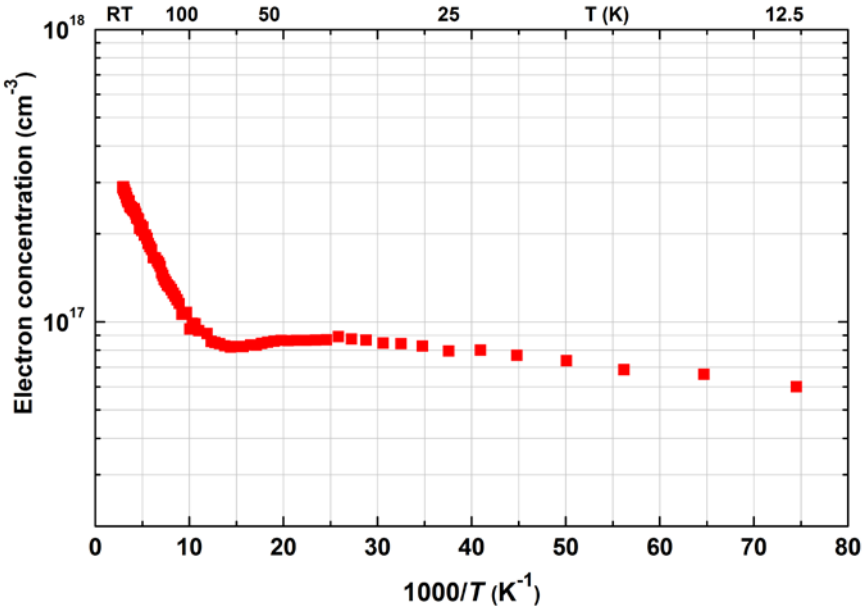

Figure 4.3: The electron concentration of the melt-grown In_2O_3 bulk single crystals on the reciprocal temperature scale, measured by Dr. Kalus Irmscher at IKZ using van der Pauw.

information about the transport properties of the studied crystals, the reader is referred to Ref. [61].

4.2 The optical properties of In_2O_3

The widely cited-band gap of In_2O_3 is around 3.75 eV [6]. Recently, a weaker optical absorption was observed in this material, not only in polycrystalline thin films [133], but also in the single crystalline ones [70]. This identification challenged the widely reported-band gap, and shows that it is 1 eV smaller. The stronger absorption was described as direct-allowed transitions [6], while the weak one was interpreted as parity-forbidden transitions [3]. If this onset at lower energies is because of the direct or partly indirect transition, is still controversially discussed [4]. This section is devoted to outline the optical transmission measurement and determination of the band gap of the In_2O_3 bulk single crystals using this measurement.

4.2.1 Fundamental absorption

The photo-excitation of electrons from the valence band to the conduction band is named fundamental or interband absorption. There are two types of absorption: direct and indirect ones. If the maximum of the valence band and the minimum of the conduction band have a same crystal momentum in the Brillouin zone, the semiconductor is direct band gap, otherwise it has an indirect gap. These two classifications are illustrated in the Fig. 4.4. Indirect transitions are accompanied by phonons absorption or emission to fulfil the momentum conservation.

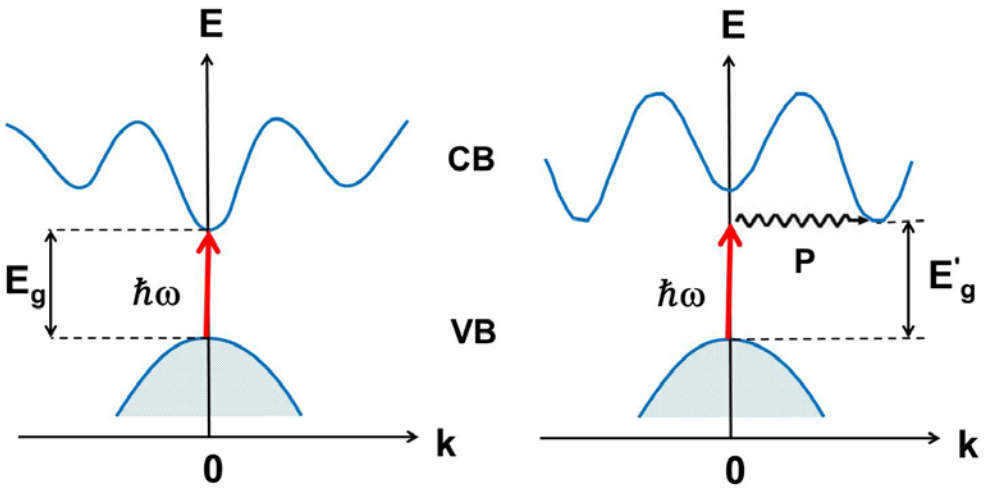

Figure 4.4: Schematic diagram of the band structure of a direct and an indirect band gap semiconductor, left and right, respectively [132].

4.2.2 Optical transmittance

The optical properties of TCOs can be studied by optical transmission and reflection measurement using UV-Vis spectrometer. By performing the measurement of transmittance as a function of wave length (λ), one can determine the absorption coefficient α (λ) and accordingly the band gap of the sample. The transmittance T (λ) and reflectance R (λ) are the fractions of the incident light which are transmitted and reflected, respectively. In this measurement the specimen is in normal incidence of the light, considering this point as well as the equality of the front and back reflection coefficient leads to the following equation for absorption coefficient [134, 135]:

$$\alpha = -\frac{1}{d}\ln\left[\frac{\left(\sqrt{(1-R)^4 + 4T^2R^2} - (1-R)^2\right)}{2TR^2}\right] \tag{4.9}$$

where d is the sample thickness. Reflectance can be determined by knowing the refractive index n and using the equation:

$$R = \frac{(n-1)^2}{(n+1)^2} \tag{4.10}$$

The optical band gap can be acquired by evaluation of the absorption coefficient as a function of energy. Near the band edge, a parabolic-band dispersion can be assumed for

the density of states. Therefore, the incident photon-energy dependence of the absorption coefficient for direct transitions is expressed by [136, 137]:

$$\alpha(h\upsilon) \propto (h\upsilon - E_g)^r \tag{4.11}$$

here, E_g is the band gap, and the power r=1/2 for parity allowed transition and r=3/2 for forbidden ones. The power r=1/2 results in the equation (2.2). For indirect transitions, as α depends on the probability of the interaction between electron excitations and phonons, it relates to phonon energy E_p. Hence, α (hν) for indirect transitions is given by:

$$\alpha(h\upsilon) \propto (h\upsilon - E_g' \pm E_g)^r \tag{4.12}$$

where r=2 for allowed transitions and r=3 for forbidden ones, and E_g' is indirect energy band gap [138].

In the present study, the optical transmittance measurement was performed in UV-Vis ranges at room temperature by means of a double beam spectrometer (Perkin-Elmer Lambada 25) with spectral resolution 1 nm. The sample thickness d was around 500 μm. The result is plotted in Fig.4.5. One can realize a sharp absorption edge at wave length of 440 nm, and the transparency of the sample in visible range from this figure.

The equations (4.9) and (4.10) were used to obtain reflectance and absorption coefficient, respectively. The refractive index was determined using the one-term Sellmeier equation [139] ($1/(n^2-1)=-A/\lambda^2+B$), where $A=133\times10^{-16}$ m^2 and B=0.3340 from Ref. [140].

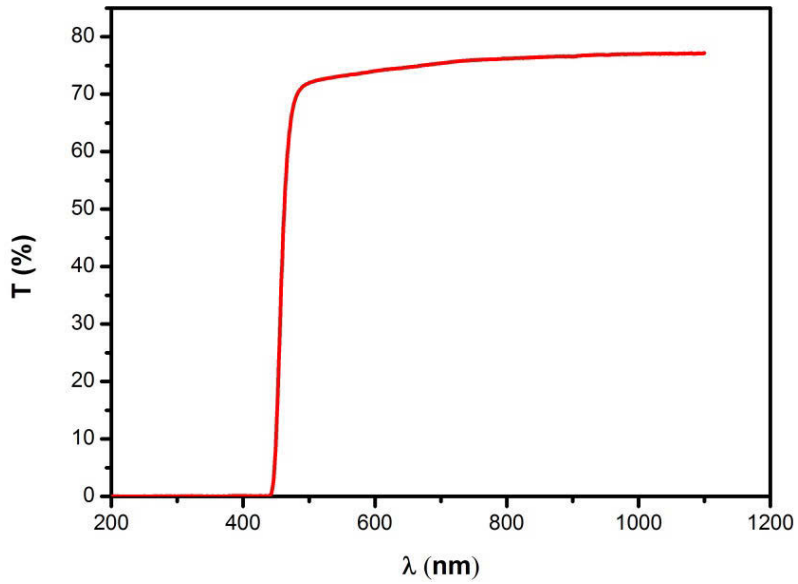

Figure 4.5: Transmittance of melt-grown In_2O_3 bulk single crystal at room temperature. A sharp absorption edge at λ=440 nm is observable.

Walsh demonstrated that a weak contribution to photon absorption corresponds to a parity forbidden transition with the optical transition matrix-element becoming zero for direct transition at Γ-point of the Brillouin zone of the bixbyite structure, which contains an inversion center. Therefore, he ascribed this weak onset (Γ_4-Γ_1) transition to the forbidden one [3].

Whether this forbidden transition is direct or indirect is still controversial. Weiher et al. [70] attributed the weak absorption to an indirect forbidden transition where the CBM is located at Γ−point , and the energy difference between the VBM and the top most of the valence band at Γ is about 1 eV. However, different experimental and theoretical works show that the transition is direct [5, 55, 108, 141] or slightly indirect (maximum of the valence band is less than 50 meV away from the highest occupied level at Γ-point) [142]. Accordingly, we considered this onset as forbidden-direct transition for the band gap determination. By applying the equation (4.11) and r=3/2 for the parity forbidden transition, the spectral dependence $\alpha^{2/3}$ is plotted in Figure 4.6.

From the data linearization, the optical band gap was obtained to be around 2.8 eV, which is in very good agreement with the value obtained from References [4, 5, 74, 96, 109].

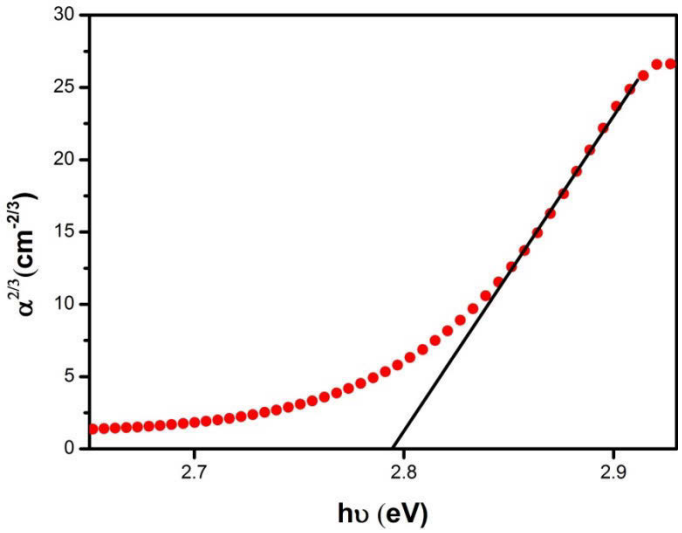

Figure 4.6: Absorption coefficient to power 2/3 as a function of photon energy.

Chapter 5
Photoelectron spectroscopy

5.1 Introduction

Photoelectron spectroscopy or photoemission spectroscopy (PES) is a standard direct technique used to study the electronic structure, i.e. how the electrons are distributed in solids and on their surfaces. This experimental method is based on the photoelectric effect, the extraction of electrons induced by incident radiation and detection of their intensity as a function of the kinetic energy. The photoelectric effect was discovered by Hertz in 1887 [143], and it was the first evidence for quantization of light, as elucidated by Einstein in 1905 [144]. At the time, the experiment was performed by using a light monochromatized by a prism spectrograph and the determination of the kinetic energy of the liberated electron was obtained by measuring the voltage required to overcome the current across the vacuum vessel [145]. The method has since then made great advancement. Three physical quantities: Energy (E), momentum (**k**) and spin (s) fully define the electronic state of a material. The only tool able to investigate all of these quantities at the same time is angle-resolved photoemission spectroscopy (ARPES), which is the refinement of the initial experiments on the photoelectric effect.

In this chapter, a general introduction to the theoretical aspect of ARPES will be presented at first. Next, some remarks regarding the experimental laboratory and setup and sample preparation will follow. A comprehensive and detailed review regarding the PES can be found in references [145-149].

5.2 Basic concepts of photoemission spectroscopy

5.2.1 The photoemission process

When light of sufficient energy impinges a sample, some electrons are removed from it, are emitted and their intensity (number of electrons per second) is measured as a function of their kinetic energy E_{kin} and emission angles ϕ, θ. The schematic setup of the ARPES is illustrated in Fig. 5.1. The outgoing electrons can leave the sample with the maximum kinetic energy $E_{kin,max}$ which is given by following equation

$$E_{kin,\max} = h\nu - \Phi \tag{5.1}$$

where h, ν and ϕ are respectively Planck's constant, the photon frequency and work function of the solid.

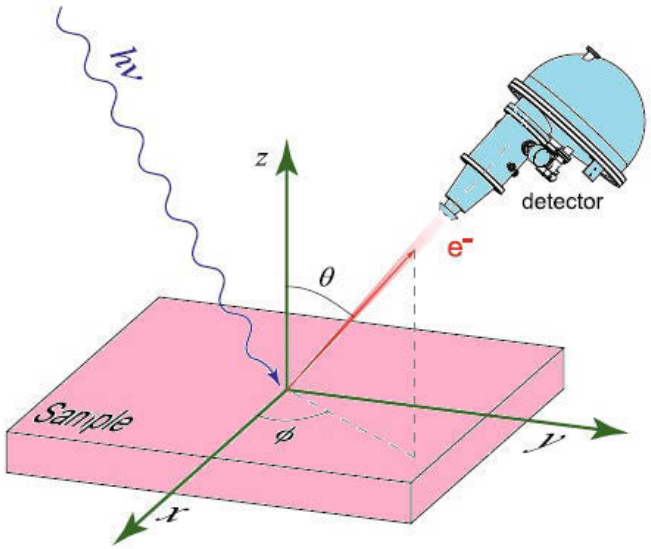

Figure 5.1: A sketch of angle-resolved photoemission spectroscopy. Incident Photon with energy hν extracts electrons from the sample, and electrons are detected regarding their kinetic energy and emission angles ϕ, θ. Taken from [150].

If the incident photon has high enough energy, it can remove electrons from the energy state below the Fermi energy E_F with binding energy E_B. Hence, the kinetic energy is obtained by

$$E_{kin} = h\nu - \Phi - |E_B| \tag{5.2}$$

The momentum of the emitted electrons is determined by

$$p = \sqrt{2mE_{kin}} \tag{5.3}$$

where m is the free electron mass. The direction of the wave vector (**p**/ħ) of the emitted electron is determined from the emission angles [145]. Figure 5.2 shows the schematic image of photoemission process in single-particle picture. This figure illustrates the energy level in the sample on the left side, and the energy distribution of the liberated electrons

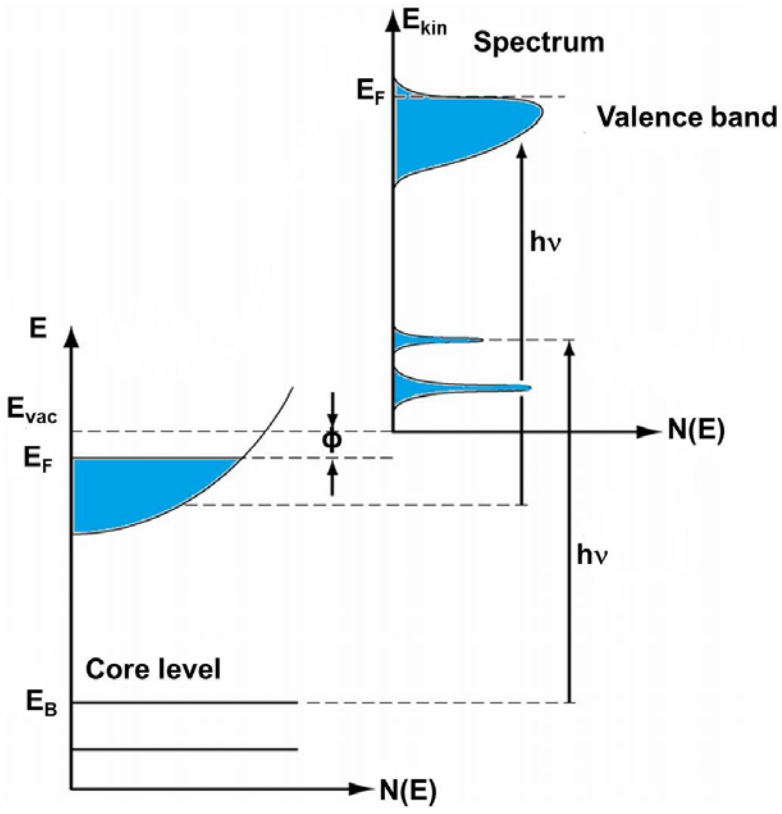

Figure 5.2: The sketch of energy levels in photoemission spectroscopy [145]. The vacuum, Fermi and binding energies are denoted by E_{vac}, E_F and E_B, respectively.

which were excited by photon energy of hυ on the right side. The kinetic energy of zero corresponds to the vacuum level of the solid.

The PES spectrum reflects the electronic states of the studied sample, and it is analyzed to obtain information about the initial states of electrons using different theoretical models. In the following subsection, one of the models, so-called three step model which explains photoemission process is outlined.

5.2.2 Three-step model

The useful three step model is the most common description which is used to interpret the photoemission process. Also, a sudden approximation is assumed here. In fact, the interaction between excited electron and the (N-1)-electron system is disregarded in this model.

In three step model, PE process is considered as three independent and consecutive steps:

1- Photoexcitation of the electron from an occupied initial state to unoccupied final state.
2- Transport of the electron to the surface.
3- Escape of the electron through the surface to the vacuum.

Figure 5.3 shows the steps of this model. These steps will be discussed in more detail in the following.

Photoexcitation of the electron

In the first step, electron is excited from an initial to a final state as a result of its interactions with the electromagnetic radiation. The transition probability ω_{fi} of the optical excitation of the electron from an initial state with the N-electron wave function of $|\Psi_i>$ and energy E_i to a final state with the N-electron wave function $|\Psi_f>$ and energy E_f can be calculated by using Fermi's Golden rule:

$$\omega_{fi} = \frac{2\pi}{\hbar} \left|\langle \Psi_f(\mathrm{k}_f)|H|\Psi_i(\mathrm{k}_i)\rangle\right|^2 \delta(E_f^N - E_i^N - \hbar\omega) \qquad (5.4)$$

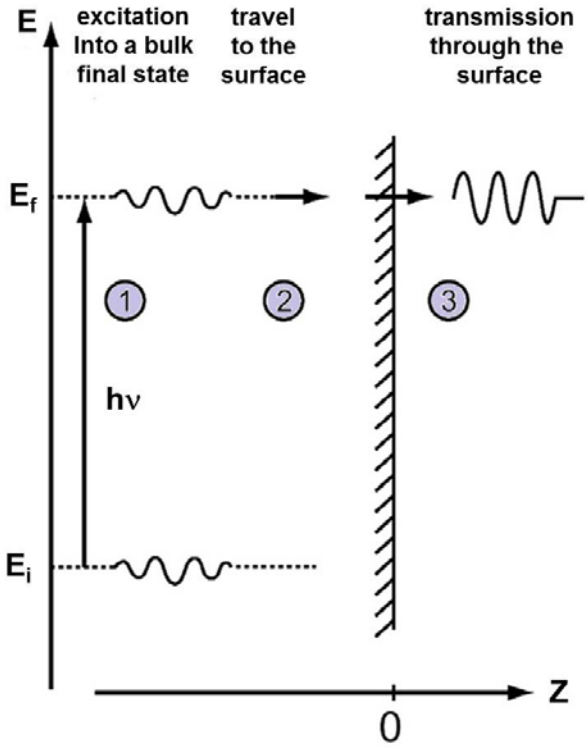

Figure 5.3: Three-step model [145].

The Hamiltonian operator H describes the interaction of the electron with the electromagnetic field of the incident light. Applying perturbation theory leads to the following equation for Hamiltonian operator:

$$H = \frac{e}{2mc}\left(\vec{A}\ .\vec{p}\ + \vec{p}.\vec{A}\right) - e\Phi + \frac{e^2}{2mc^2}\left(\vec{A}\ .\vec{A}\right) \tag{5.5}$$

here, $\vec{A}$ and Φ are vector and scalar potentials, and $\vec{p}$ is electron momentum. By selecting the gauge Φ=0, and using the relation $\left(\vec{A}\ .\vec{p}\ + \vec{p}.\vec{A}\right) = 2\ \vec{A}\ .\vec{p} + i\hbar\left(\nabla.\vec{A}\right)$ and the assumption $\nabla.\vec{A} = 0$ and also neglecting the last term of equation (5.5), surface photoemission term, it results in [145]:

$$H \cong \frac{e}{mc}\ \vec{A}\ .\vec{p} \tag{5.6}$$

To avoid complications, in this model it is assumed that the final state represents an excited electron in the solid, so initial and final wave functions are bulk Bloch waves. Therefore, the internal distribution of excited electron is given by [145]:

$$N_{int}(E,\hbar\omega) \propto \sum_{f,i}\left|M_{if}(k)\right|^2 \delta\left(E_f - E_i - \hbar\omega\right)\delta\left(E - \left(E_f - \Phi\right)\right) \tag{5.7}$$

$|M_{if}(k)|$ is the one-electron dipole matrix element of the transition.

Transport of the electron to the surface

Electrons suffer from inelastic electron-electron and electron-phonon scattering during their travel through the sample to the surface, which results in a continuous background in the lower kinetic energy side of the spectrum. The background is frequently neglected or removed using a Shirley-type approach [151]. Of the many inelastic decay channels available, the electron-phonon scattering dominates at low interaction energies, while the electron-electron interaction plays a considerable role in the determination of the mean free path of the electrons λ [145]. For the energies of interest (5 to 5000 eV), the behavior of photoelectrons in the solid can be estimated as free electron gas. Thus, the inverse of the mean free path depends on the mean electron-electron distance r_s as a following universal function [145]:

$$\lambda^{-1} \approx \sqrt{3}\frac{a_0}{E_{kin}} r_s^{\frac{-3}{2}} \ln\left[\left(\frac{4}{9\pi}\right)^{\frac{2}{3}} \frac{E_{kin}}{R} r_s^{2}\right] \qquad (5.6)$$

where a_0 and R are Bohr radius and Rydberg energy, respectively: a_0=0.529 Å and Rydberg energy R=13.6 eV. In the equation (5. 6), the electron-electron distance r_s is applied in the unit of a_0. Fig. 5.4 shows the mean free path of electrons versus their kinetic energy for different elements.

As depicted in this figure, the mean free path does not relate to the material, and the curve is therefore called universal curve. One can see that the curve has a broad minimum around the energies (20 to 100 eV). The PES is usually conducted in this range of energies, where λ~5 to 10 Å. Thus, it is possible to probe solely the first atomic layers and the surface of the materials in this energy regime. The surface sensitivity of the photoelectron spectroscopy necessitates the ultra-high vacuum (UHV) conditions for the experiments.

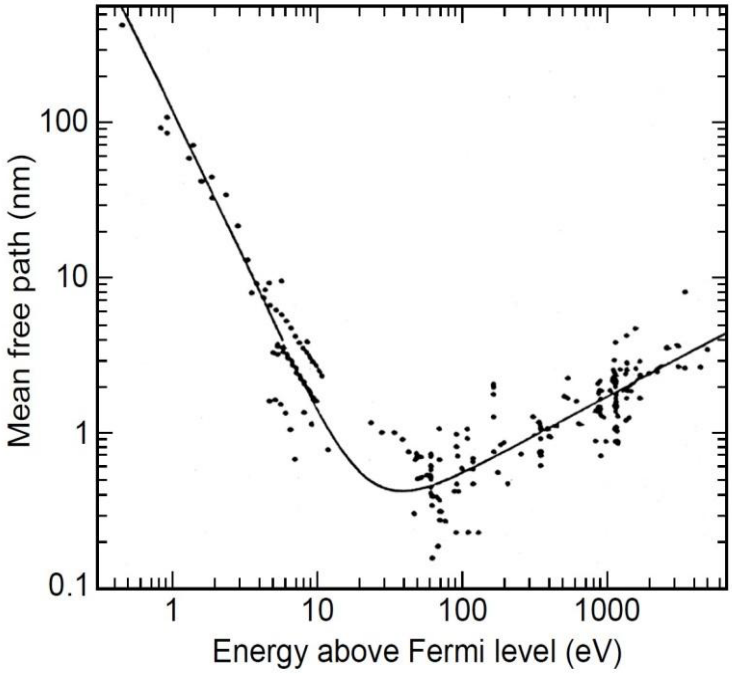

Figure 5.4: Mean free path of electrons versus their kinetic energy for various elements [152].

Escape of the electron through the surface to the vacuum

In the free electron final state approximation which is used in the three step model, the final Bloch states in the solid are estimated by nearly-free electron parabola. When an electron reaches the surface and escapes to the vacuum, it experiences diffraction at the surface because of the potential step. The refraction can be described using a simple model, which is schematically represented in Fig. 5.5. In this concept, it is assumed that the potential changes merely in the z-direction. The electrons with high enough kinetic energy can overcome the potential and escape to vacuum. In order to overcome the potential step, their kinetic energy fulfills the following condition:

$$(\frac{\hbar}{2m})k_{\perp}{}^{2} \geq eV_0 \tag{5.7}$$

where V_0 and $k_{\perp}$ are inner potential and the perpendicular component of the outgoing electron's wave vector. The parallel component of the excited electron to the surface in the solid $k_{\parallel}$ is conserved ($k_{\parallel} = K_{\parallel}$). The wave vector of the photoelectron outside the sample K is expressed as the wave vector of a free electron. Therefore, the parallel

component of the wave vector inside and outside of the crystal can be directly determined by

$$k_{\parallel} = K_{\parallel} = \frac{1}{\hbar}\sqrt{2mE_{kin}}\ \sin\theta \tag{5.8}$$

However, the perpendicular component of the wave vector changes because of the potential difference. The perpendicular component of the wave vector in the crystal is described by:

$$k_{\perp} = \sqrt{\frac{2m}{\hbar^2}(E_{kin}cos^2\theta + |V_0|)} \tag{5.9}$$

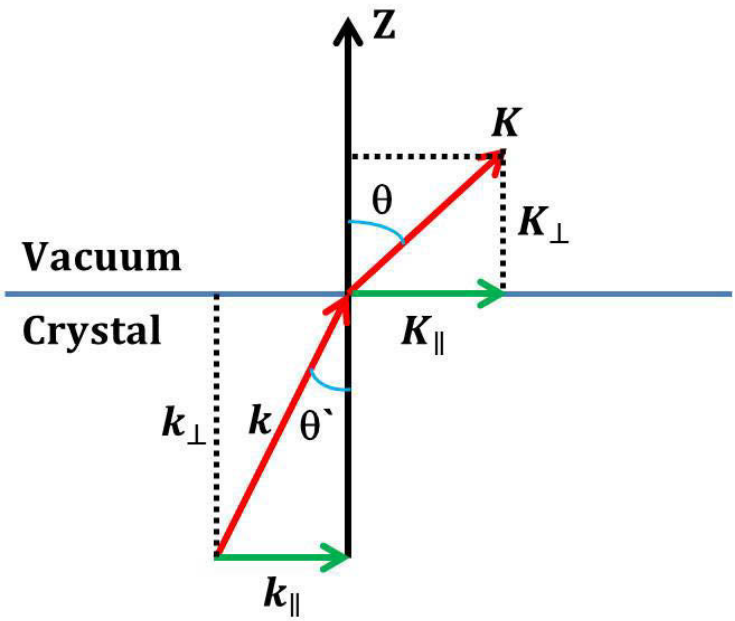

Figure 5.5: Refraction of the outgoing electron at the crystal-vacuum interface. The parallel component of the wave vector to the surface is only conserved. From [145].

5.3 Experimental setup of ARPES

5.3.1 Light sources

Two main light sources are usually used in ARPES experiments: 1- Lab based light sources, e.g. gas-discharge lamps, 2- Synchrotron radiation. In the present work, PES measurements were conducted using the synchrotron light source at the storage ring BESSY II (Berliner Elektronen Speicherring für Synchrotronstrahlung), which will be discussed briefly in the following. This storage ring is one of the existing third generation synchrotron radiation sources in Germany [153].

Synchrotron light is produced in a storage ring by accelerating the electrons to near the speed of light and forcing them on a curved trajectory using a magnetic field. These sources usually provide electromagnetic radiation in a wide range of energies from infrared to the X-ray regimes

Despite the high resolution of lab-based lamps which can be as low as 1 meV for He I radiation and 0.4 meV for the Xe radiation, they have a relatively low flux, but most importantly a fixed emission-energy. On the other hand, synchrotron sources benefit from higher flux, brilliance and energy tunability. Figure 5.6 (a) displays the electron storage ring of synchrotron radiation and the beamlines of BESSY II schematically. The electrons are generated by thermal emission from a filament and then they are accelerated in different stages: in a vacuum linear accelerator called microtron and the circular booster synchrotron. After being accelerated to their final energy of 1.7 GeV, the electrons are injected into the storage ring. In the storage ring, the electron beam is kept circulating with constant energy and the energy losses resulting from the scattering with the residual gasses, with the radiation emission or electron optics imperfections are supplied back in the radiofrequency cavities. The storage ring of BESSY II has constant beam current of around 300 mA and uses a top-up mode operation, i.e. continuous compensation of the lost electrons. The electron beam motion is controlled by a series of magnetic field devices obtained by dipole magnets, and insertion devices (undulators), in which a periodic alternating magnetic field let the electrons move in a slightly zig-zagging way. Dipole magnets accelerate radially the electrons leading to a radiation

emission from the electron bunches tangent to the electron trajectory. Therefore, a fan-like region is included in the resulting radiation [138], See Fig. 5.6 (b). Contraction of the synchrotron radiation to a small angular fan because of the relativistic speed of traveling electrons in the synchrotron leads to much higher intensity of the beam compared to that in lab-based light sources.

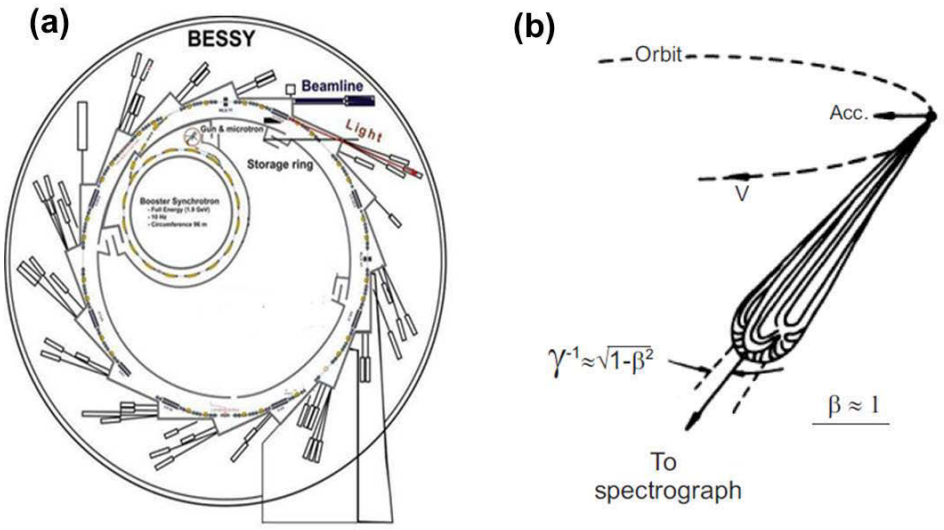

Figure 5.6: (a) Schematic representation of the photon source BESSY II [150]. (b) Radiation characteristic of an electron moving in a circular orbit at high speed. The angular distribution of the emitted electromagnetic radiation peaks at high speeds in the forward direction [145].

5.3.2 The BEST beamline

The present study was performed at the beamline BEST (Beamline for Education and Scientific Training) of BESSY II. Photons in the UV and VUV energy range are generated by a diploe magnet and monochromatized in the 5-40 eV are normal-incidence monochromator (NIM) with a deflection angle $2\theta=4°$ and focal length of 5 meters. The resolving power of the beamline $\Delta E/E>20.000$ and the spot size at the sample is 20µm×120 µm at photon energy of 21 eV. Fig. 5.7 demonstrates an optical sketch of the beamline. The pre-monochromator optics consists of two mirrors (M_1 and

M_2). The first mirror M_1 is a 1 m long toroid, which is situated 12.5 m away from the dipole magnet source. Its role is production of an intermediate vertical and horizontal focus in 12.5 and 13.6 m, respectively. Water cooling keeps it at constant temperature of 22 °C.

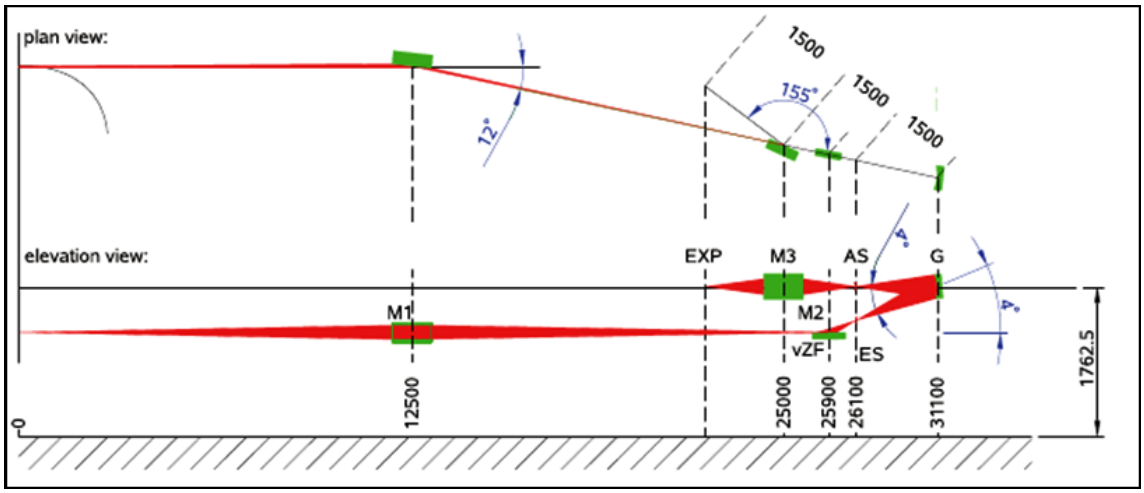

Figure 5.7 Optical lay-out of the 5m-NIM beamline, The grating, entry and exit slits are denoted by G, AS and ES, respectively [154].

The second mirror M_2 is a plane ellipse (130 mm×20 mm) and produces a line focus on the entrance slit in 0.2 m distance. The entrance slit operates according to two parallelograms and one trapezoidal guide, and its size can be changed in the interval of 0-3500 µm by a micrometer screw. The toroidal mirror M_3 is a refocusing mirror and located 1.5 m after the exit slit.

The concave grating unit is placed 5m away from the entry and exit slits, which are set in the fixed positions [154]. The wave length of the diffracted light is adjusted by rotation of the grating in vacuum based on the off-Rowland circle to reach the user desired photon energy. The grating chamber position can be vary up to 300 mm by translational movement of that in the direction of the incoming light, which determines in fact the degree of focusing [155].

The light is diffracted by the grating according to the following equation:

$$\lambda = \frac{1}{mN} \left(\sin\alpha + \sin\beta \right) \tag{5.10}$$

where m, N, α, and β are deflection order, the density of grating, incoming and outgoing angles. The wave length of the diffracted light and accordingly its energy is set through changing the incoming and outgoing angles with respect to the normal to the grating. The rotation angle is constrained from -2 to 20°. The photon-energy dependency of the intensity of 5m-NIM is shown in Fig. 5.8. The maximum intensity is obtained to be around 19.7 eV. A view of the 5m-NIM is displayed in figure 5.9.

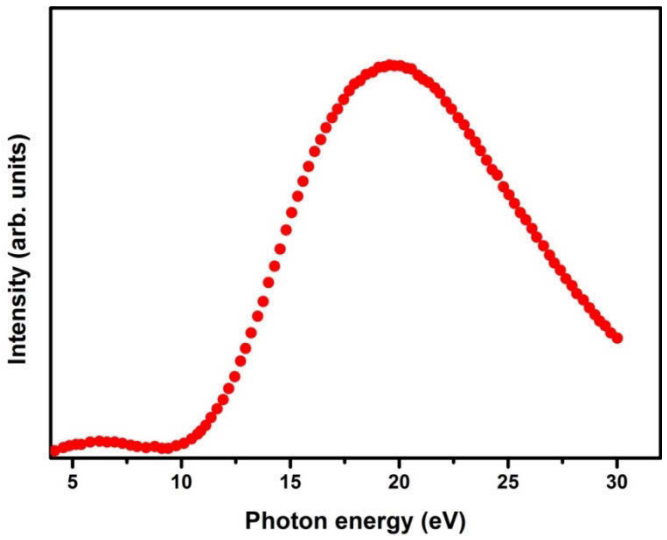

Figure 5.8: Intensity distribution of the 5m-NIM monochromator.

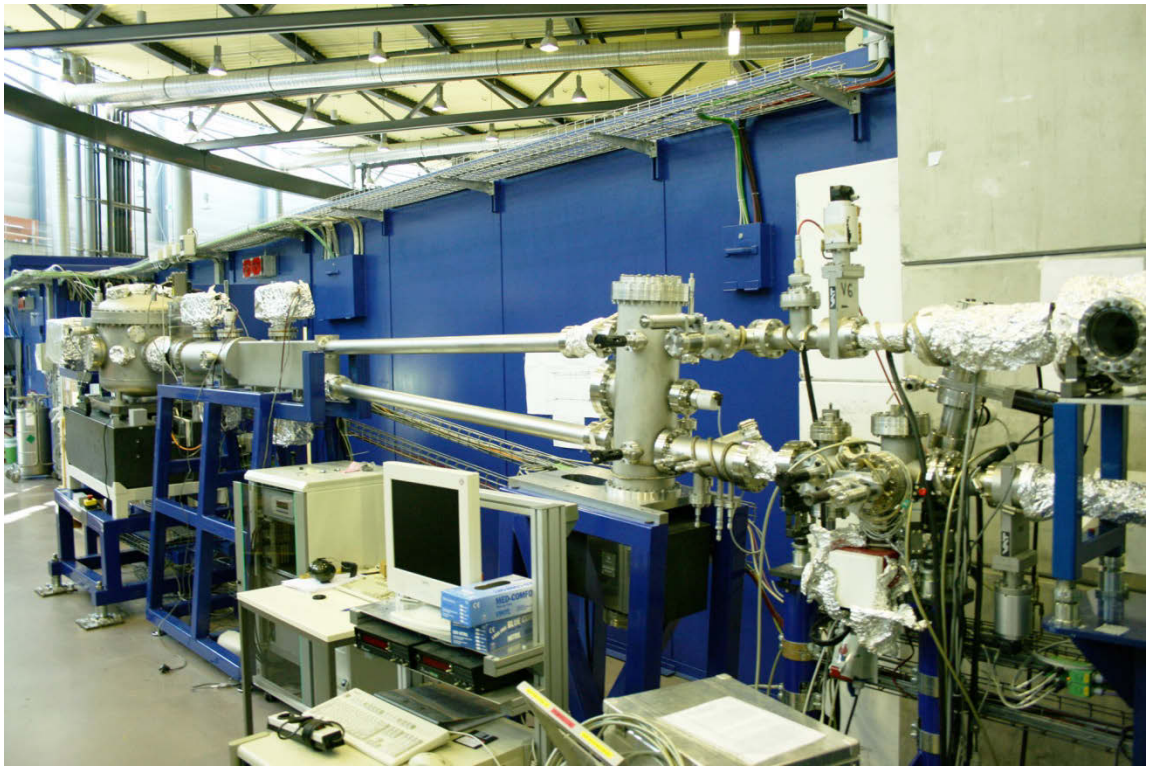

Figure 5.9: The 5m-NIM beamline. The UHV chamber at the end is the chamber for three gratings.

5.3.3 Electron energy analyzer

The photo-excited electrons from the sample are collected within a finite acceptance angle and energy resolution according to their kinetic energy and emission angle. On the BEST beamline a hemispherical analyzer is used. Hemispherical analyzers consist in electron lenses, a hemispherical energy filter and nowadays a 2D-multi channel plate (MCP) detector. Electron lenses sort the electrons with respect to their emission angles and decelerating the photoelectrons through retarding electric field. The electrons are decelerated to the energy which is known as pass energy E_P. The hemispherical energy filter is the half of a spherical capacitor, which arranges and separates photoelectrons according to their kinetic energy. It includes two concentric hemispherical electrodes with inner and outer hemisphere radii of R_1 and R_2. The electrostatic field is generated by applying voltage to the hemispheres. The voltage difference V relates to the pass energy E_P by following formula [156]:

$$V = \frac{E_p}{e}\left(\frac{R_2}{R_1} - \frac{R_1}{R_2}\right) \tag{5.11}$$

It is set when the user enter the E_P value in computer. The 2D-MCP detector is located at the exit plane and enhances the counting rate of electrons by a 2D-array of electron multipliers. In fact, it enables a simultaneous measurement of photoelectrons with different kinetic energy and angle or spatial origin from the sample surface [157]. The multiplied electrons stimulate and illuminate a phosphor plate on which the image of the electronic distribution is formed and recorded by charge-coupled device (CCD) camera. Figure 5.10 represents a schematic image of the conventional hemispherical analyzer.

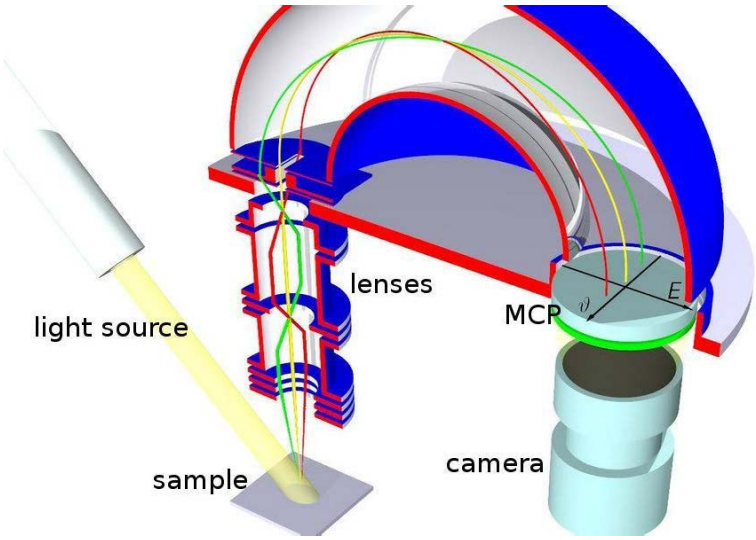

Figure 5.10: The Principle of the hemispherical analyzer. From [158].

The energy resolution of a hemispherical analyzer is determined by:

$$\Delta E_A = E_p\left(\frac{s}{2R} + \frac{\Delta y}{2R} + \alpha^2\right) \tag{5.12}$$

where $R=(R_1+R_2)/2$, and s, Δy and α are the mean slit width of the analyzer, the ability of the detector two resolve two points of the distance of Δy and the analyzer half acceptance angle in the dispersion direction. The ARPES apparatus of the BEST beamline is equipped by a Scienta SES2002 analyzer [159] whose mean radius R=200 mm, $\alpha \approx 6^{\circ}$. In this study the slit size 0.5 mm and the pass energy of 5 eV were used to

record the spectra. For ideal detectors, Δy and also α can be considered to be zero. By above-mentioned values and applying equation (5.12), the energy resolution analyzer ΔE_A is obtained to be 6.25 meV.

5.3.4 Experimental-end station setup

The ARPES apparatus is constructed by the PREVAC ltd. Company [159]. It consists in three different UHV chambers: the load lock, distribution chamber (UFO) and the analysis chamber. A schematic diagram of the ARPES apparatus of the BEST beamline is illustrated in Fig. 5.11.

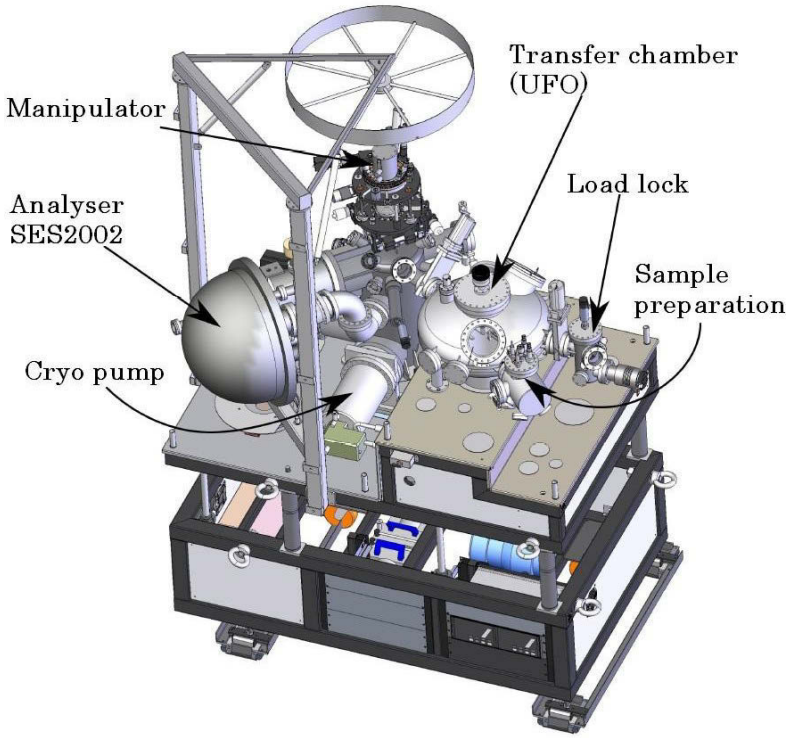

Figure 5.11: The experimental-end station of the 5m-NIM [159].

The samples are introduced to the vacuum from the load-lock. It contains a carousel with six sample-storage positions. The UFO locates between the load-lock, preparation and analysis (main) chambers. This chamber is used for sample transfer between mentioned chambers. The main chamber is equipped by a cryogenic manipulator with 5-dgrees of freedom. The sample can be translated along the three x, y, z axes and also rotated about two axes perpendicular to each other and lying in the sample surface

directions. A closed-cycle He cryostat allows the variation of temperature between 20 K and room temperature. The base pressure of the main chamber, UFO and load-lock are 2×10^{-10}, 5×10^{-10} and 5×10^{-8} mbar. In the preparation chamber, it is possible to evaporate metals from tungsten coil and study metal contacts on the samples.

5.3.5 Sample preparation for ARPES measurements

As mentioned in previous chapters, the azimuthal orientation of the (111) plane of samples was determined by Laue method in order to identify scanning orientation. The specimens were oriented along their Γ-N crystallographic direction. They were stuck on the Al-sample screws using a two-component silver epoxy glue to achieve good ohmic contacts. To obtain clean surface, the samples were cleaved parallel to (111) planes in the main chamber and under UHV condition better than 2×10^{-10} mbar. A piece of the Al-cleaver was glued on the samples to cleave the samples, see Fig. 5.12. The analysis of the surface properties of the cleaved samples revealed atomically flat surfaces of them by means of scanning tunneling microscopy as discussed in this thesis earlier.

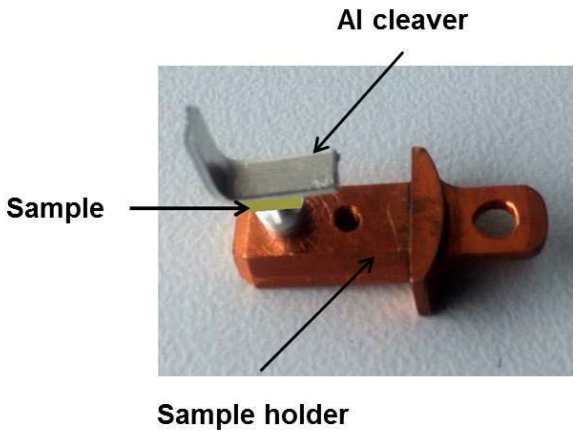

Figure 5.12: The copper sample holder with an In_2O_3 sample on that, Al cleaver is used to cleave the samples parallel to (111) planes in the UHV condition.

As the surface of a semiconductor may be charged electrostatically upon photon beam irradiation under UHV condition, a valence band spectrum of In_2O_3 was measured at different photon beam intensities to insure the absence of the charging effect. Since the

current of storage ring at BESSY II is constant, the photon intensity was varied by changing the size of the entry and exit slits of the beamline. The photon flux was measured by a photodiode located close to the third mirror of the beamline. Figure 5.13 represents the normalized valence band spectra of the In_2O_3 sample at different photon flux. As depicted in this figure, no shift was observed by changing the photon intensity in ARPES experiment.

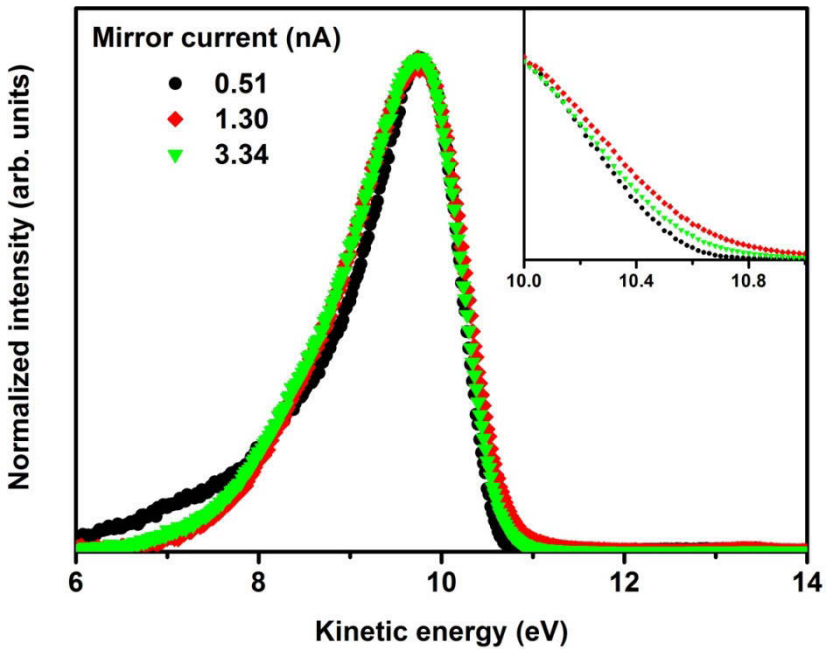

Figure 5.13: The normalized valence spectra of the melt-grown In_2O_3 at different photon intensities, revealing the absence of the charging effect and accordingly proper ohmic-back contact of the samples. The inset shows the spectra in kinetic energy between 10 to 11 eV.

5.4 Data processing

ARPES provides information about the electronic properties of the occupied states of materials. In this study, energy distribution curves (EDCs) were used to perform photoemission spectroscopy. The kinetic energy dependence of the outgoing electron intensity is measured at constant excitation energy by this mode. The photoemission

spectra are referenced to the Fermi level. Therefore, the Fermi energy should be determined.

Fermi energy

The ARPES spectra are in the kinetic energy E_{kin} scale at first, and their scale is changed to the binding energy E_B using the Fermi energy E_F, (E_B=E_{kin}-E_F). The Fermi energy was determined from a thick evaporated polycrystalline gold film. Since the analyzer and gold are in electrical contact, the Fermi energies of the Au film and the analyzer equilibrate. Therefore, the Fermi edge of the sample, which is also electrically connected to the analyzer, is the same. The experimental parameters for the Fermi edge determination like beamline setting, the slit size of detector, temperature and the pass energy should be the same as the spectra which are referenced to the Fermi energy. Figures 5.14 (a) and (b) represent the Fermi edge of the Au film at room temperature and 20 K, respectively, and also the first derivative of the experimentally Fermi distribution in their insets. The spectra were taken at 18 eV. From the Fermi fit function, the Fermi energy was obtained to be (13.58±0.02) eV, and the full width at half maximum (FWHM) was determined to be (21.7±0.5) meV at 20 K and (106.8±0.5) meV at 300 K, See the insets of figures 15.14 (a) and (b). FWHM is the total energy resolution (S_A) which is theoretically given by [138]:

$$S_A = \sqrt{(\Delta T)^2 + (\Delta E_A)^2 + (\Delta E_B)^2} \tag{5.13}$$

where $\Delta T=4k_BT$, and k_B Boltzmann constant and T absolute temperature (here T= 300 and 20 K). ΔE_A and ΔE_B are the analyzer and the beamline resolution. From section 5.2.4 ΔE_A =6.25 meV and From Ref. [160] ΔE_B=6.9 meV. Therefore, S_A is determined to be 11.58 meV at 20 K and 103.82 meV at 300 K.

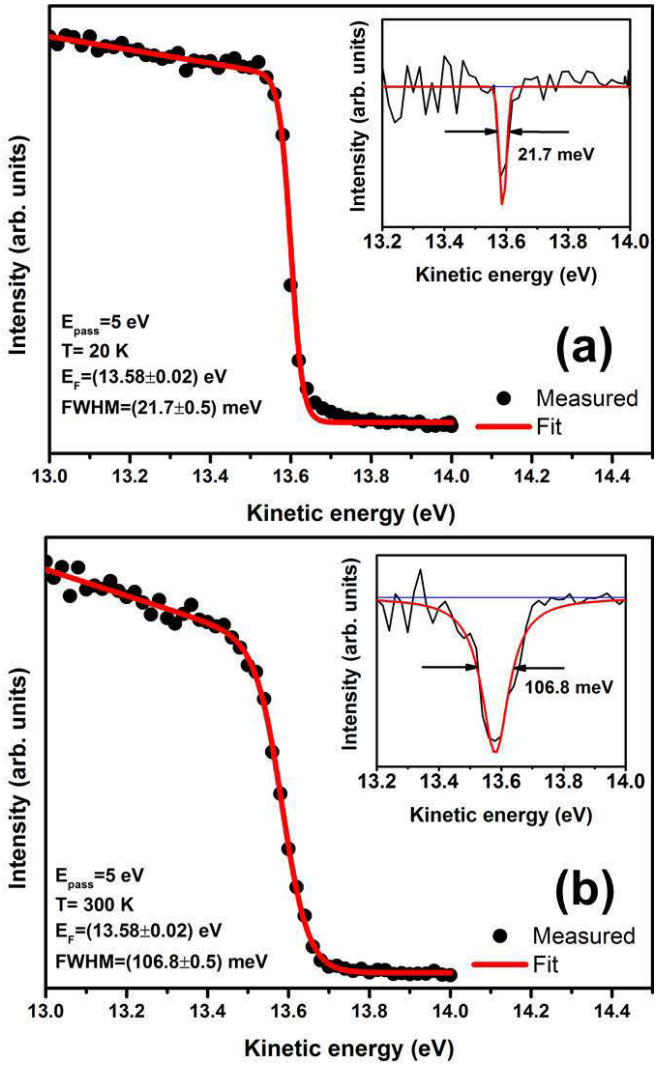

Figure 5.14: EDC spectrum corresponding to the Fermi region (a) at 20 K and (b) at 300 K. The insets show the first derivative of the Fermi steps with a Gaussian fit.

Peak analysis

In order to get accurate information from the spectroscopy, the recorded spectra should be analyzed. The spectral line shape of spectra describes the form of a feature in spectroscopy. Their ideal line shape is commonly Gaussian, Lorentzian, or Voigt. The latter line profile results from the convolution of Gaussian and Lorentzian. Gaussian line shape is the most frequently observed line profile. The Doniach-Sunjic profile is also used for asymmetric line-shape which is usually observed as a result of the instrumental and physical effects, such as the asymmetric response-function of analyzer, non-

monochromatic X-ray induced transition, phonon-broadening or because of the background removal [161].

Resolving the individual bands is not possible in In_2O_3 with large bixbyite unit cell. Thus, it necessitates using a fit procedure to determine peak positions and resolve individual bands. Fig. 5.15 demonstrates an example of the fit result of In_2O_3 valence band. First of all the Shirley background was subtracted from the original spectra, and then the EDC spectra were fit by Gaussians. Similar to the Ref. [5], the main peak of VB can be fitted by three single peaks. The peaks were located at binding energies of -3.64, -4.05 and -4.7 eV.

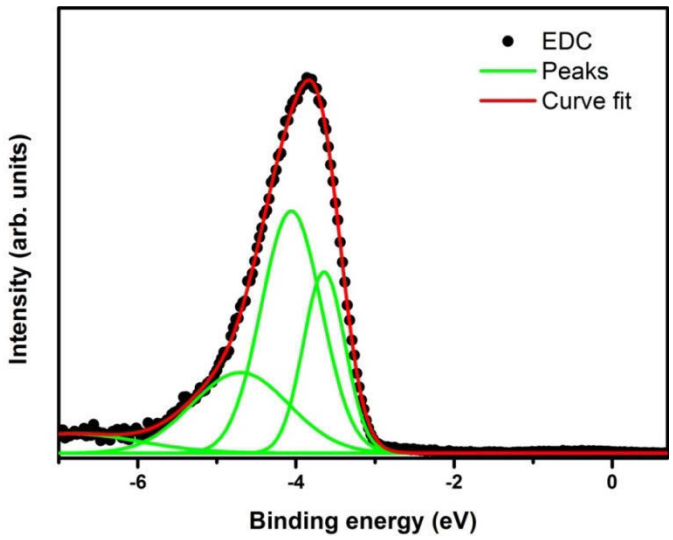

Figure 5.15: EDC spectrum of In_2O_3 taken at photon energy 18 eV, including the global fit of the valence band.

Chapter 6
Electronic structure of In_2O_3

6.1 Introduction

In_2O_3 has become a focus of research due to its wide range of applications, such as solar cells, electrodes for displays, and gas sensors [1, 16]. As discussed in previous chapters, the fundamental band gap of In_2O_3 has recently been found to be around 1 eV smaller [3-5] than the widely cited-band gap of 3.75 eV [6]. The knowledge of the nature and magnitude of the band gap plays a critical role in interpretation of the surface sensitive ARPES spectra and also the study of metal-semiconductor interfaces. Therefore, first a brief introduction into the basic features of electronic structure of In_2O_3 and also surface electron accumulation layer (SEAL) concept will be presented in this chapter. Next the experimental In 4d semi-core level spectra as well as valence band will be discussed.

6.2 Basic aspects of electronic structure of In_2O_3

According to the ionic model, the valence band of In_2O_3 is filled and consists mainly of O 2p band. The VB is separated from the conduction band which is mostly composed of empty In 5s.

The In 4d semi-core levels are located below the main valence band and do not contribute to the bonding. Based on this description, Fan and Goodenough [162] suggested a representation of density of states for In_2O_3. Their concept was approved and improved by other theoretical calculations later [95].

For instance, Fig. 6.1 displays orbital and site projected density of states for In_2O_3 calculated with DFT method and taken from Ref. [108]. In this figure, one can observe that the In and O are not energetically separated, so their bonding is not purely ionic. As depicted in Fig. 6.1 and also schematically in Fig. 6.2 top, the VB of In_2O_3 is composed of three regions: Region I which located deeper than -15 eV from the VBM. The first region has O 2p and In 4d character. In region II, the states are mainly In 4d with small contribution from O 2s and O 2p. In the Region III, the bands derive mainly from O 2p orbitals, from In 5s and from hybridized In 4d and In 5p states. Moreover, a weak feature near the Fermi energy is observable [108]. These results agree well with other band structure calculations [163, 164].

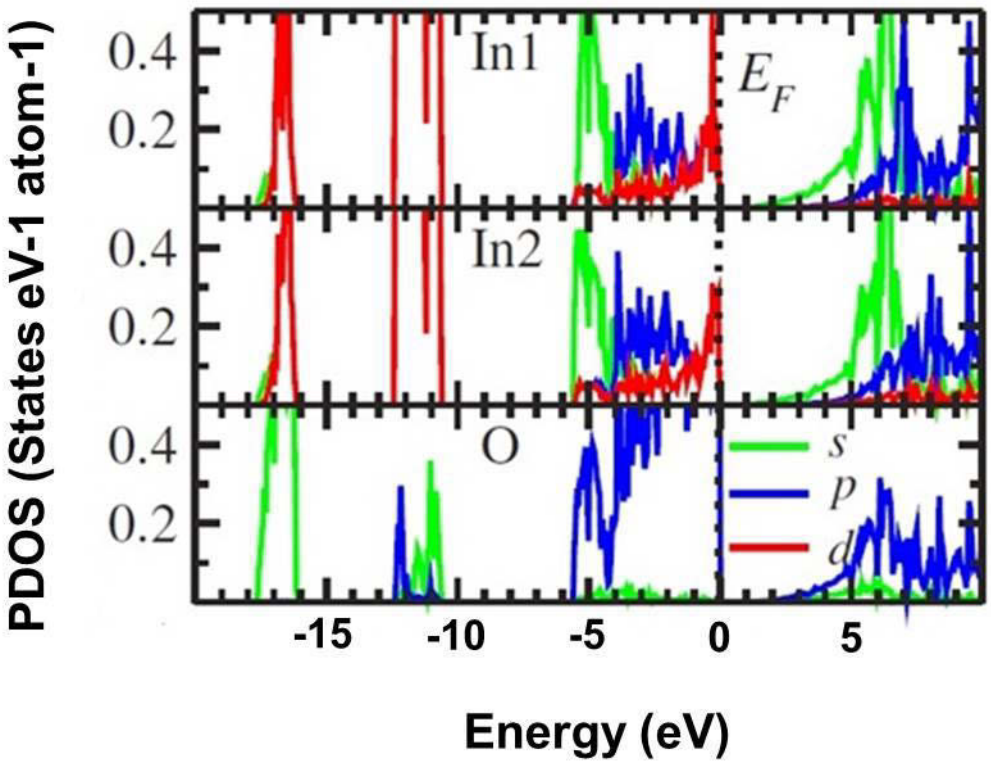

Figure 6.1: Projected density of states for In_2O_3. From [108].

Figure 6.2 represents the VB for In_2O_3 and its schematic separation in the three regions introduced above (top) and the experimental VB spectrum of the melt-grown In_2O_3 by ARPES (bottom). Similar to Ref. [109] and also considering this point that Karazhanov et al. used different point (VBM) as a reference in determination of the peak positions in

the theoretically derived PDOS [108], the region I and III (below -15 eV and the region between -9 to -3 eV) are in good agreement with theoretical predictions.

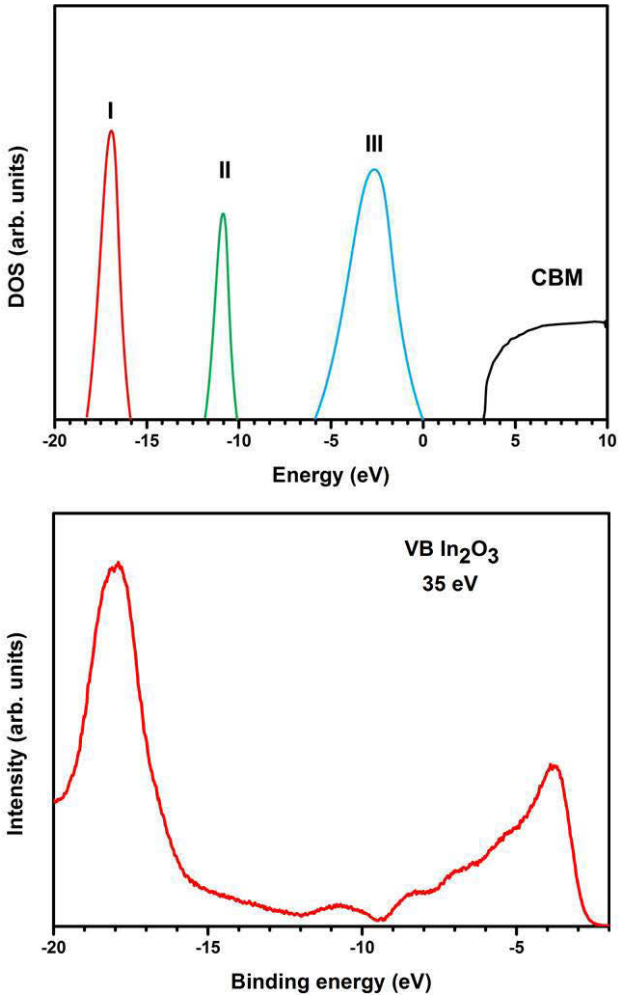

Figure 6.2: Top: the schematic diagram of the projected density of states for In_2O_3 according to the analysis of Karazhanov et al., taken from [109]. Bottom: valence band spectrum of the melt-grown In_2O_3 measured at the BEST beamline with a photon energy of 35 eV.

On the other hand, the second region, similar to Ref. [109], is located around 2 eV in lower binding energies compared to the theoretical prediction. Figure 6.3 displays In4d-shallow core level in the binding energy range of -15 to -21 eV taken at excitation energy of 35 eV. A visual inspection makes clear that the data does not consist in a single peak and actually three were needed to account for it. Some authors report that the states around a binding energy of 18 eV are due to In 4d and O 2s electrons [8, 108], whereas others reported the appearance of O 2s states at around 24 eV [165].

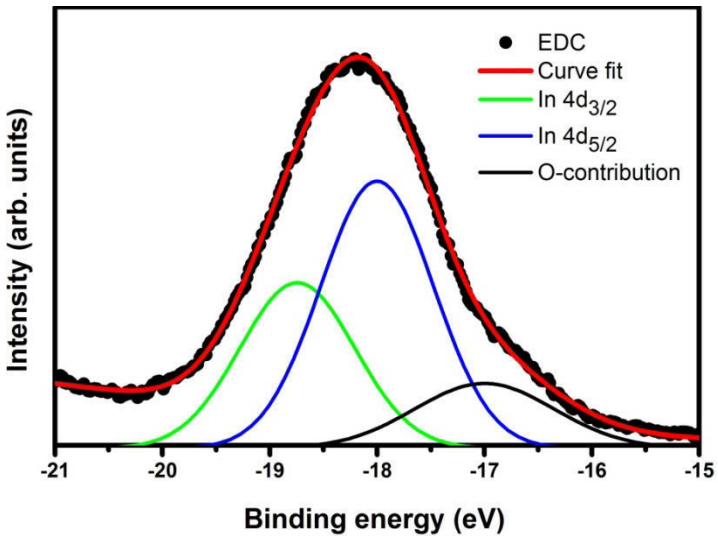

Figure 6.3: Fit results of the In4d spectrum of the melt-grown In_2O_3 taken at photon energy of 35 eV, which consists in three components, the In $4d_{5/2}$-In $4d_{3/2}$ spin orbit doublet and the O-contribution line on the lower binding energy side.

Since the nature of the state at about 17 eV has not been clarified yet, it was considered to be an O contribution instead of the O 2s core level. In order to find the precise energy value of the In 4d line, the complex line shape was fit by Gaussians for three components, the spin-orbit split In $4d_{5/2}$-In $4d_{3/2}$ doublet and the O-contribution core level occurring in the same energy range on the lower binding energy side, see Fig. 6.3. Similar to Ref. [8], constraints of the In $4d_{5/2}$/In $4d_{3/2}$ intensity ratio and spin-orbit separation was considered to be 6/4 basing on electron-counting arguments, and 0.75 eV, respectively. The energy separation of O-contribution and In $4d_{5/2}$ was obtained around 0.9 eV by the best fit.

6.3 The electronic structure of In_2O_3

One of the earliest researches into In_2O_3 was done by Rupprecht in 1954 [3]. He prepared In_2O_3 polycrystalline films by deposition indium metal on a quartz substrate at high temperatures in air. He observed the onset of optical absorption at 3.55 eV. However, Weiher and Ley identified a weaker absorption onset at 2.6 eV in single crystalline In_2O_3 plates grown by a vapor transport technique. They ascribed this onset

to indirect forbidden transitions [70]. The subsequent results of other optical experiments [166, 167], x-ray photoelectron spectroscopy (XPS) [9, 10, 168] and ARPES [5, 109] confirmed that the band gap of In_2O_3 is around 1 eV smaller than the widely-reported one~3.7 eV [6]. Moreover, some recent theoretical calculations have approved the direct [9, 108, 141] or slightly indirect [142] nature of the fundamental band gap of In_2O_3.

Using DFT and many-body perturbation theory (MBPT), Fuchs and Bechstedt [141] obtained a direct band gap of 3.1 eV for the bcc-In_2O_3. This value is obtained by sum of the derived band gap of 2.45 eV and the calculated correction value of 0.65 eV. It is noteworthy that they applied the correction value for rh-In_2O_3, because such a calculation for bcc-polymorph with 80 atoms per unit cell is extremely expensive and time consuming. The discrepancy between the experimental band gap and this value arises from the fact that many effects were neglected, namely excitonic effects, life time and phonon broadening Urbach tailing because of the impurity scattering [95]. Fig. 6.4 demonstrates their DFT-calculated band structure of bcc-In_2O_3 [141]. From this figure, one can see the complexity and weak dispersion of the valence band. The complexity of the bands stems from the large number of atoms in the unit cells and from the hybridization between different orbitals [141]. The flat valence bands are a result of the size mismatch between the cation and anion and high electronegativity of anion [35]. Also, they found that CBM and VBM are placed at the Γ-point and close to this symmetric point, respectively [141].

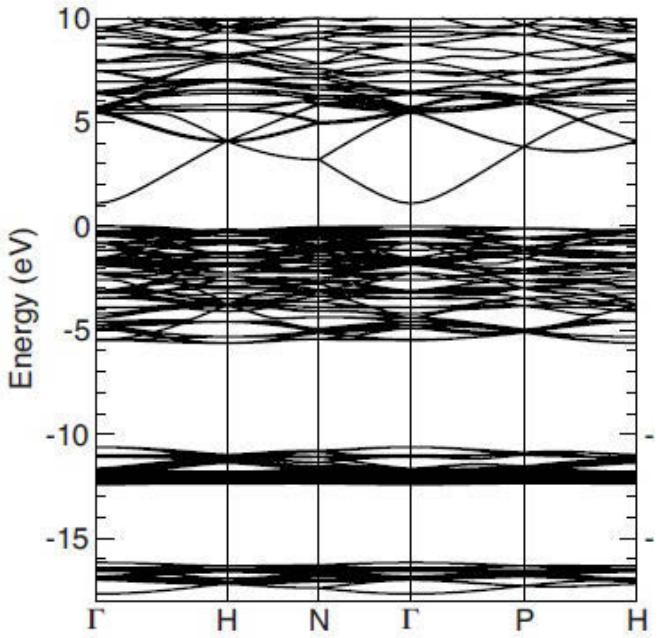

Figure 6.4: Calculated band structure of In_2O_3 and related optical transitions [141].

Walsh et al. [3] showed that the stronger onset at 3.7 eV relates to the first allowed transition from valence band states of (T_u) Γ_8 symmetry, which is located 0.81 eV below VBM, to CBM (A_g) Γ_1 symmetry. They attributed the weaker onset at around 2.9 eV to the forbidden transitions from VBM to CBM, as depicted in Fig. 6.5 [3].

The magnitude of the lowest gap and also the location of the VBM are still controversial. Bechstedt et al. [169] ascribed the onset of the optical absorption at lower energy to the transitions from lower occupied states of the CB to the higher ones.

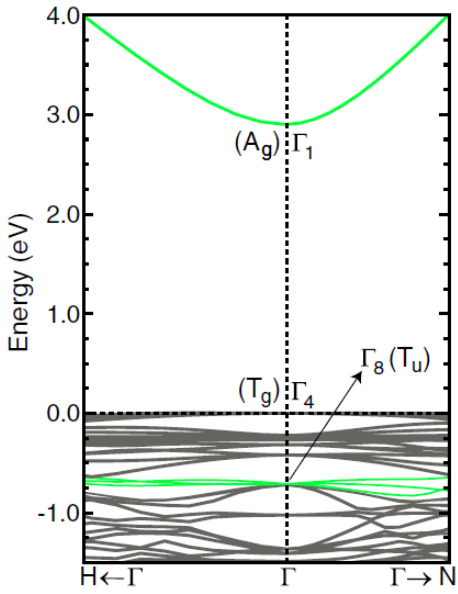

Figure 6.5: Calculated band structure of In_2O_3. The bands which originate the optical transitions at the Γ point are represented by green thick lines [3].

6.4 ARPES measurements of the electronic properties of the melt-grown In_2O_3 bulk single crystals

In order to study the band structure of the melt-grown In_2O_3 (111) bulk single crystals, high-resolution ARPES has been performed at the BEST beamline at the synchrotron-radiation laboratory BESSY II. The (111)-oriented samples of 3×3×0.5 mm^3 were prepared from a bulk crystal of over one inch in diameter. Next the samples were cleaved parallel to the (111) planes in UHV prior to photoemission study. The samples were oriented with one of the azimuth-symmetry directions of Γ-N. Photons in the energy range of 5-40 eV were used [154]. Energy and angle resolution of 20 meV and 0.2°, respectively, were found to be sufficient to resolve all essential details. The ARPES measurements were done at room temperature.

Normal emission photoelectron spectra (polar emission angle θ=0) were measured at the photon energy of 17 eV to 25 eV to study the valence band of the sample perpendicular to the (111) cleavage surface, along the Γ-P direction of the Brillouin zone. Fig. 6.6 exhibits the EDC series of the spectra at different photon energies.

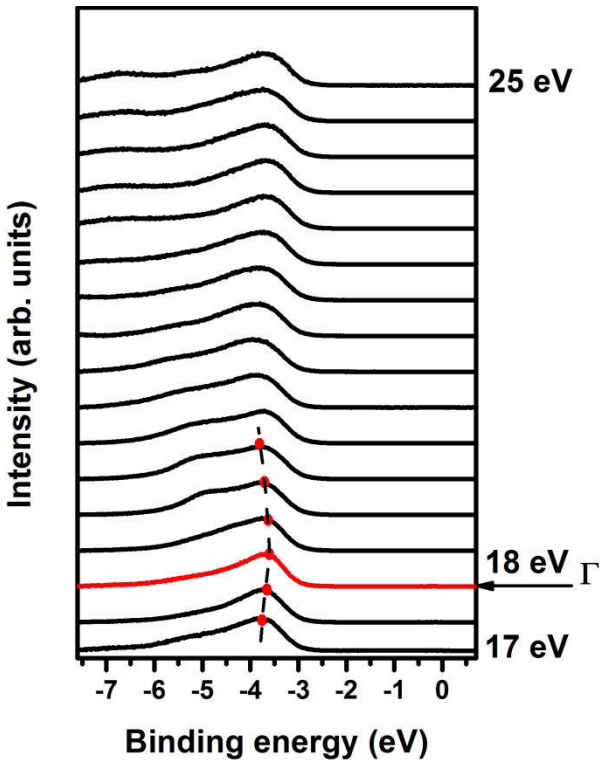

Figure 6.6: The EDC series of the melt-grown In_2O_3 (111) surface at different photon energies which probe the momentum perpendicular to (111) plane, along Γ-P direction of the BZ.

A shift of the spectral features to lower binding energies (upward dispersion) is identified in this figure. The minimum binding energy of the bands occurs at excitation energy of 18 eV. In fact, the bands disperse symmetrically with respect to this energy showing the correspondence of that with the Γ-point of the BZ and inner potential V_0 of the 13.1 eV. Likewise, Scherer et al. found that the photon energy of 18 eV probes the Γ-point of the third Brillouin zone of In_2O_3 with respect to the momentum perpendicular to the (111) surface [5].

The critical carrier density n_c for the onset of the degeneracy in In_2O_3 is 1.8×10^{18} cm^{-3} [8]. Therefore, the crystals which are the subject of this study with electron concentration around 2×10^{17} cm^{-3} are none-degenerate. As expected for a none-degenerate semiconductor, no emission can be observed within the band gap, as shown in Figure 6.7.

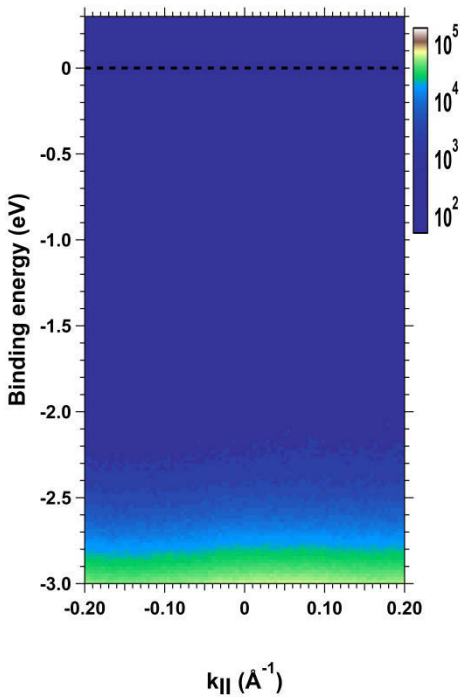

Figure 6.7: ARPES map of the melt-grown In_2O_3 (111) surface near the Fermi energy along Γ-N direction, taken at photon energy of 18 eV.

Figures 6.8 and 6.9 demonstrate examples of the fitting results of the main peak of VB and the upper part of the VB region, respectively. These spectra were recorded at photon energy of 18 eV. The main peak consists of three VB states at binding energy of -3.64, -4.05 and -4.70 eV. According to the Fig. 6.5, VBM is located at binding energy of around -2.80 eV.

In order to determine the band gap, the energy of the bottom of the conduction band should be determined. The CBM position can be derived using following formula and considering In_2O_3 as a direct band gap material as discussed in previous chapter.

$$(E_C - E_F) = k_B T \, ln \, (\frac{N_C}{n}) \tag{6.1}$$

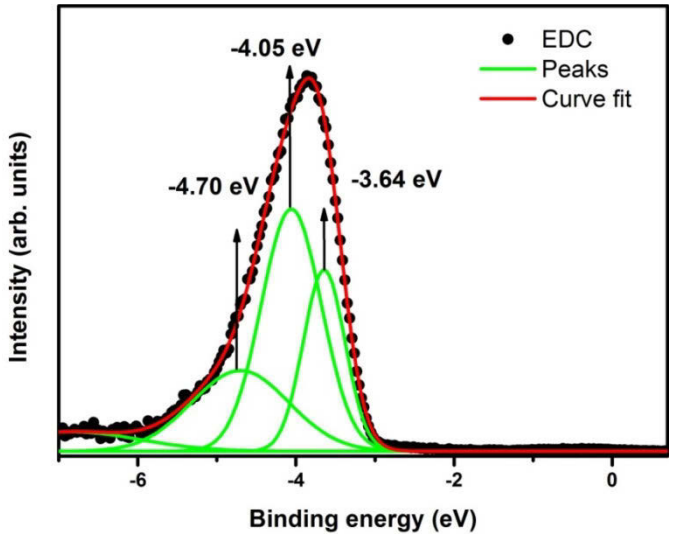

Figure 6.8: ARPES spectrum of the valence band at excitation energy of 18 eV. The fitting result of the main peak of the VB is also included.

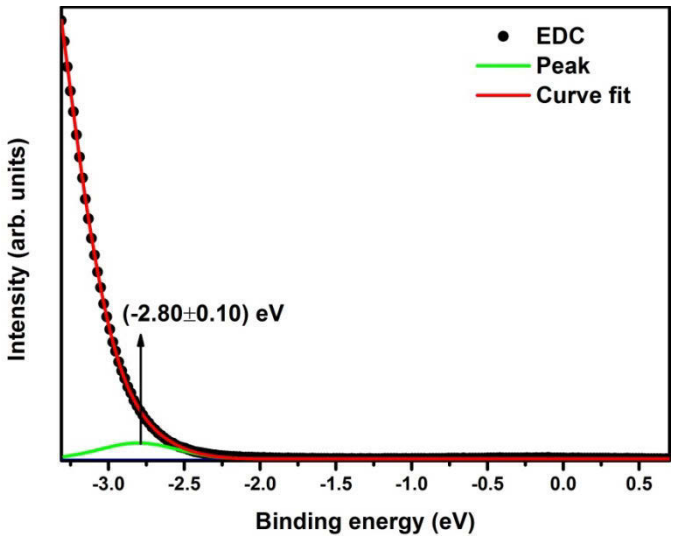

Figure 6.9: The upper region of the VB of In_2O_3 taken at photon energy of 18 eV. The top most of the valence band is detected to be at binding energy of -2.80 eV.

here K_B is Boltzmann's constant, T the absolute temperature, n the carrier concentration, and N_C the effective density of states of the conduction band ($N_C=2(2\pi\, m_e{}^*K_BT/h^2)^{3/2}$, with Planck's constant h and the electron effective mass in conduction band $m_e{}^*$). With the carrier concentration of the present In_2O_3 single-crystals of $n=2\times10^{17}$ cm^{-3} at room

temperature and employing $m_e^* \approx 0.24\ m_0$ along the Γ-N and $m_e^* \approx 0.18\ m_0$ along the Γ-P direction of the Brillouin zone [5] the energy difference E_C-E_F =0.069±0.010 eV. Therefore, the energy difference between topmost of the VB and bottom of the CB results in Eg_1=(2.87±0.11) eV, which is in good agreement with the fundamental band gap obtained from the optical measurements, see section 4.2.2, and previous reported values for the forbidden-dipole transitions at lower energies [3, 5, 70, 109, 166-168]. Transitions from the states around 0.8 eV deeper than VBM (E_B=-3.64 eV) to CBM leads to Eg_2=(3.71±0.11) eV consistent with ab initio calculations [3]. In addition to the accordance of these results with earlier studies [3, 5, 10, 70, 108, 109, 133, 166-169], they reveal that the bands at the surface of the studied crystals are nearly flat.

By varying the emission angle θ at the fixed photon energy of 18 eV, the band structure of valence band measured along the Γ-N high-symmetry direction. The corresponding EDC spectra are shown in panel (a) and (b) of figures 6.10. As expected for In_2O_3 with its large unit cell, it is not possible to resolve the individual electronic bands and compared their energy to the calculated band structure. In accordance to the theoretical calculations, one can see a roughly flat valence bands in this figure.

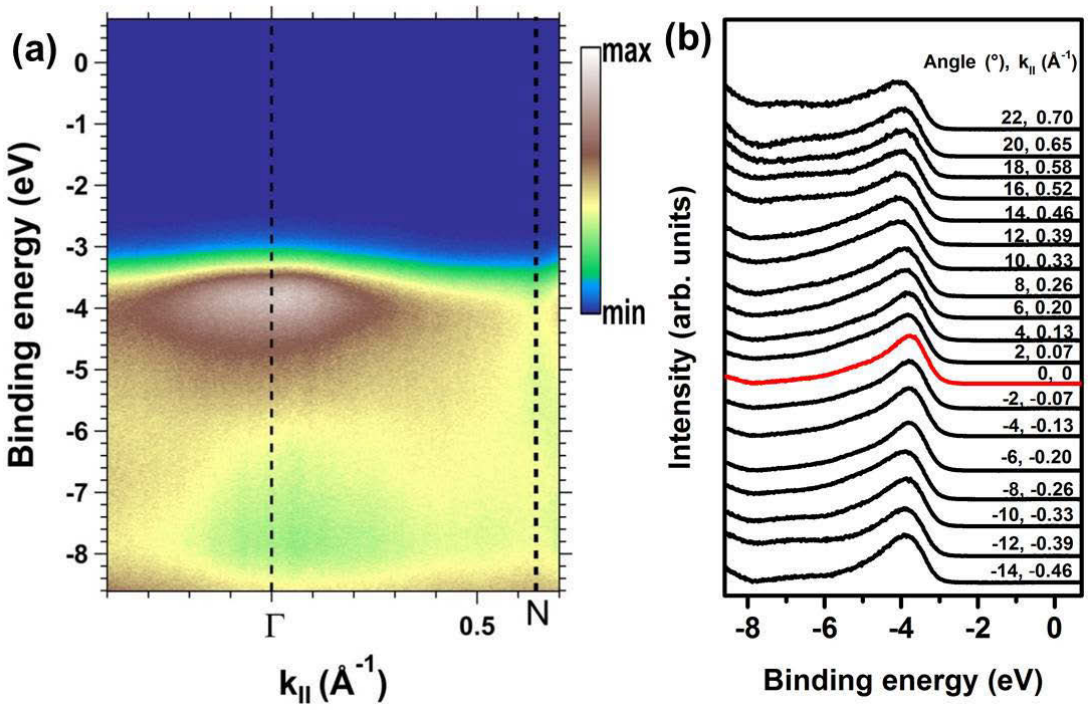

Figure 6.10: (a) The valence band structure along the Γ-N direction of the BZ of melt-grown In_2O_3. (b) The corresponding EDC spectra along Γ-N taken at different emission angles.

6.5 Surface electron accumulation layer

Due to the presence of the surface and in some cases also existence of defect or impurities the bulk translational symmetry in the perpendicular direction is broken. Thus, the surface electronic structure may differ from the bulk one and surface states may form, leading to a rearrangement of the carrier density and the variation of surface concentration in comparison to the bulk. In semiconductors, presence of surface states causes the pinning of the Fermi level within their band gap and resulting in bending of the bands relative to the Fermi level.

For example, by photoemission spectroscopy King et al. found that the surface Fermi level located 3.4 eV above the VBM, while from IR reflectivity and Hall effect measurement, it was identified it lies 2.95 eV above the VBM in the bulk of MBE-grown single crystalline In_2O_3 (001) thin films [7], see Fig. 6.11. Their results demonstrate the existence of a pronounced downward band bending at the surface of this material [7]. The high n-type conductivity and also the identification of SEAL in In_2O_3 are attributed to the placement of charge neutrality level (CNL) above the CBM [7]. Low-lying CBM could be as a result of the large size and electronegativity mismatch of the cation and the anion [35]. The presence of SEAL was also observed at (111) and (0001) surfaces of bixbyite and rhombohedral In_2O_3 thin films, respectively [9]. Therefore, these results indicate that there is a downward band bending and an increase of the electron concentration at the surface, i.e. a surface electron accumulation layer. A number of recent publications ascribed the onset at low energy to the existence of pronounced downward band bending and consequently to the SEAL in In_2O_3 thin films [8, 9].

The existence of the SEAL has also been reported for other TCOs like ZnO [170], SnO_2, [171, 172], In based III-V compounds like InAs [173] and InN [174], and the post-transition metal oxide CdO [174]. Moreover, Zhang et al. [8] demonstrated the presence of a two dimensional electron gas (2DEG) in In_2O_3 with high enough electron density to have many-body interactions shrinks the band gap and causes electron accumulation at the surface, as shown in figure 6.12. Using the measured Fermi momenta the surface charge density was estimated to be 4.2×10^{13} cm^{-2}. By fitting with a parabola the effective mass of the free-electron like state was obtained to be 0.22 m_0 [8].

Similarly, a 2DEG was also identified at the $LaAlO_3/SrTiO_3$ interface and later in $SrTiO_3$ [30, 176]. According to the previous studies, the microscopic source of 2DEG and SEAL in In_2O_3 and likely in $LaAlO_3/SrTiO_3$ interfaces are oxygen vacancies at the surface [8, 11, 177-179].

Furthermore, 2DEG and SEAL for In_2O_3 have been observed only for epitaxial thin films or crystal surfaces prepared prior to investigations, e.g. by sputtering and annealing.

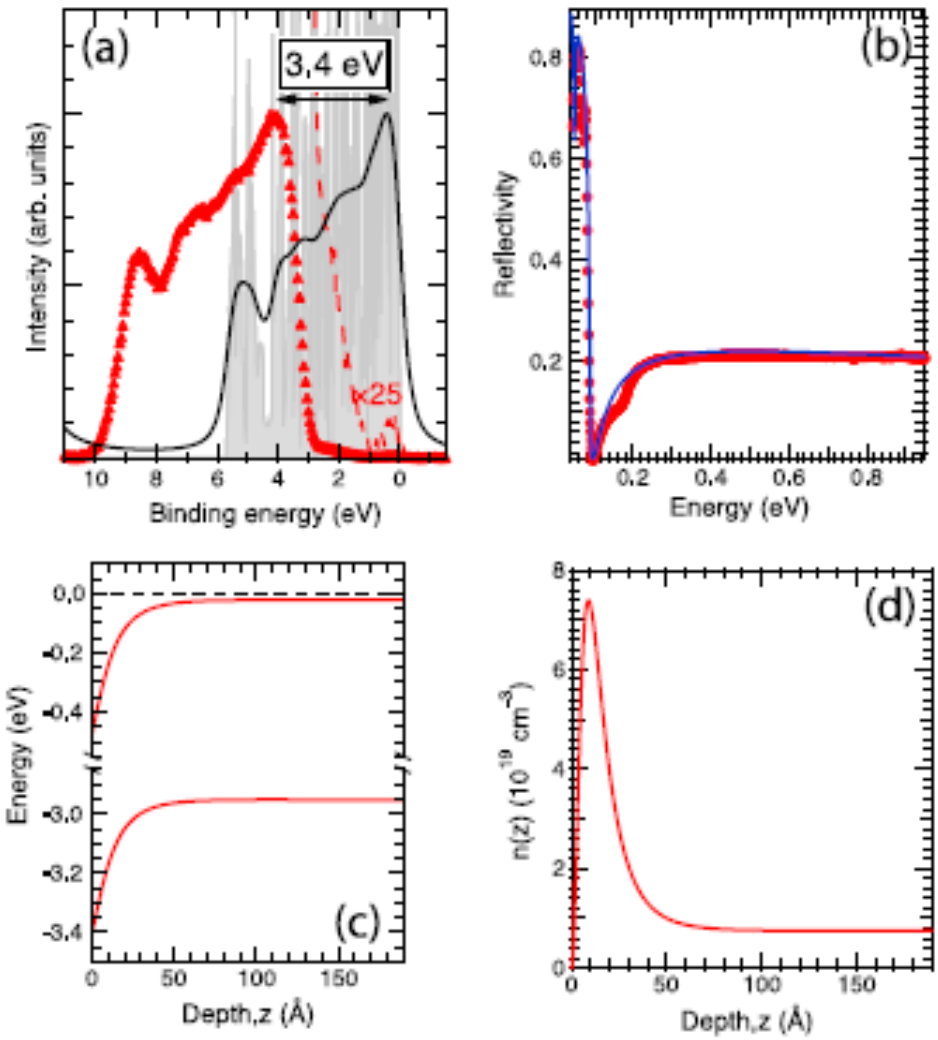

Figure 6.11: a) PES and also DFT-calculated spectra of the valence band of In_2O_3 showing that the surface Fermi level is pinned 3.4 eV above the VBM. (b) Measured and simulated IR-reflectivity denoted by circles and line, respectively, displaying the Fermi level lies very close to CBM. (c) Downward band bending. (d) An increase of electron concentration at the surface in comparison to the bulk concentration, calculated using Poisson's equations. Adopted from [35].

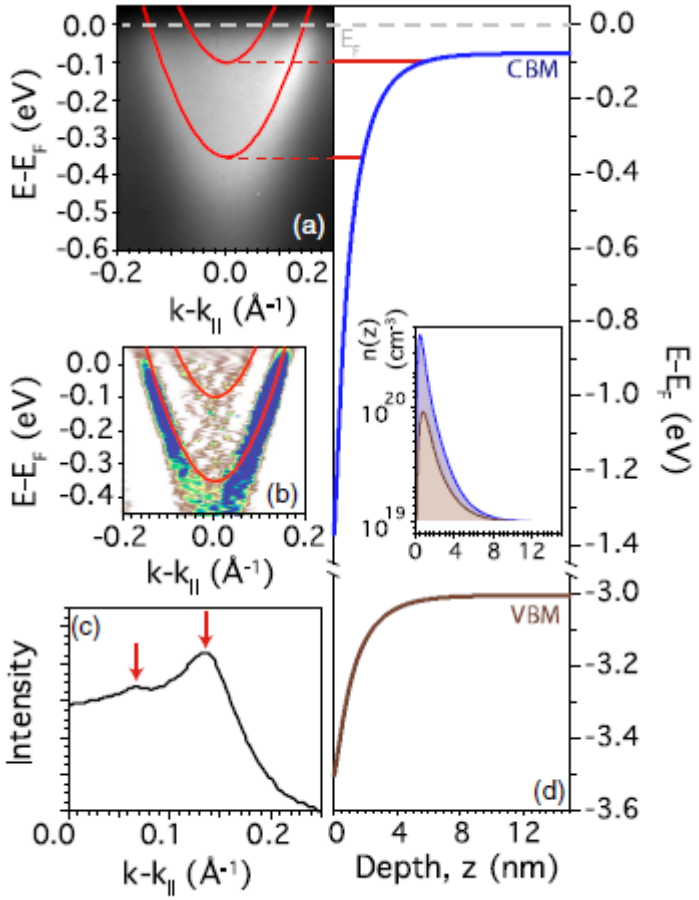

Figure 6.12: a) ARPES maps of In_2O_3 (111) thin films near the Fermi energy along the $[1\bar{1}0]$ direction taken at photon energy 9 eV, revealing the presence of two nested subbands below the Fermi level, the position of the subbands was determined by Poisson-Schrödinger calculations and shown by solid curves. (b) Second-derivative image of the data in panel (a). (c) Momentum distribution curve derived by summing the intensities over an energy range of ±25 meV. The Fermi wave vectors of the subbands are displayed by arrows. (d) Downward band bending of 1.30 V in the VB and 0.45 eV in the CB. The inset displays the derived near-surface carrier density from Poisson calculations within a modified Thomas-Fermi approximation (MTFA). From [8].

However, Scherer et al. [5] reported distinct dispersions of electronic bands perpendicular to the surface, in contrast to the SEAL case, on UHV-cleaved CVT-grown In_2O_3(111) single crystals, as shown in Fig. 6.13. As discussed in the previous section, the fundamental and surface band gaps are roughly similar in the crystals which are the subject of this study, which implies that the surface of these samples is free of the

accumulation layer. The existence of SEAL is still under discussion in as-cleaved In_2O_3 bulk single crystals. Employing hard X-ray photoemission spectroscopy (HAXPES) at 6000 eV and x-ray photoelectron spectroscopy (XPS) on thin films of In_2O_3, Körber et al. [14] claimed a carrier accumulation at In_2O_3 surfaces being related to the particular sample preparation or processing, i.e. not an intrinsic property of the material. Our data confirm this hypothesis.

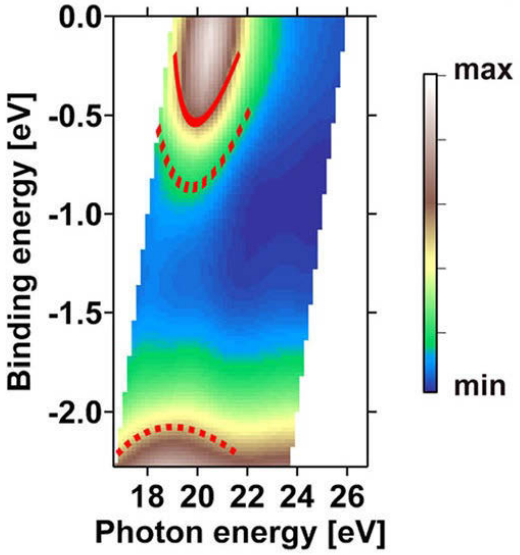

Figure 6.13: a) ARPES photocurrent map of CVT-grown In_2O_3 (111) bulk single crystals near E_F recorded at normal emission with different photon energies, revealing the dispersion of the conduction band in $k_\perp$, Γ-P direction, the flank of the CB and the uppermost VB are shown by red-dashed curves. From [5].

Chapter 7
Metal-In_2O_3 contacts

7.1 Introduction

The extraordinary properties of semiconductors allow us to manipulate their conductivity by external stimulation using electrical currents, electromagnetic fields and/or light. Application of semiconductors in electronic devices necessitates electrical contacts. As the contacts are metallic, the understanding of the metal-semiconductor (M-S) interface, which is in fact an intimate contact between these two materials, is essential to improve the performance of existing devices and to build new ones. A rectifying metal-semiconductor interface was the first semiconductor devices, which was discovered by Braun in 1874 [180]. He pointed out that the current flowed freely in just one direction at the point-contact between a metal and a metal sulfides. Braun described this behavior in terms of extremely high resistive thin surface layer at the interface [181]. In 1938, Schottky attributed the rectifying behavior at the M-S interface to the presence of potential barrier resulting from a depletion layer on the semiconductor side of the junction [182]. Schottky proposed a model to predict the barrier height, nowadays called the Schottky-Mott rule, according to which the barrier height is given by the difference between the electron affinity of the semiconductor and the metal work function [183].

In several systems, a discrepancy is usually observed between prediction of this model and experimentally-derived barrier heights. In 1974 Bardeen [184] noted that a high density of states at the interface, originating, for example, from surface states or metal-induced gap states (MIGS), lead to the Fermi level pinning which can cause this disagreement.

The barrier height is commonly determined by current-voltage (I-V) and capacitance-voltage (C-V) measurements. In the present work, ARPES was applied to derive the barrier height of the metal-In_2O_3. The advantage of this direct and surface-sensitive technique with respect to the afore-mentioned ones is that it allows us to study the electronic structure of the interface during the contact formation in addition to the determination of the barrier-height.

TCOs with their widespread applications are of particular interest to study M-S junction, as most of the electronic devices rely on ohmic or Schottky contacts. n-type In_2O_3 is even more interesting to investigate due to the presence of SEAL, which is commonly believed prevents Schottky-contact formation in In_2O_3 thin films. Although this characteristic is favorable for ohmic contact creation, it hinders space-charge based characterization techniques as well as function of this material as Schottky diodes or field-effect transistors. To reduce the influence of the SEAL, surface preparations of In_2O_3 thin films by oxygen-plasma treatment [10] and reactive-sputtering process in an O_2-Ar atmosphere [15] were reported. In the previous chapter, we stated that transmission and ARPES measurements showed that as-cleaved melt-grown crystals have nearly surface flat-bands. Therefore, their clean surface should be free from electron-accumulation layers, and accordingly it is expected that a rectifying contact can form on its surface. In this chapter, the results of metals (Cu, Ag, Au, In, and Sn) on In_2O_3 will be presented and then compared with the Schottky-Mott rule and MIGS-based model.

7.2 Basic characteristics of the metal-semiconductor contacts and Schottky-Mott rule

Schottky described that the rectifying behavior of the M-S junction is generated by space-charge region on the semiconductor side of the interface. In this model, it is assumed that the semiconductor does not have any surface states within the band gap, and its bands are flat. The energy-band diagram of a M-S junction is schematically represented in Fig. 7.1. The work function of the metal and semiconductor, which are the energy difference between their Fermi level and the vacuum level, are denoted by

Φ_M and Φ_S, respectively. The electron affinity of semiconductor χ is the energy difference of its conduction band edge and vacuum level. According to the Schottky model, when a metal and semiconductor with different work functions are brought into the contact, an electric field is produced as a result of their work function difference and matching of the Fermi level. The penetration of the electric field in the metal can be neglected, as its penetration depth, which is determined by Thomas-Fermi screening length $L_{Th\text{-}F}$ is generally less than 1 Å ($L_{Th-F} = [\left(\frac{e^2}{\varepsilon_0}\right) D_m(W_F)]^{\frac{1}{2}}$, where e, D_m (W_F) and ε_0 are respectively elementary charge, the number of states per unit energy and unit volume at the Fermi level and vacuum permittivity). On the other hand, the electric-field penetration, the Debye length L_D, is around 13.4 nm for a typical semiconductor with concentration of order 10^{17} cm^{-3} and at room temperature ($L_D = \left(\frac{\varepsilon_b \varepsilon_0 k_B T}{e^2 (n_b + p_b)}\right)^{\frac{1}{2}}$, in this expression ε_b, n_b and p_b are static dielectric constant, bulk electron and hole concentration of the semiconductor, and k_B and T are Boltzmann constant and absolute temperature, respectively) [182].

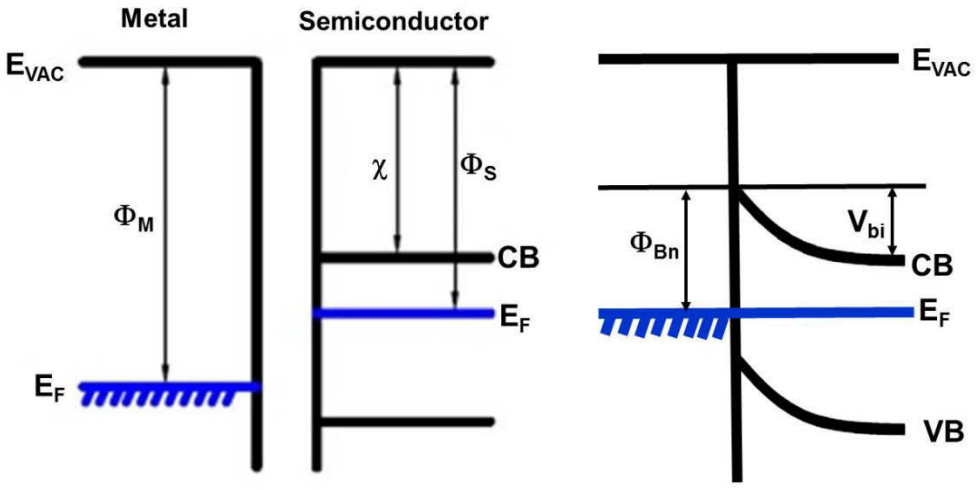

Figure 7.1: Energy band diagram of a metal in contact with a n-type semiconductor before the contact (left) and after the contact (right). From [183].

Therefore, the electric field enters deeply into the semiconductor. The work function of the semiconductor increases as the electric field penetrates it, and accordingly, the potential lowers by V_{bi} [182].

Assuming an abrupt contact, for an ideal metal-n-type semiconductor, the Schottky barrier height (SBH) is simply given by [182]:

$$\Phi_{Bn} = \Phi_M - \chi \quad (7.1)$$

In fact, for a n-type semiconductor the barrier height is the distance between the bottom of the semiconductor's conduction band and the metal Fermi level. For the ideal metal-p-type semiconductor contact, the barrier height Φ_{Bp}, which is the energy difference of the valence band edge of the semiconductor and the metal Fermi level, is expressed by [183]:

$$\Phi_{Bp} = E_g - (\Phi_M - \chi) \quad (7.2)$$

where Φ_M and χ are the same as above and E_g is the band gap of the p-type semiconductor, and the Schottky barrier height is the energy difference between VBM of the semiconductor and the metal Fermi level. The built-in potential V_{bi}, which the electrons feel during their movement into the metal, is determined by:

$$V_{bi} = \Phi_{Bn} - V_n \quad (7.3)$$

here V_n is energy difference between the Fermi level and the CBM.

When a metal and a semiconductor are in electric contact, an inversion (depletion) layer forms at the junction as a result of the charge transfer across the interface and diffusion of the carriers away from the junction. A depletion layer is free of mobile carriers and acting as a potential barrier which prevents flow of electrons (holes) from metal (p-type semiconductor) to the n-type semiconductor (metal).

According to the Schottky-Mott rule, three types of contacts can form depending on the difference between work function of the metal and the semiconductor. These contacts are named accumulation, neutral and depletion, as the majority of carriers are accumulated, unchanged or depleted at the interface. Figure 7.2 represents these three different metal-n-type semiconductor interfaces [135] before the contact at upper part and after the contact at lower part. Accumulation and neutral contacts ($\Phi_M \leq \Phi_S$) are non-rectifying, i.e. ohmic, while the depletion one ($\Phi_M > \Phi_S$) is rectifying, i.e. Schottky. In the ohmic contact cases, the contact has negligible resistance, and electrons can therefore flow easily between the two materials. Stable ohmic contacts are critical for the performance of the semiconductor devices, such as field-effect transistors, metal-oxide-semiconductor field effect transistors (MOSFET), and LEDs.

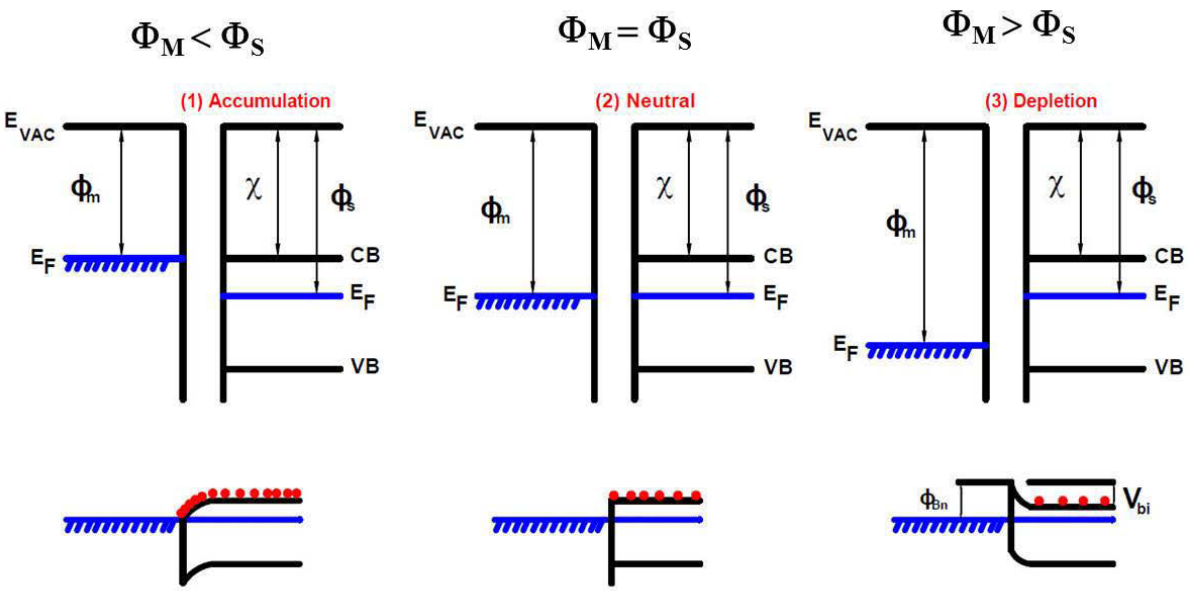

Figure 7.2: Schematic representation of the band diagram of three possible metal-n-type semiconductor contacts according to the Schottky-Mott rule. Upper part displays the metal and the semiconductor energy-band diagram before the contact, and lower part show them after the contact. From [135].

The experimental barrier heights are not usually consistent with the prediction of the Schottky-Mott rule, and they do not usually depend on the metal work function. For instance, the disagreement of the Schottky-Mott rule prediction and the experimental data for the metal-n-type Si Schottky contacts is clear in the Fig. 7.3 [185].

However, this figure shows that there is a correlation between the SBH and the measured barrier heights on n-type Si. In this model, the possible chemical reaction and the effect of the atomic structure at the interface, i.e. any interface interactions are not regarded. Bardeen [182] proposed that the charged surface and interface states, which are accompanied by a double layer of charge lead to the Fermi level pinning.

The absorption of the charges coming from the metal into the semiconductor by these states shielding the semiconductor from the details of the metal. Therefore, the bands line up with respect to these charged surface and interface states [184].

In the next section, this phenomenon and the metal-induced gap states model will be discussed.

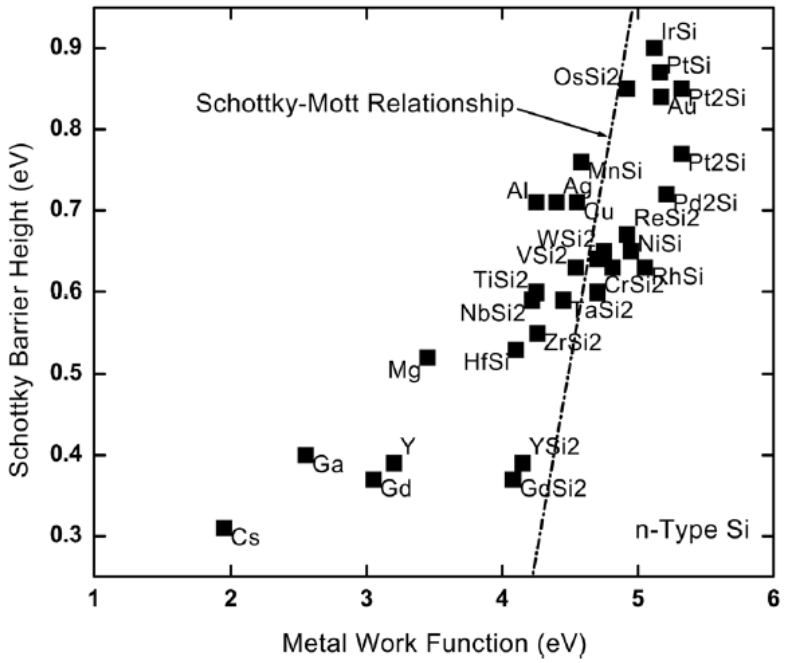

Figure 7.3: The experimentally measured barrier heights on n-type Si and the discrepancy existed between experimental results and predicted one from Schottky-Mott rule (straight line). From [185].

7.3 MIGS-based concept

As mentioned in forgoing section, Bardeen noted that the interface states are present within the band gap of semiconductor at Schottky junctions. As a result of the charge neutrality, the net charge in the metal side is equal to the sum of the net charge of the interface states and space-charge region on the semiconductor side in the equilibrium. The physical origin of these states is generally interpreted as follows:

In the bulk crystal of a semiconductor, it is usually assumed that the potential has the periodicity of the lattice. The end of the semiconductor material with the surface or interface states result in the breaking down the periodicity and the change of the wave functions of the electrons. The deviation of the periodicity can be as a result of either intrinsic surface and interface states or extrinsic ones (such as bulk defect of the semiconductor) [186].

At the M-S interfaces, the wave functions of an electron in the semiconductor should match with that of the metal. Heine [187] noted that the metal wave functions tail

extends into the semiconductor because of the overlap between the metallic band and the band gap of the semiconductor, as shown schematically in Fig. 7.4.

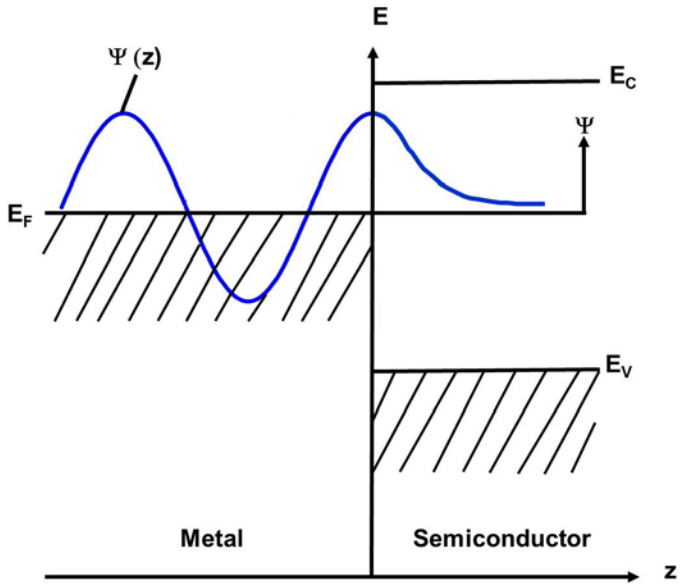

Figure 7.4: Representation of the metal Bloch state Ψ (z) near the Fermi level which decays into the semiconductor. Adopted from [188].

The deviation from perfect periodicity at the contact leads to the formation of exponentially decaying interface states with imaginary wave vectors [188]. Schrödinger's equation results in the creation of these virtual gap states (VIGS) within the forbidden gap of the semiconductor. Louie and Cohen reported that there are four different types of interface states by model calculation for jellium-silicon interface [182]. Their result is schematically depicted in Figure 7.5.

The first states are bulk-like ones, which exist on both sides of the barrier.

The second ones are bulk-like semiconductor states entering into the metal, which are located lower than CB of the metal.

Third, localized-interface states placing in the deeper band gaps of the semiconductor.

Fourth, the metal-induced gap states lie in the range of the energy that CB of the metal overlaps the band gap of the semiconductor. The wave functions of the fourth type states are bulk-like in the metal decaying rapidly into the semiconductor [182].

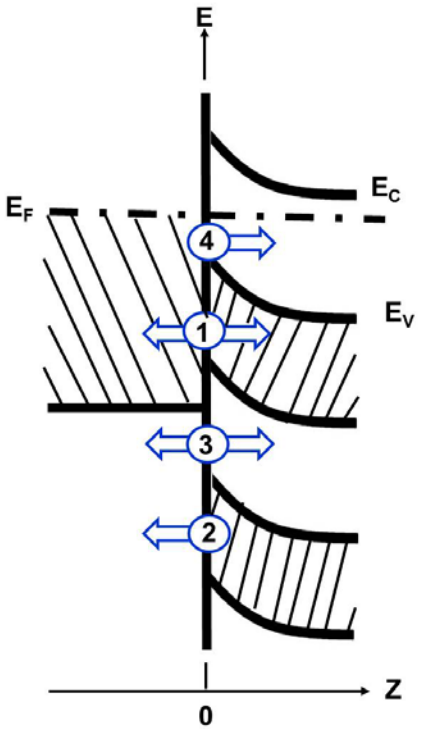

Figure 7.5: Schematic representation of the four types of the electronic interface states, derived by model calculations for a jellium-Si interface, bulk-like states (1), decaying semiconductor states into the metal (2), localized states (3) and MIGSs (4). From [182].

The results of these realistic, atomic calculations are in very good agreement with Heine description for the penetration of the metal-Bloch states into the VIGS when band gap of semiconductor overlaps CB of the metal [188].

The character of the virtual gap states relates to their position within the band gap. As they lie closer to the bottom of the conduction band their acceptor-like character increases, while they mostly show donor-like behavior near the maximum of the valence band. The energy point within the band gap, in which the contribution of both acceptor and donor-like states is equal, is called branch-point energy E_{bp} of the complex band structure or CNL [186]. If the Femi level is located above the CNL the charge density of MIGS is negative, whereas it is positive for the Fermi level lying below it [182]. The charge densities of metal or semiconductor are situated on both sides of the interface, and revealing a charge transfer between these two materials. The charge density is the sum of the space-charge density Q_{sc} and the charge density of the interface states Q_{is} (total charge per unit surface in the junction). Pauling proposed that there is a correlation between the ionicities of covalent single-bond in diatomic molecules and the difference

of their atomic electronegativities. Using this concept, Mönch demonstrated that charge transfer in the M-S junction corresponds to the difference between the electronegativities of the metal and the semiconductor substrate X_m-X_{sub} [182]. When there is no charge exchange between these two solids, i.e. X_m-X_{sub} =0, the Fermi level therefore coincides with the CNL. The charge neutrality level of the MIGS is in fact the branch-point energy of the virtual gap states. According to the MIGS-based and electronegativity concept, the barrier height is expressed by [182]

$$\Phi_{Bn} = \Phi_{cnl} + S_X(X_m - X_{sub}) \tag{7.4}$$

Where Φ_{cnl} (Φ^n_{bp}=E_C-E_{bp}), and S_X ($\partial\Phi_{Bn}/\partial X_m$) are the charge neutrality level (n-type branch-point energy) and the slope parameter, respectively. The equation (7.4) also shows the important role of the CNL in the barrier determination. The electronegativities of the metal and semiconductor in Miedema unit [189] are used in this equation. Miedemas' electronegativities X_{Mied} relate to the Paulings' ones X_{Paul} by X_{Mied}=1.93 X_{Paul}+0.87 [182]. The reason for the preference of Miedema values to Pauling ones is that the electronegativities were obtained from the metals and not from the constituents of diatomic molecules in this unit [186]. The slope parameter is given by

$$S_X = \frac{A_X}{(1 + 0.1(\varepsilon_\infty - 1)^2)} \tag{7.5}$$

where ε_∞ is the high-frequency dielectric constant and A_X=0.86 is a proportionality relating Φ_M and X_M in Miedema unit.

The underlying assumptions behind the gap-states based models result in an insignificant role of the metal work function as well as the structure of the interface in the barrier determination [185].

Although the models based on gap states can describe the Fermi-level pinning, various experimentally and theoretically-derived results are inconsistent with these models. For instance, it was found that the SBH rely on the atomic structure in metal-semiconductor contact with single crystalline interface [190, 191], which was also approved by theoretical calculations [192-195]. Thus, the SBH is associated with the chemical bonds and detail of the atomic structure at the interface. In addition, the bias voltage and work function dependence of the barrier height is in contrast to the underlying assumption of these models, which assumes that the distribution of gap states essentially depends on the semiconductor [185]. The mechanism of the formation of the SBH is very complex

with many phenomena contributing and competing with each other. It cannot be therefore ascribed to a single simple general rule. For a more comprehensive and detailed discussion on the SBH, the reader may refer to the Ref. [195].

7.4 The surface photovoltage effect

The surface photovoltage effect (SPV) for the first time was explained by Bardeen and Brattain, when they studied the photon-induced variation of the potential with a mechanically vibrating reed on Ge [196, 197]. When the surface of a semiconductor is irradiated by light, electron-hole (e-h) pairs are generated via band-to-band transitions or releasing captured carriers through trap-to-band transitions. The number of pairs is higher at the surface than in the bulk. For the high-quality materials, trap-to-band transitions are negligible. The photon-induced electron-hole pairs move in opposite directions as a result of the potential in the space-charge layer. A similar phenomenon happens at the Schottky M-S contact, when it is exposed to light during the ARPES measurement. If the photon beam impacts on a rectifying interface, e-h pairs will be created and followed by spatial redistribution inside the sample because of the electric field. For example, in a rectifying metal-n-type semiconductor contact, electrons are forced to move towards the bulk of the semiconductor due to the presence of the potential difference (Φ_{Bn}), whereas the holes are trapped at the surface to compensate space-charge region.

The occurrence of SPV therefore causes the shift of the PE spectra to the higher binding energies for the n-type semiconductors and lower energies for the p-type ones, i.e. the reduction of the barrier height [198]. This effect is schematically presented in Fig. 7.6.

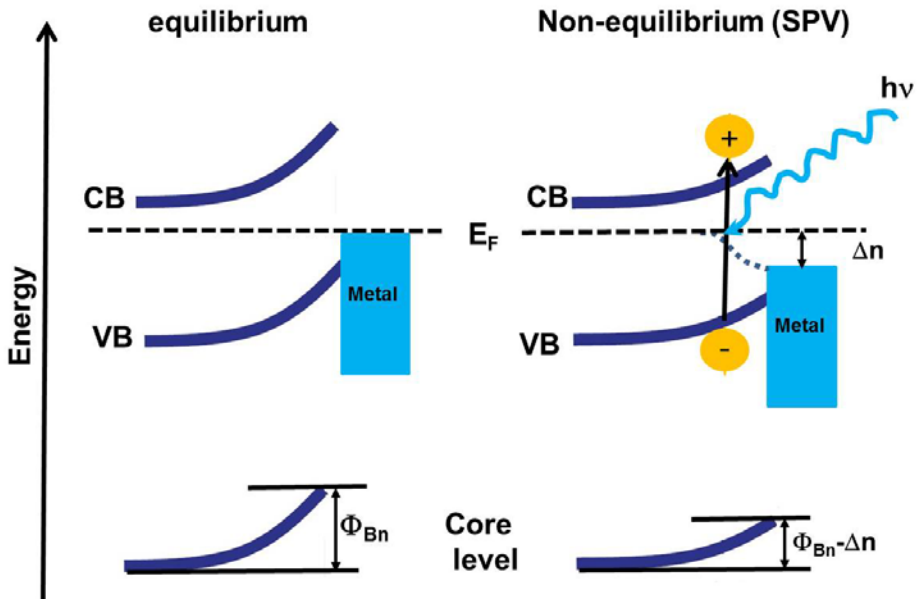

Figure 7.6: Schematic representation of the band alignment in equilibrium (left side) and in the presence of the SPV, leading to the shift of the band and reduction of the barrier height at metal-n-type semiconductor interface. Adopted from [198].

The surface photovoltage does not occur at ohmic contacts, at which the carriers flow easily and the recombination rate is too small to allow for the charge redistribution and an energy shift of the photoemission spectra. The shift of the spectra because of the SPV is generally determined by considering the shift of the well-developed Fermi edge of a thin metallic film covering the semiconductor relative to the reference Fermi energy of a thick metal layer [198, 199]. An excessively thick metal layer opposes the electrons, excited at the surface of the semiconductor crystal, from penetrating through the metal layer and hinders thus the measurement of the surface photovoltage effect. As a result, the Fermi level coincides with the reference Fermi energy. The magnitude of the SPV depends on different parameters, e.g. photon intensity, band bending, combination rate, bulk concentration [182], and temperature [200]. For example, it was found that its magnitude increases at lower temperatures [182]. The exponentially increase of the SPV with the increase of the size of the band gap [183, 201] makes it more important for the wide band-gap materials like In_2O_3.

To prevent the SPV induction by external light sources, the main chamber was darkened during the experiments in this study.

7.5 Work function determination by PES

In order to determine the barrier height from the Schottky-Mott rule, the work functions of metal and semiconductor, In_2O_3, are required. Photoemission spectroscopy offers the opportunity to measure the work functions of the metal and semiconductor precisely *in situ*. During the travel of electrons to the surface of the sample, most of the outgoing electrons undergo inelastic scattering, which reduces their kinetic energy. The electrons which experience inelastic collisions are called secondary electrons, and the ones which do not experience are primary electrons. Photoemission spectra are composed of these two contributions. The primary electrons reflect the density of states and appearing as the peaks in the spectra, whereas the secondary ones have continuous and featureless energy spectrum down to the zero kinetic energy. The primary electrons give information about the binding energies of the electronic states, and their kinetic energy is given by equation (5.2), Fig.7.7 (a). On the other hand, the slowest emitted electrons are secondary ones with zero kinetic energy, which are used to obtain the work function. As the analyzer and the sample are electrically in contact, there is a potential difference between the sample and the analyzer, given by the difference between their work functions ($\Delta\Phi=\Phi_m-\Phi_a$) and results from the equalization of their Fermi edges. Because of the potential difference and also considering this fact that usually $\Phi_m>\Phi_a$, the electrons will be accelerated during their travel through analyzer by $\Delta\Phi$. Accordingly, the spectrum is shifted by this value to higher kinetic energy, yielding $E_{kin}=h\nu-E_B-\Phi_a$ (Fig. 7.7 (b)).

Moreover, the secondary electrons are also generated by collisions of the electrons with the surface of the analyzer. Since these electrons are produced in the analyzer, they are not affected by the potential difference $\Delta\Phi$.

There is an overlap between the secondary edge of sample spectrum and an analyzer secondary edge. In order to separate these edges and remove the low-energy distortions of the analyzer electronic lenses, an accelerating potential E_{acc} is commonly applied. This leads to the acceleration of the secondary edge of the sample and not the edge of the analyzer, resulting in $E_{kin}=h\nu-E_B-\Phi_a+E_{acc}$ (Figure 7.7 (c)).

Due to the electrical contact between analyzer and the metallic sample, the kinetic energy scale of the sample is calibrated with respect to the Fermi edge of the sample by the Fermi energy of the metal. In fact, an ‘‘internal’’ kinetic energy scale is defined, implying that kinetic energy is given to the electrons before they escape from the sample. So, the kinetic energy of the fastest electrons in the vicinity of the Fermi edge is defined by E_{kin}^{max}=hν, and the whole spectrum shift subsequently. Accordingly, the secondary edge of the sample is shifted to the kinetic energy of the work function of the sample [202], as shown in Figure 7.7 (d). The secondary cut-off corresponds to the slowest electrons (E_{kin}^{min}), which had the minimum energy to overcome the work function. The work function for a metallic sample is given by:

$$\Phi = h\upsilon - (E_{kin}^{max} - E_{kin}^{min}) \quad (7.6)$$

here hν is the photon energy and E_{kin}^{max} and E_{kin}^{min} are the maximum and minimum kinetic energies of the photoelectrons measured in the spectrum. The minimum kinetic energy of the electrons E_{kin}^{min} is determined by a linear extrapolation of the low energy edge onto the abscissa. The maximum kinetic energy E_{kin}^{max} is the Fermi energy E_F. This value is obtained by fitting of a polycrystalline metallic film spectrum by the Fermi-Dirac distribution function and is used to calculate the work function of the sample.

The secondary cut-off electrons rarely consist of the electrons, which come from the Fermi edge. Therefore, E_{kin}^{min} can be determined by linear extrapolation of the low energy cut-off for the samples without any electronic features at the Fermi edge like semiconductors.

The lowest kinetic energy and the highest one of the initial spectrum of a semiconductor are zero and kinetic energy corresponding to the VBM, respectively.

By these values, one can determine just the ionization energy (E_{ion}). The E_{ion} is determined by:

$$E_{ion} = h\upsilon - (E_{kin}^{VBM} - E_{kin}^{min}) \quad (7.7)$$

Fig. 7.8 displays the schematic initial spectrum of a semiconductor (left side) and regarding to the internally-calibrated one (right side). The calibration and determination of the Fermi level of the analyzer by a metallic sample is a prerequisite to obtain the work function of a semiconductor.

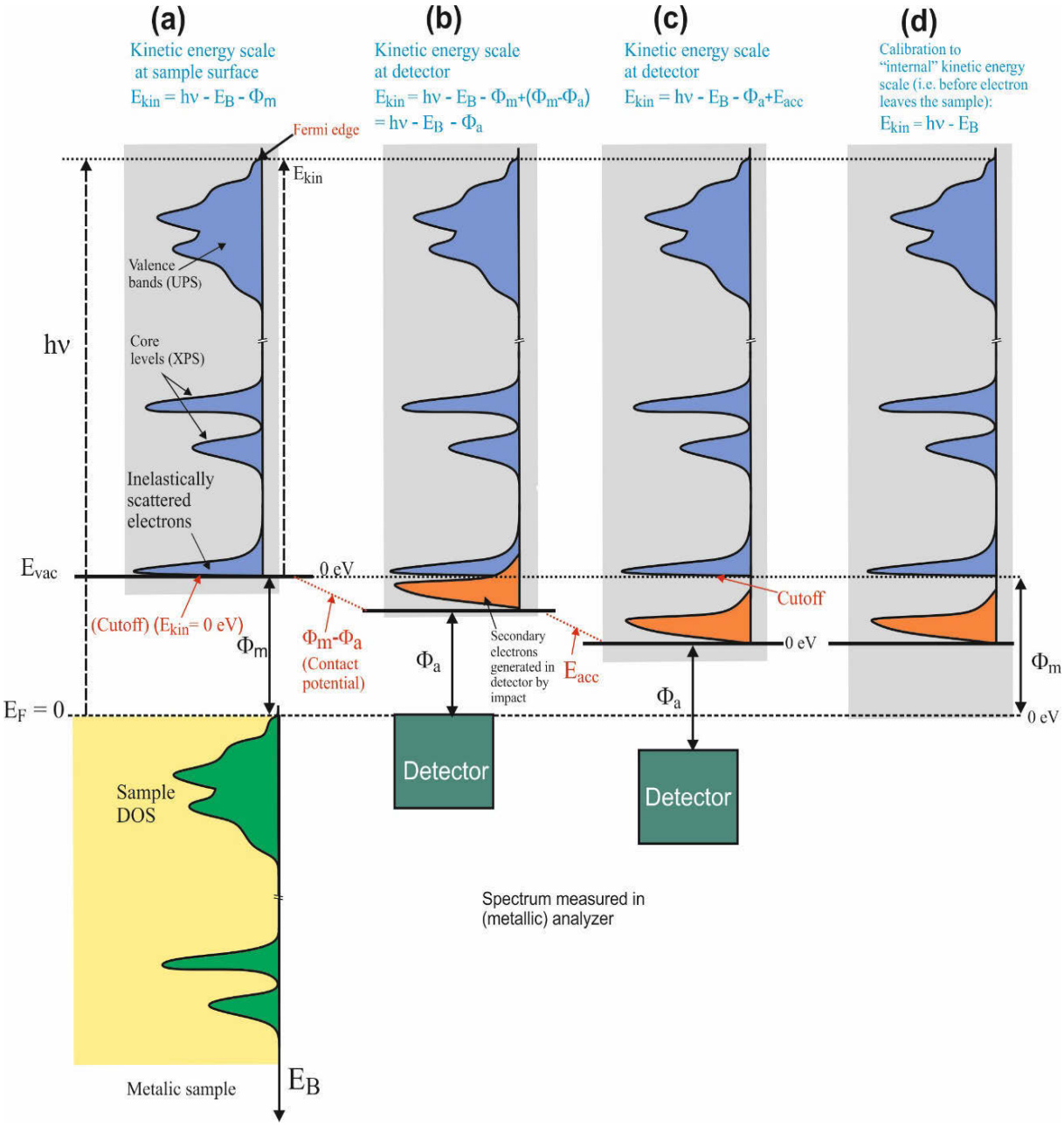

Figure 7.7: Schematic representation of the PES on metallic sample and the corresponding PES spectra. From [97].

Due to the fact that the semiconductor sample is electrically connected to the analyzer during the photoemission spectroscopy, the Fermi level of the semiconductor will be equilibrated with the analyzer. Thus, its ‘‘internal’’ kinetic energy spectrum will be calibrated, and the work function of the semiconductor and the semiconductor VBM energy can be determined [199]. In order to measure the work function of the In_2O_3 and the metals (noble metals, In and Sn), various biased voltage were applied in the range

between 1 to 7 V on the In_2O_3 and each metal. The bias voltage 7 V was found to be enough to stabilize the work function values for the In_2O_3 and the metals. The spectra were measured at the photon energy of 18 eV and at a bias voltage of 7 V. In Figures 7.9 (a) and (b) the high and low kinetic energy sides of the In_2O_3 overview spectra are displayed at RT and LT, respectively. Fig. 7.9 (c) shows the PE spectrum near the Fermi edge of a thick layer of the metallic Ag. The Ag spectrum was fitted by the Fermi-Dirac distribution function to determine E_{kin}^{max}, i.e. E_F. The minimum kinetic energy E_{kin}^{min} was obtained by linear extrapolation of their cut-off. Employing the derived values and applying the equation (7.6) for the work function determination yield Φ_{In2O3}= (4.25±0.05) eV at RT and Φ_{In2O3}= (4.30±0.05) eV at LT.

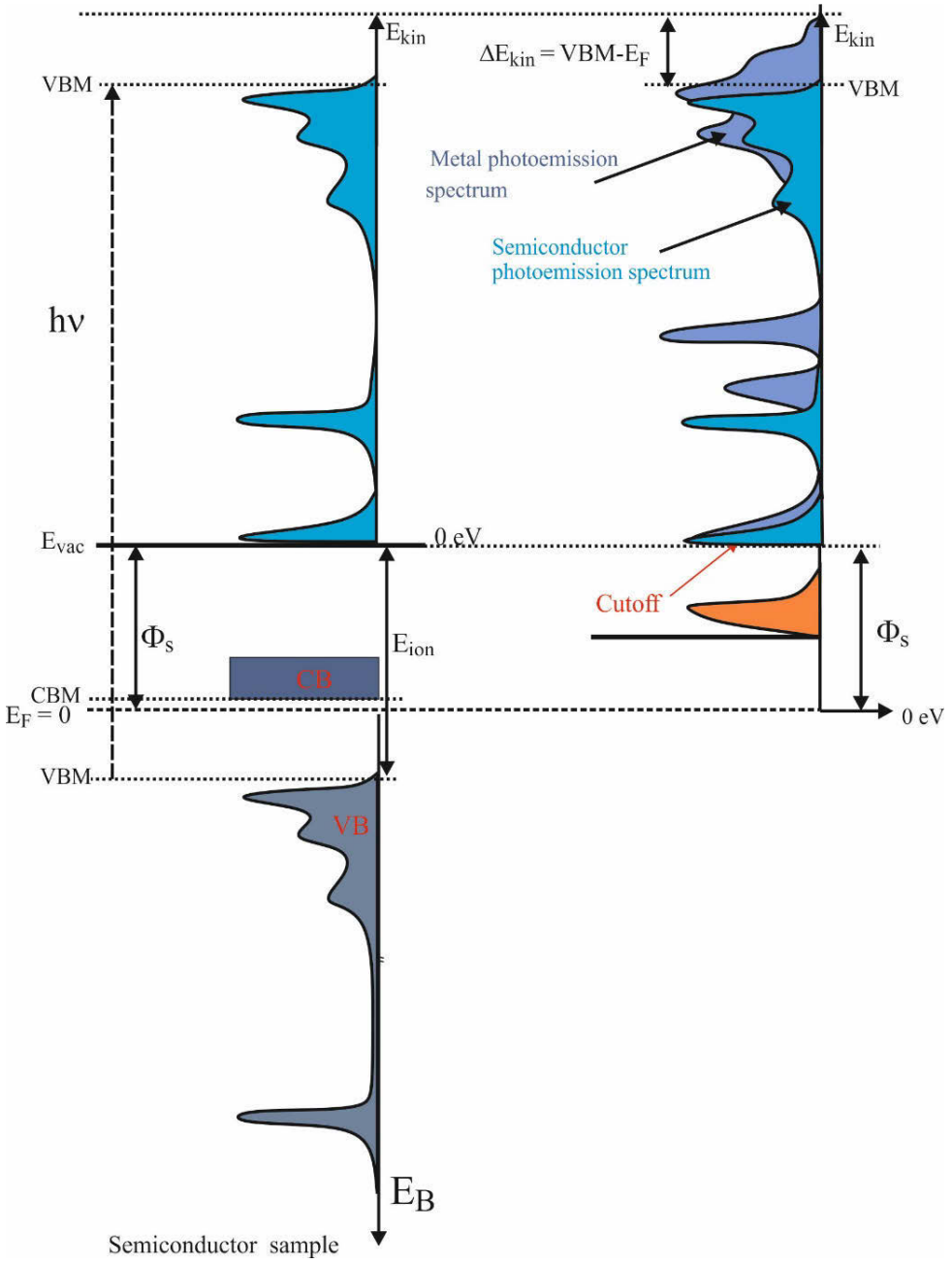

Figure 7.8: Energy scheme and the corresponding initial (left side) and ''internal'' kinetic energy calibrated spectra of a semiconductor (right side). Adopted from [97].

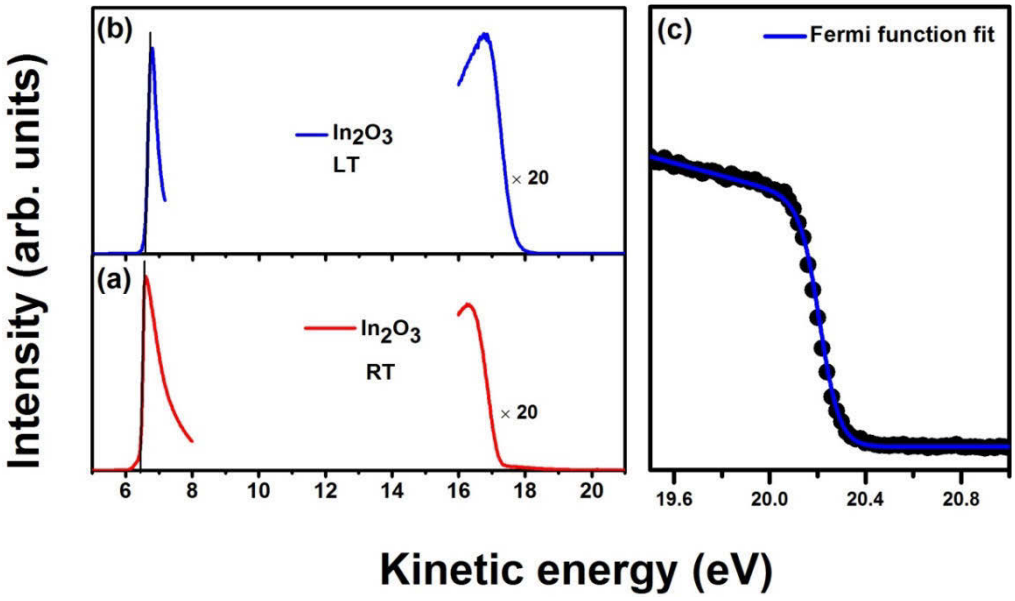

Figure 7.9: Low and high kinetic energy edges of the PE spectra of In_2O_3 taken at excitation energy of 18 eV and a bias voltage 7 V (a) at RT (b) LT. The minimum kinetic energy was determined by linear extrapolation of the low kinetic energy sides of the spectra. (c) Fermi function fit of the high kinetic energy edge of the thick Ag-layer (320s) to determine E_F.

The extraction of the metal work functions will be discussed in their corresponding sections.

To derive the barrier height from Schottky-Mott rule [183], the electron affinity of In_2O_3, the energy difference between the conduction band minimum E_C and the Fermi energy E_F, is needed:

$$\chi_{In_2O_3} = \Phi_{In_2O_3} - (E_C - E_F) \quad (7.8)$$

As outlined in Chapter 6 and similar to the room temperature, this difference at 150 K can be determined using the equation (6.1). Taking in to account the electron concentration of the melt-grown In_2O_3, $n=1.5\times10^{17}$ cm^{-3} at LT and applying the equation (6.1), E_C-E_F is obtained to be (0.025±0.006) eV at this temperature. Therefore, χ_{In2O3}= (4.18±0.06) eV at RT and χ_{In2O3}= (4.27±0.06) eV at LT.

7.6 The study of Metal-In_2O_3 contacts by ARPES

Metal (Ag, Au, Cu, In and Sn) contacts on melt-grown-In_2O_3 (111) single crystals were studied using angle-resolved photoemission spectroscopy by monitoring the band

bending of the In 4d core levels and valence band spectra, with correction for the photovoltage effect. The measurement was performed through stepwise metal evaporation onto the (111) surface of In_2O_3 at room temperature (RT) as well as low temperature (LT) 150 K for all metals, excluding the case of Ag. Evaporation of metals (purity: 99.99%) onto the In_2O_3 (111) surface was performed from a tungsten coil in a preparation chamber separate from the analyzer chamber at an operating pressure of 5×10^{-10} mbar. The photoemission spectra were taken at a base pressure of 2×10^{-10} mbar. The evaporation process was repeated several times under constant heating conditions and stopped when the observed photoemission spectrum looked like that of a thick metal overlayer.

Ag/In_2O_3 contact

In order to study the band bending as a function of Ag thickness, ARPES spectra of the In 4d core levels and the valence band were acquired. In Fig. 7.10 (a) selected EDC of the In 4d semi-core level are shown for increasing Ag thickness given by the evaporation time. In 4d line shape was fitted for each evaporation step by using the same procedure described to fit the clean core-level data in the previous chapter. Two examples of the fitted core-level are shown in Fig. 7.10 (b) for the clean as well as for the Ag covered sample surface (here after 5 s evaporation time). Directly evident from this thickness-dependent series of measurements are the decrease of the intensity and the energy shift of the emission line.

With increasing Ag thickness the In 4d lines shift continuously to lower binding energies due to an upward band bending, see e.g. Fig. 7.10 (b). Saturation of the bending of (0.15±0.05) eV is reached after about 5 seconds of evaporation time. As depicted in Fig. 7.10 (c), the band bending determined using the most intense peak of the valence band for the clean In_2O_3 (111) surface attained the same saturation value of (0.15±0.05) eV as the In 4d-core level after about 5 seconds evaporation of Ag. Gradually, Ag states appear at higher thicknesses in the valence band, and after 320 s, only the Ag spectrum could be measured. Fig. 7.10 (d) summarizes the energy shift of the core level and the valence band as a function of evaporation time. Since no surface or interface state appears, and no sign of chemical reaction was observed during different steps of the Ag growth, the measurement was performed only at RT for the case of this interface.

As discussed in section 7.4, the surface photovoltage effect has an impact on the determination of the barrier height [198, 201]. This effect leads to a barrier reduction. In Fig. 7.11, a series of normalized photoemission spectra are displayed in the vicinity of the Fermi energy with Ag thickness recorded at photon energy of 18 eV. After 40 s Ag

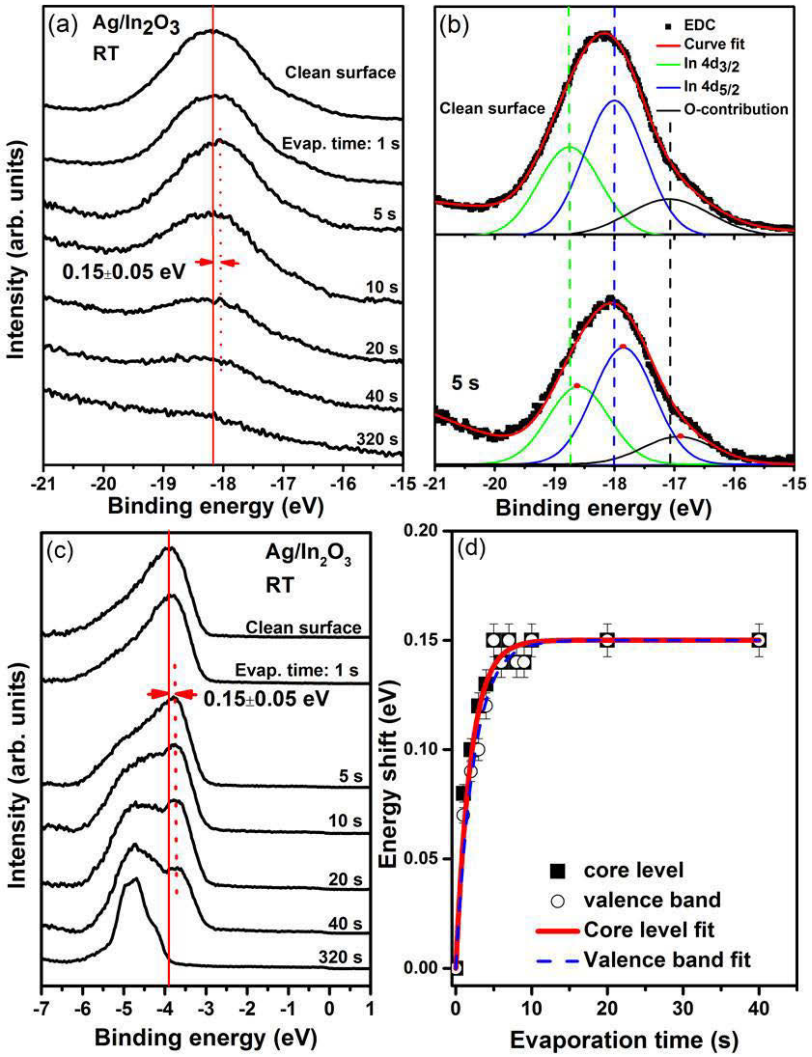

Figure 7.10: (a) Selected ARPES spectra of the In 4d semi-core level of an Ag/In_2O_3 contact as a function of Ag thickness at RT. The photon energy was 35 eV. (b) Two examples of the fit results of the In 4d spectra of the clean surface of In_2O_3 and after 5 s Ag evaporation, consisting in three components, the In $4d_{5/2}$-In $4d_{3/2}$ spin orbit doublet and the O-contribution line on the lower binding energy side. The red dots in the lower half show the maxima of the three fit components. (c) Selected ARPES spectra series of valence band of In_2O_3 (111) with different Ag evaporation times at RT, taken at photon energy of 18 eV. (d) Summary of the energy shifts of the In 4d semi-core level and intensity maximum of the valence band as a function of evaporation time.

deposition a distinct Fermi edge emerged, shifted to higher binding energy of (0.07±0.02) eV. After 320 s, for a thick Ag-layer, the Fermi level coincides with the reference Fermi energy. The Ag thickness-dependent photoemission spectra series, therefore, yield a small but distinct Schottky barrier of Φ_B= (0.22±0.07) eV, which is the sum of band bending (Fig. 7.10 (d)) and photovoltage (Fig. 7.11).

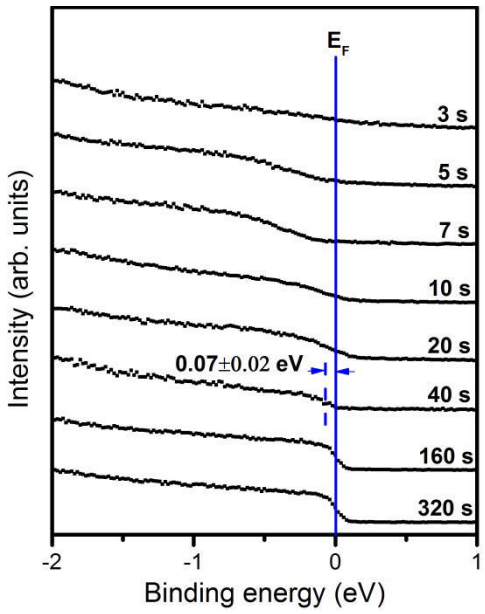

Figure 7.11: Selected normalized ARPES spectra series near the Fermi energy of the clean In_2O_3 (111) surface and after different evaporation times at RT, taken at a photon energy of 18 eV. A clear Fermi edge develops after approx. 40 s evaporation time which is shifted by 0.07 eV due to an appearing photovoltage.

A second method to determine the Schottky barrier height of metal-semiconductor contacts is to apply the Schottky-Mott rule. As mentioned earlier, its application is restricted by the assumption that the surface as well as the metal-semiconductor interface has to be free of surface and interface states, respectively. If a sufficient density of these states existed, the charge transfer via these states would dominate the interface formation resulting in a reduced or even vanishing band bending. But if the Schottky-Mott rule can be applied the barrier height is given by the equation (7.1) for the n-type semiconductors. So, the work function of Ag is required in addition to the

electron affinity of In_2O_3 which was discussed in previous section. Fig. 7.12 represents the low and high kinetic energy edges of a thick layer Ag on the crystal In_2O_3 at RT.

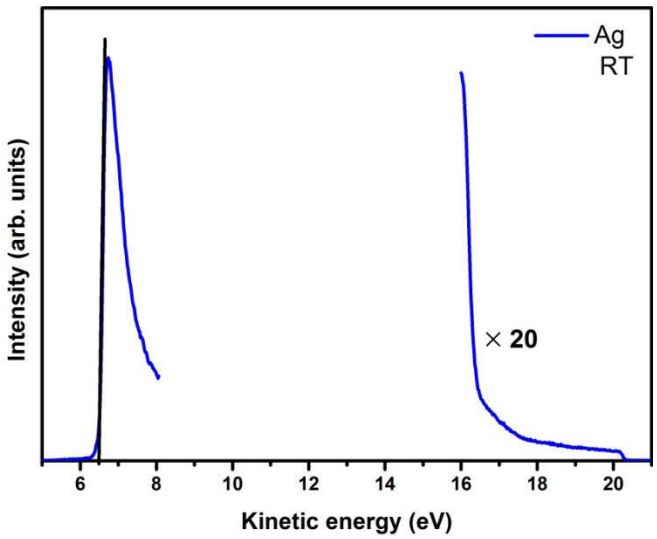

Figure 7.12: Low and high kinetic energy sides of the EDC spectra of thick Ag-overlayer on In_2O_3 (111) at RT, recorded at photon energy of 18 eV and 7 V sample bias.

According to this figure, the work function of silver is (4.30±0.05) eV. Substitution the corresponding values in the equation (7.1) yields the barrier height calculated according to the Schottky-Mott rule $\Phi_{Bn}^{S\text{-}M}$= (0.12±0.11) eV. This value is in good agreement with the barrier height obtained from the experimental band bending of Φ_B= (0.22±0.07) eV, discussed above [203]. The weakly higher barrier height from band bending might originate from the tendency of Ag to oxidize. An increase of the laterally homogenous barrier height has been observed previously in Ag/ZnO and also AgO/ZnO contacts [21, 204].

Last, the experimental results were compared with the electronegativity concept and metal-induced gap states (MIGS) based models. In these models the laterally homogenous barrier height is expressed by equation (7.4), yielding $\phi_B^{\text{hom}} = \phi_{bp}^{n} + S_X(X_{Ag} - X_{In_2O_3})$. Employing the same derived values for the Φ^{n}_{bp}, S_X, and X_{In2O3} as the ones in Ref. [15] and considering X_{Ag}=4.45 eV [189], one obtains $\Phi_{B,Ag}^{\text{hom}}$= -0.4 eV+0.395×(4.45 eV-5.73 eV)= -0.91 eV. This determined barrier height is inconsistent with the formation of the Ag/In_2O_3 Schottky contact of Φ_B = (0.22±0.07)

eV demonstrated in the present experimental work. A similar disagreement has been also reported for ZnO and Au, Pd, and Pt/In_2O_3 contacts [15, 21].

Au/In_2O_3 contact

Motivating by the higher work function of another noble metal, Au, Au-In_2O_3 (111) contacts were studied. The results, which were analyzed in a way similar to Ag/In_2O_3 interfaces, will be discussed in the present subsection. Figure 7.13 (a) displays the core level spectra for different Au coverages at RT, excited at photon energy of 35 eV.
In addition to the suppression of the In 4d core levels by Au coverage, one can identify a chemical shift to higher binding energies for higher evaporation time. The chemical shift evidenced the possibility of the chemical reaction in Au-In_2O_3 interfaces at RT. It is compatible to the chemical reaction between In-based compounds and gold at room temperature [205]. In Fig. 7.13 (b) the two examples of the fit results for the as-cleaved and also after 5 s of evaporation time are shown, revealing the upward band bending of (0.15±0.05) eV. Fig. 7.13 (c) shows the roughly similar upward band bending of the VB upon Au evaporation at RT. The results of the energy shift of the spectra in these two regions of binding energies are summarized in panel (d) of this figure. Fig. 7.14 demonstrates the photoemission spectra of an Au/In_2O_3 interface at different Au thicknesses corresponding to the Fermi energy region. It shows the appearance of the Fermi edge and its shift by (0.06±0.02) eV with respect to the reference Fermi energy due to the SPV. The barrier height is derived to be Φ_B= (0.15±0.05) eV+(0.06±0.02) eV= (0.21±0.07) eV, and the contact is therefore of Schottky character.

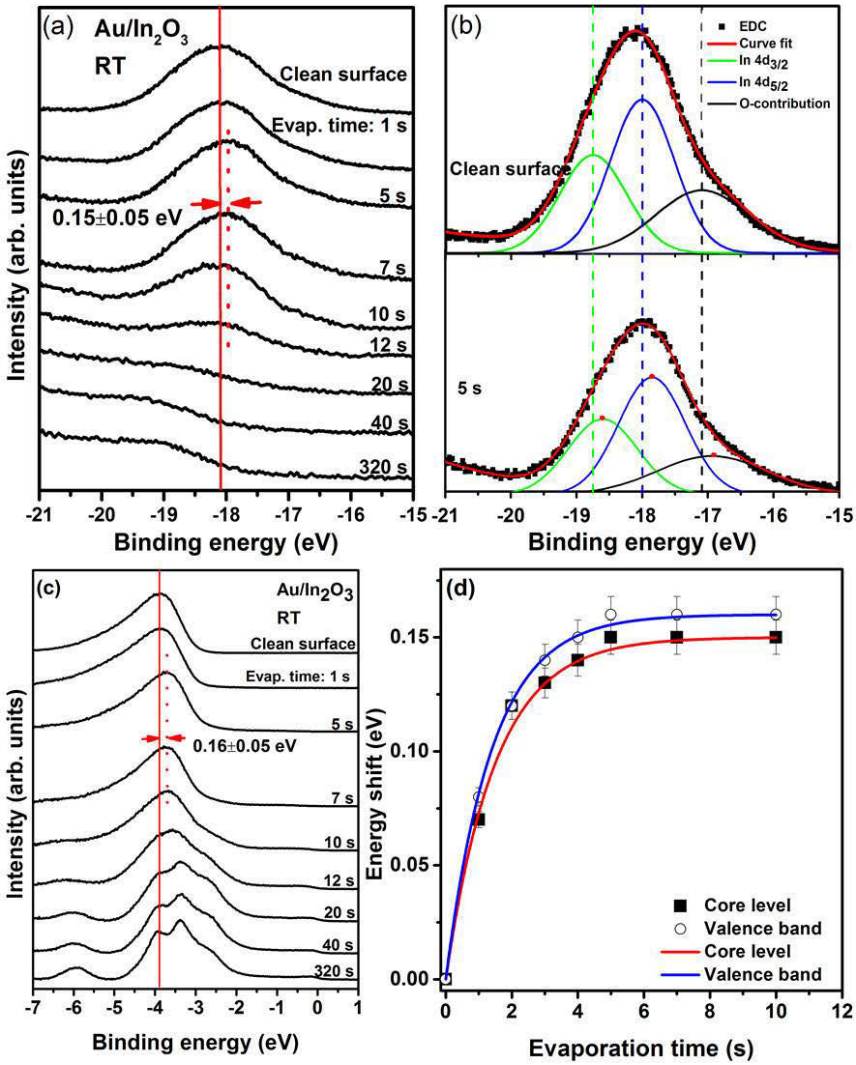

Figure 7.13: (a) Selected EDC series of the In 4d core level of the as-cleaved In_2O_3 and with increasing deposition of Au at RT and at excitation energy of 35 eV. (b) Two examples of fit results of the core level spectra of the clean surface of In_2O_3 and after 5 s Au evaporation. (c) Series of photoemission spectra of valence band of In_2O_3 (111) as a function of Au evaporation times at RT, excited at photon energy of 18 eV. (d) Summery of the energy shifts of the core level and intensity maximum of the valence band vs. evaporation time.

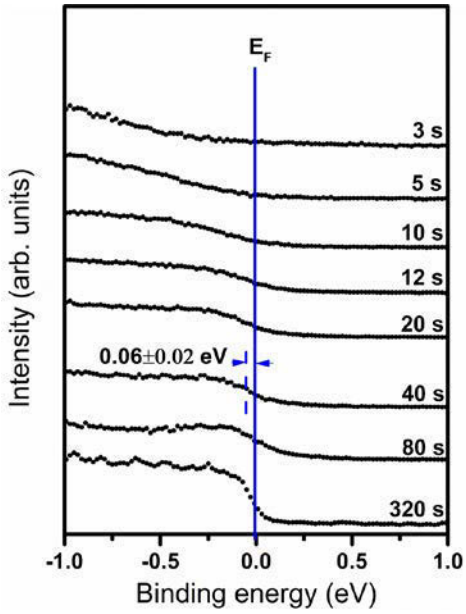

Figure 7.14: (a) ARPES spectra of an Au/In_2O_3 contact near the Fermi energy at RT and at excitation energy of 18 eV. It reveals the evolution of the Fermi edge of deposited Au layer and its shift to higher binding energy by (0.06±0.02) eV as a result of the photovoltage effect.

From Fig. 7.15, the work function of thick Au-layer on In_2O_3 was determined to be (4.85±0.05) eV, which is obviously lower than the reported value for the work function of gold [206]. It might be due to the chemical reaction and alloy formation which was discussed earlier. The Schottky-Mott rule predicts the barrier height of (0.67±0.11) eV, which does not agree with the experimental value.

As shown in Fig. 7.16 (a), a nearly-free electron state can be observed in a thick Au-layer (640 s), which was prepared at RT. The spectrum was taken at photon energy of 18 eV and at temperature of 20 K to improve the resolution. The two dimensionality of this state is apparent from the panel (b) of this figure, showing the lack of the photon-energy dispersion of the state. The figure 7.16 (c) depicts the parabola fit of dispersion of the state. The effective mass, binding energy of the bottom of the band and the Fermi momentum were derived to be (0.28±0.05) m_0, (0.43±0.05) eV, and ±(0.16±0.02) $Å^{-1}$. These values share many properties with Au (111) Shockley surface state [207] and indicates that the Au films grow ordered on In_2O_3 (111) at this temperature.

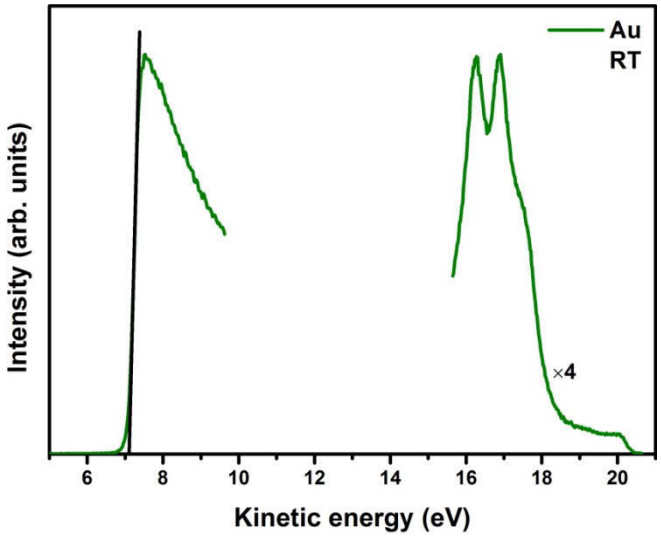

Figure 7.15: EDC spectra of low and high kinetic energy sides of thick Au-layer (320 s) measured at photon energy of 18 eV and 7 V sample bias and at room temperature.

The Shockley surface state [208] are usually observed on (111) surface of the noble metals with single crystalline structure. However, two distinct parabola are typically detected at the surface of Au (111) single crystals [207] as a result of the Rashba-Bychoff effect [209]. This effect is in fact a momentum-dependent spin-splitting of the two-dimensional states, which associated with spin-orbit coupling and asymmetry of the potential perpendicular to the surface.

The reason of the absence of the splitting of the bands in the thick Au-overlayer on In_2O_3 (111) might originate from the imperfection of the sample's surface and/or the difference in the sample preparation.

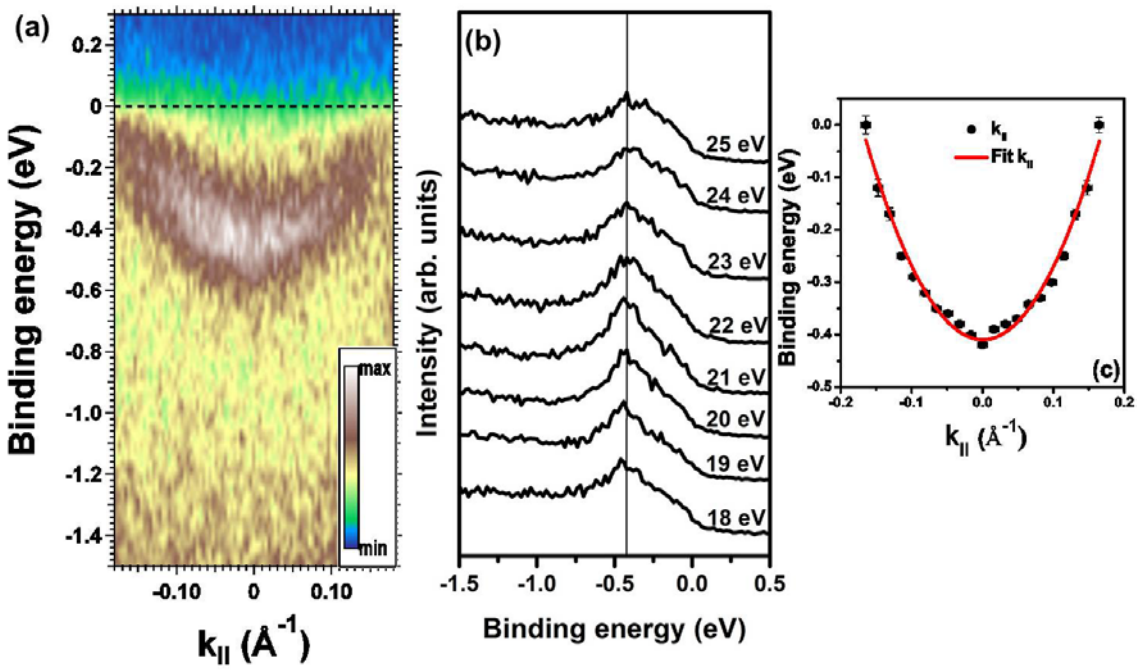

Figure 7.16: (a) ARPES photocurrent map of the thick overlayer of Au on In_2O_3, the Au was evaporated at RT. The spectrum was taken at excitation energy of 18 eV and at temperature 20 K for better resolution. (b) ARPES spectra in normal emission of near-E_F region of the thick layer Au at different photon energies. (c) The parabola fit of the free-electron like state in panel (a).

Due to the observed evidence of the possibility of chemical reaction in Au-In_2O_3 interfaces and also the Shockley-surface state on thick Au film prepared at RT, the measurement was conducted at 150 K as well to suppress the reactivity of the metals. The Figures 7.17 (a) to (d) show the band bending of the core-level spectra, two examples of the fitting results of the core-level spectra, the band bending of the VB spectra, and the summary of the energy shift of the spectra in the aforementioned regions upon Au coverages at LT, respectively. Au deposition results in larger upward band bending of (0.26±0.05) eV at LT compared to the one at RT. No sign of the chemical shift can be detected in the core level spectra by Au at this temperature, hinting to the occurrence of the chemical reaction at room temperature. As shown in Fig. 7.18, the surface photovoltage effect yields the shift of the spectra to higher binding energies by (0.10±0.02) eV. The larger shift to higher binding energies is in accordance with the higher band bending and the lower temperature of the contact preparation and therefore lower recombination rate.

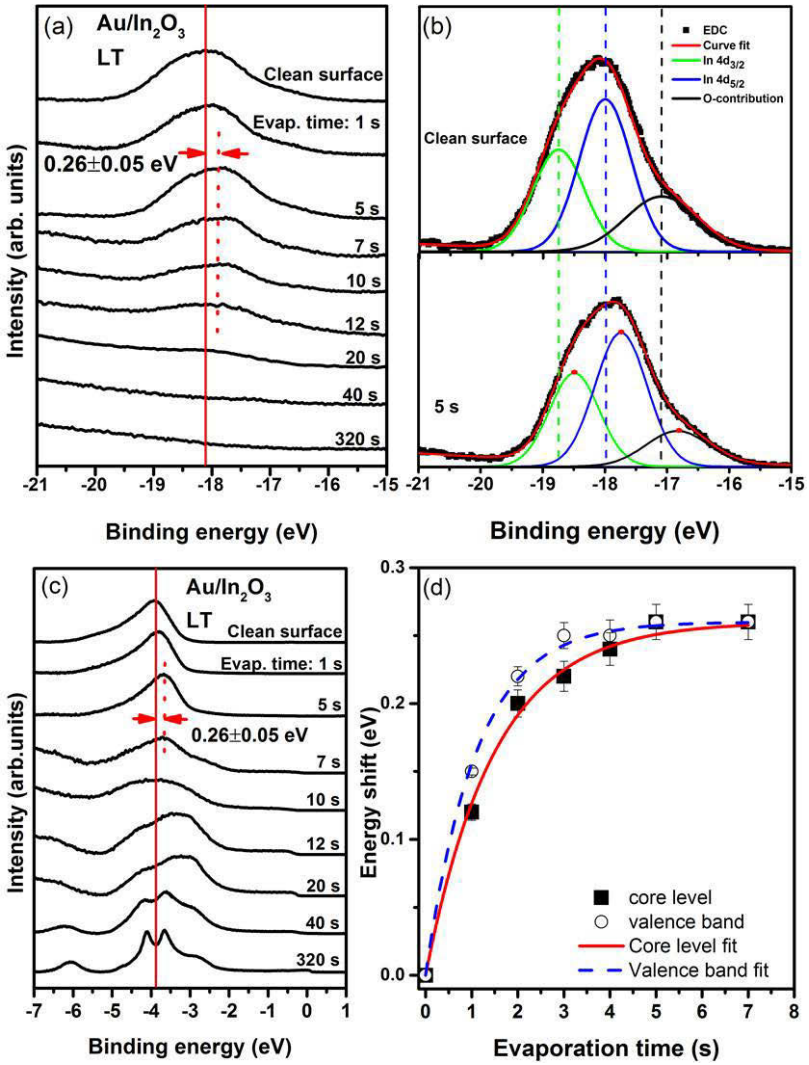

Figure 7.17: (a) Selected photoemission spectra of the pristine In_2O_3 as a function of the Au evaporation time in the In 4d-core level region at LT. (b) Two examples of fit results of the core level spectra of the clean surface of In_2O_3 and after 5 s Au evaporation at LT. (c) EDC series of valence band of In_2O_3 (111) as a function of Au coverages at LT, taken at photon energy of 18 eV. (d) Summery of the energy shifts of the core level and intensity maximum of the valence band as a function of evaporation time of Au.

For example, the complete compensation of the band bending was identified in clean surface of Si at low temperature [210]. The barrier height is determined to be Φ_B= (0.26±0.05) eV+(0.10±0.02) eV= (0.36±0.07) eV. Moreover, no surface state appears for the thick Au-layer at LT, indicating the difference and less homogeneity in Au growth on In_2O_3 at LT in comparison to that at RT. During deposition of Ag on Ag (111), transition of island growth shape from dendrites with triangular envelopes at temperatures below 140 K to more isotropic fractal islands at intermediate temperatures

and to distorted hexagonal shapes at temperatures higher than 170 K have also been realized by STM and kinetic Monte Carlo simulation as well. This result reveals the dependence of silver growth shape on temperature in Ag/Ag (111) system [211].

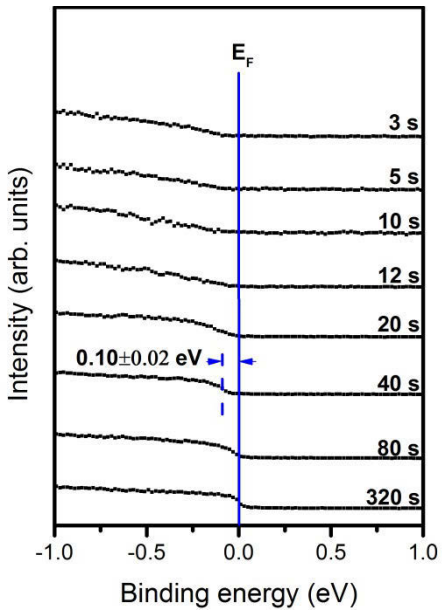

Figure 7.18: The EDC series of In_2O_3 upon Au evaporation in the vicinity of the Fermi energy.

The work function of a thick Au-film was obtained to be (5.27±0.05) eV in agreement with Ref. [201, 207], leading to Φ_{Bn}^{S-M}= (0.99±0.11) eV at LT. The value of the SBH predicted by the Schottky-Mott rule for the Au/In_2O_3 contact at both temperatures is too high with respect to the experimental one independently obtained by photoemission. We attribute this difference to the formation of new chemical bonds at room temperature, a phenomenon neglected by the Schottky-Mott rule.

Furthermore, from equation (7.4), one can obtain $\Phi_{B,\,Au}^{hom}$= -0.63 eV, where X_{Au}=5.15 eV [189] in Miedema unit. The MIGS-based model predicts an ohmic contact for Au-In_2O_3 interfaces, whereas experiments show the Schottky behavior of the studied contacts. Since no emission of the bottom of conduction band was detected within band gap in the non-degenerate In_2O_3 crystals studied in the present work, the value of Ref. [9] was used for the branch-point energy. However, the negative value (Φ^{n}_{bp}= -0.4 eV) employed, resulted in the obvious discrepancy. The charge neutrality level concept

therefore is not capable of describing the Ag and Au contact on the UHV-cleaved In_2O_3 (111) surface. A Schottky-like behavior has been already reported for In_2O_3 thin films after elimination of the surface accumulation layer (SEAL) by surface treatments [10, 15]. The authors of Ref. [15] additionally pointed out that the removal of the SEAL on In_2O_3 thin films by sputtering contradicts with the CNL approach.

The positive barrier height, for the already discussed interfaces, indicates the presence of a charge depletion on the semiconducting side of the Ag and Au contacts on UHV-cleaved In_2O_3 (111) bulk single crystals, which contrasts with the existence of SEAL at the clean surface. These results are consistent with the flat surface bands of the studied crystals, which was described earlier. Therefore, surface accumulation is most probably not an intrinsic property of as-cleaved melt-grown bulk In_2O_3 single crystals and likely produced by growth and post-growth treatment conditions.

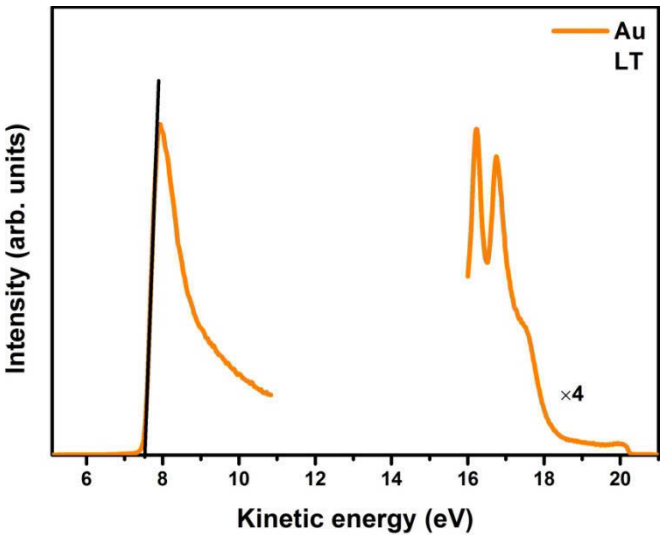

Figure 7.19: The low and high kinetic energy sides of the photoemission spectra for the thick Au-film, taken at LT.

Cu/In_2O_3 contact

The lightest noble metal, Cu, on In_2O_3 was studied as well. The results will be discussed in this subsection. As depicted in the Figures 7.20 (a) to (d) and in contrast to the other noble metals examined, Cu causes a slight downward band bending of (-

0.14±0.05) eV of the spectra in the In 4d and valence band regions at room temperature, revealing that the contact has an ohmic behavior. As expected for an ohmic contact, no photovoltage shift can be observed for a Cu/In_2O_3 interface, see Figure 7.21.

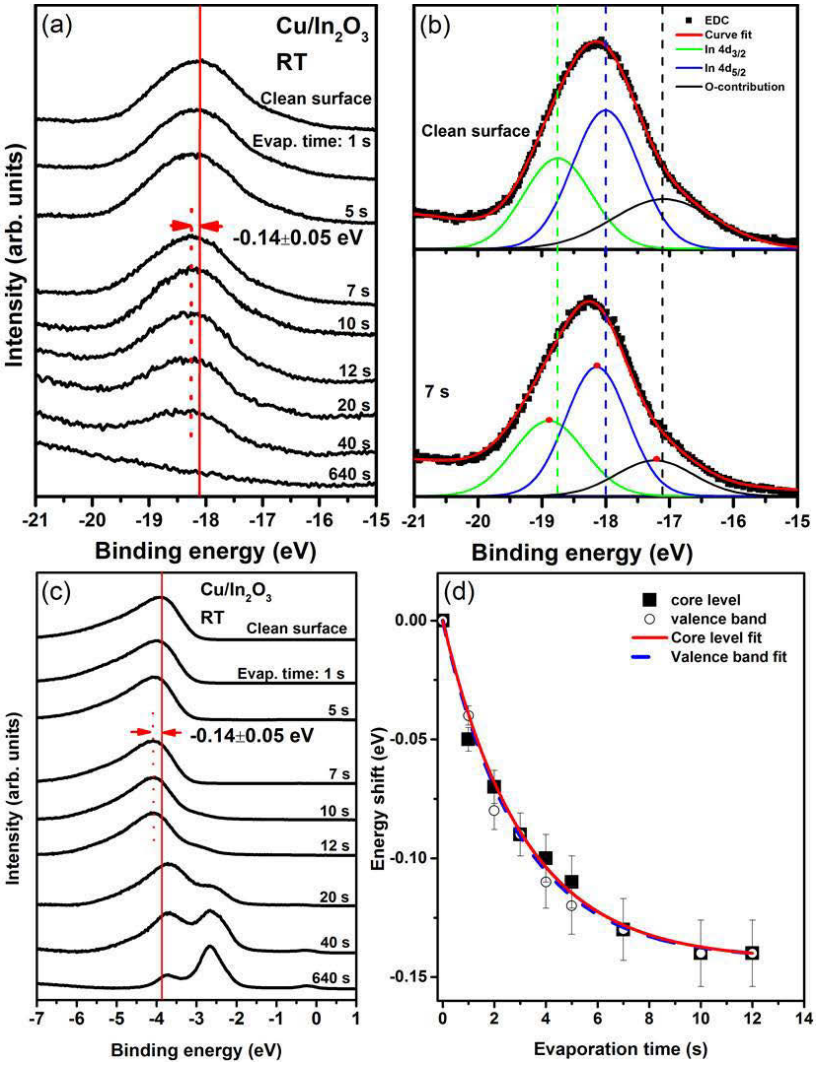

Figure 7.20: (a) A series of EDC spectra of the In_2O_3 as a function of the Cu evaporation time in the In 4d-core level region at RT. (b) Two examples of fit results of the core level spectra of the clean surface of In_2O_3 and after 7 s Cu evaporation at RT. (c) Photoemission spectra of the valence band of In_2O_3 (111) with Cu deposition at RT. (d) Summary of the energy shifts of the core level and the most intense peak of the valence band against the evaporation time of Cu.

It should be noted that the spectra in this figure were taken 10° off-normal due to the appearance of the Shockley-like surface state for higher coverages, which is discussed in the following. Thus, an ohmic contact with barrier height of (-0.14±0.07) eV was formed in a Cu/In_2O_3 interface.

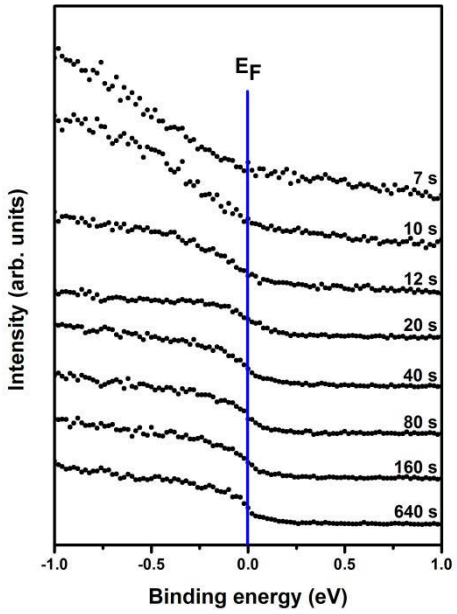

Figure 7.21: Normalized PE spectra of the pristine surface of In_2O_3 as well as after Cu coverage near the Fermi energy, the spectra were taken 10°-off normal. No SPV can be detected in this ohmic contact.

The work function of a thick Cu film on In_2O_3 was measured to be (4.51 ±0.05) eV at this temperature (Figure 7.22), yielding the Schottky barrier height of (0.33 ±0.11) eV.

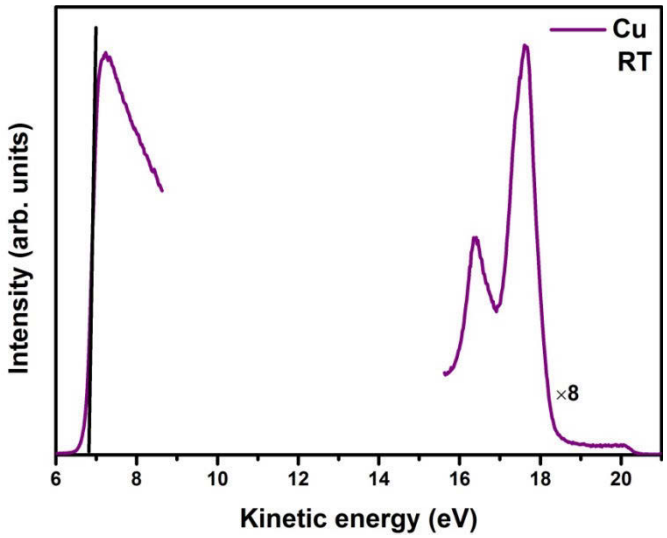

Figure 7.22: Photoemission spectra of a thick Cu film on In_2O_3 recorded 10°-off normal at excitation energy of 18 eV and a bias voltage 7 V at RT.

These results show a remarkable discrepancy between the experimental barrier height and the derived one from the Schottky-Mott rule. The Schottky-Mott rule predicts a Schottky contact, while the experiment shows its ohmic character.

The selected ARPES maps along the Γ-N direction of the bulk Brillouin zone for the as-cleaved and the low Cu-covered samples near the Fermi energy are demonstrated in Fig. 7.23 (a). The spectra recorded at hν=18 eV. At initial stage of Cu growth, a free-electron like state with parabolic dispersion emerges. As seen in the Figure 7. 23 (a), after 3 s of evaporation time this state has the maximum intensity, which gradually fades away at higher coverages. The nearly-free electron state vanishes after 7 s. The dispersion of the state at an evaporation time of 3 s was fitted by a parabola, yielding an m^*= (0.35±0.05) m_0, E_B= (0.40±0.05) eV, and k_F= ±(0.13±0.02) $Å^{-1,}$ Figure 7.23 (b). From these values, it is clear that this state differs from the two quantized subbands which were observed near-surface of In_2O_3 thin films [8]. Moreover, the state does not show $k_\perp$-dependency, revealing its two dimensionality character, Fig. 7.23 (c). Since the state is two dimensional, the surface charge density n_{2D} is calculated to be 2.69×10^{13} Cm^{-2} by using the formula relating the Fermi wave vector k_F and the charge density of a two-dimensional free electron gas [212]:

$$n_{2D} = \frac{k_F^2}{2\pi} \tag{7.9}$$

This estimated n_{2D} is substantially larger compared to the reported ones at conventional semiconductor interfaces [213].

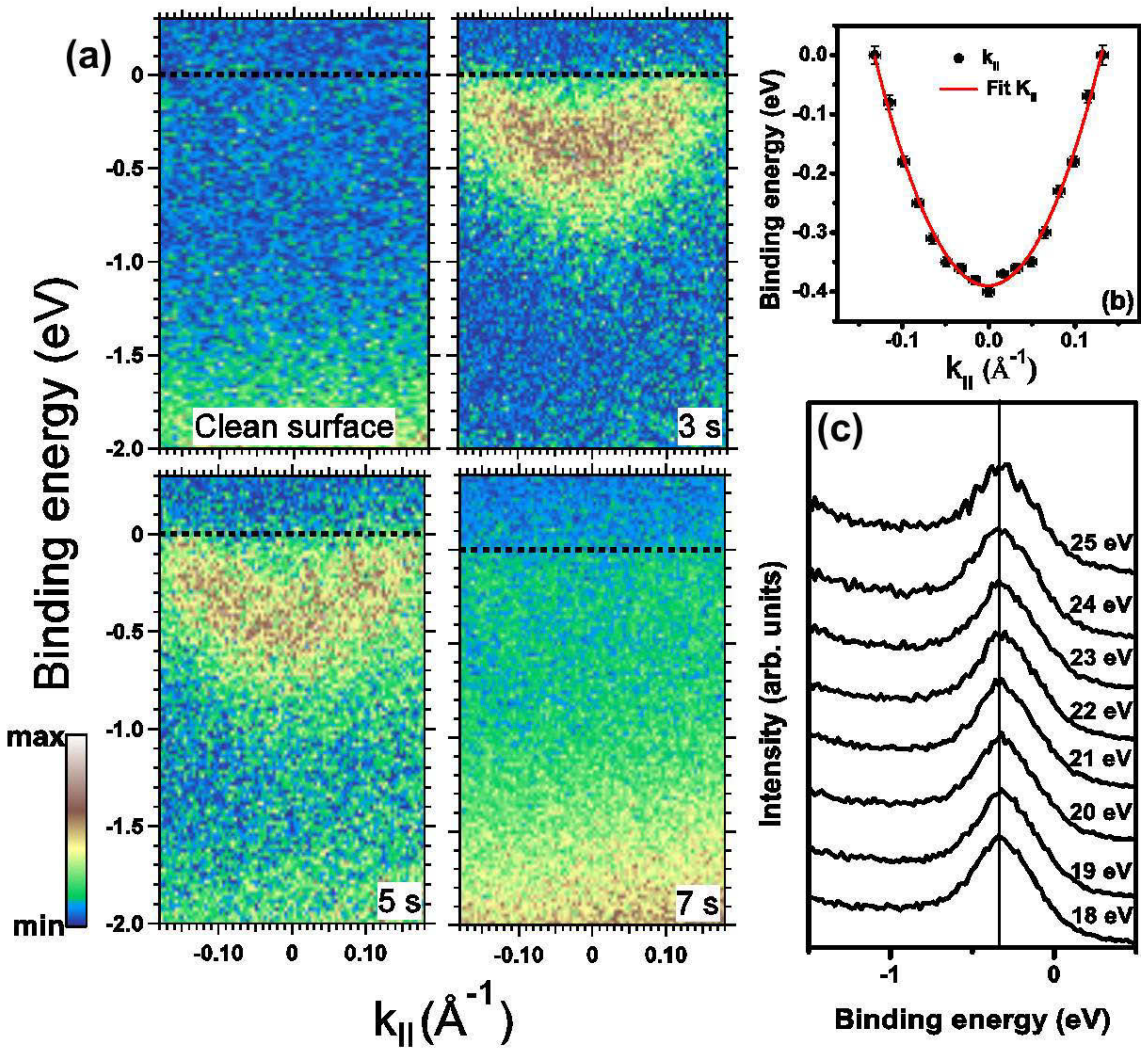

Figure 7.23: (a) ARPES photocurrent intensity maps of the near-E_F emission of the clean surface of In_2O_3 and low Cu-covered samples along Γ–N direction, taken at hν=18 eV. (b) Parabola fit using dispersion of the free-electron like state near the Fermi energy region for a low Cu-covered sample (after 3 s of Cu evaporation) (c) ARPES spectra in normal emission of near-E_F region of a low Cu-covered sample at different photon energies from 18 to 25 eV, revealing the 2D character of the state within the band gap.

As discussed earlier, the energy difference between the bulk Fermi level and bottom of the conduction band was determined to be 0.07 eV in the studied crystals. Considering this as well as the 2D character of the identified state, we conclude that the conduction band of In_2O_3 is not lowered below the Fermi level upon Cu evaporation. It is not surprising that the Schottky-Mott rule does not predict the right value of the SBH, given the presence of this 2D state.

We note that at higher coverages of Cu, another 2D state appears near the Fermi level on In_2O_3. Also this state has a parabolic dispersion and is of two-dimensional character, as depicted in figures 7.24 (a) to (c).

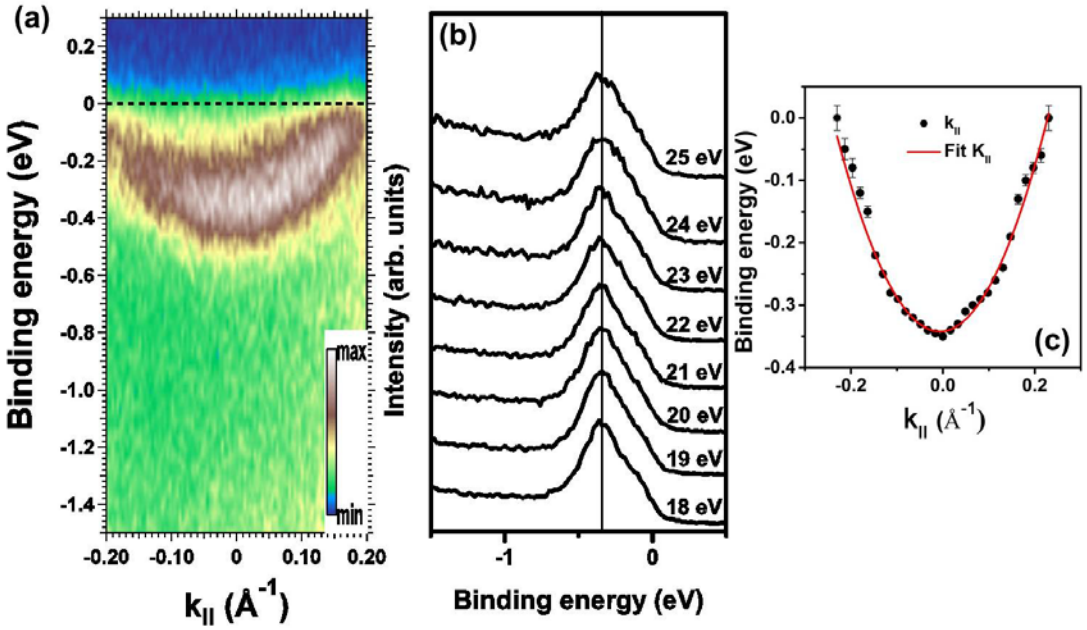

Figure 7.24: (a) ARPES maps of the near-Fermi level emission of the thick Cu layer on In_2O_3 measured at hν=18 eV and at 20 K. The thick film was prepared at RT. (b) Normal emission photoelectron spectra of the state at different excitation energies, showing the lack of the photon energy-dependency and accordingly 2D character of the Shockley-like state. (c) Parabola fit of the state near the Fermi energy in panel (a).

By fitting a parabolic function to the dispersion of the state, the effective mass, binding energy of the bottom of the band and the Fermi wave vector were found to be (0.58±0.05) m_0, (0.35±0.05) eV, and ±(0.23±0.02) Å^{-1}. These values differ from the values of the Shockley surfaces states measured on bulk single crystals of Cu (111), namely (m^*= 0.412 m_0, E_B= 0.435 eV, and k_F= ± 0.215 Å^{-1}) [214].

The higher effective mass and lower binding energy of the bottom of the band of the Shockley-like state in comparison to the bulk values indicate that this surface state is less bound. Copper have face-centered cubic (fcc) structure and bonding length of the atoms in Cu is derived to be around 2.56 Å from Ref. [215]. Since Cu and also In_2O_3 have cubic crystal structures and their bonding lengths (bonding length of In_2O_3~2.2 Å)

are comparable, the difference between the values of the state in the present study and the bulk ones in Cu film might be attributed to the strain as a result of the growth processes.

With the same motivation as for the Au/In_2O_3 contact, i.e. to suppress the surface reactivity which might induce the emergence of the nearly free-electron at initial stage of Cu growth on In_2O_3 as well as the surface state on a thick Cu film, the measurement was also performed at 150 K. An almost identical downward band bending of (-0.13±0.05) eV was observed at LT, as shown in Figures 7.25 (a) to (d). From Figure 7.26, one can identify the absence of the SPV for this ohmic contact at LT similar to the RT-results, leading to barrier height of (-0.13±0.07) eV. Analogous to the room temperature results, a 2DEG appears at low Cu-covered samples with similar m^*, E_B, and k_F values, and then vanishes for higher coverages at LT, revealing the formation of accumulation layer at the interface consistent with its ohmic behavior. The work function of copper at this temperature was measured to be (4.54±0.05) eV roughly identical to the RT-value (Fig. 7.27), yielded Φ_{Bn}^{S-M}= (0.27±0.11) eV inconsistent with the experimental value. Additionally, considering X_{Cu}= 4.55 eV in Miedema unit [189], the laterally homogenous barrier height within MIGS-base model $\Phi_{B,Cu}^{hom}$= -0.87 eV. This model predicts much larger ohmic barrier height compared to the experimental value. Similar to the Au growth on In_2O_3, no surface state was observed on a thick Cu film at LT, indicating the difference of growth modes at low and room temperature.

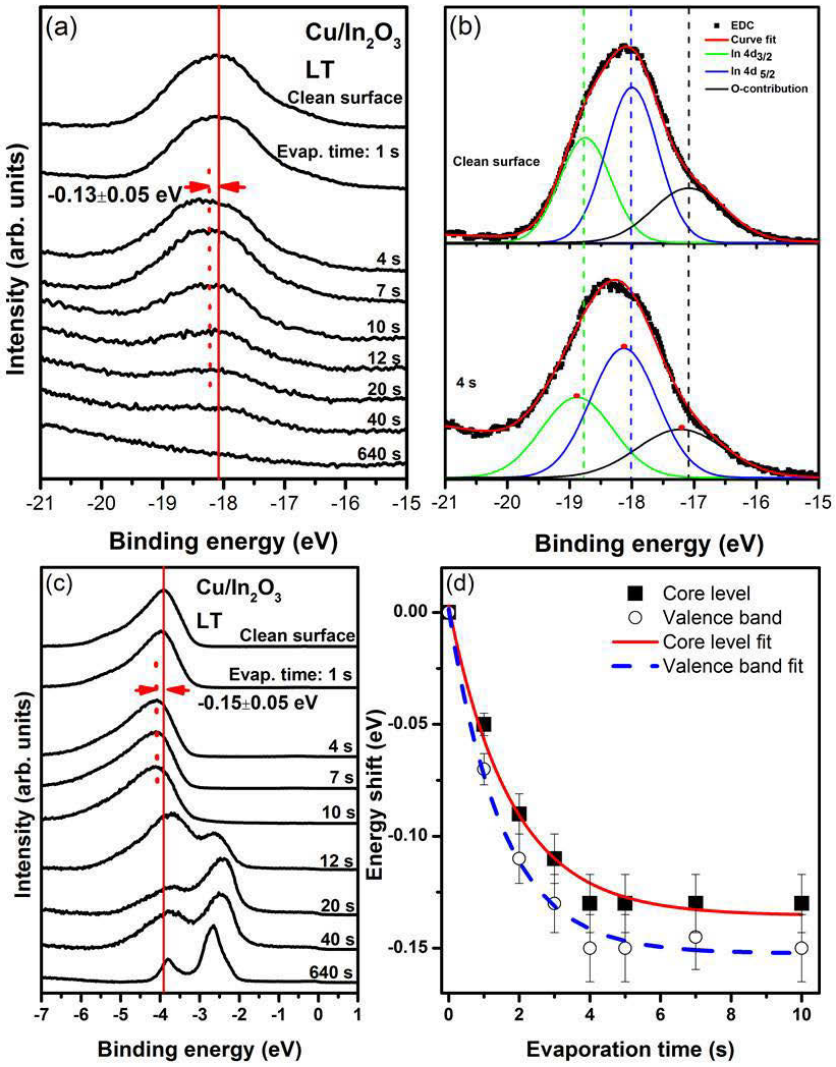

Figure 7.25: (a) Photoelectron spectra of the In 4d-core level of the pristine In_2O_3 and with increasing deposition of Cu at LT (a) and two examples of fit results of the spectra for the clean surface and after 4 seconds of evaporation time (b). (c) Photoemission spectra of the valence band of In_2O_3 (111) vs. Cu coverages at LT. (d) Summary of the band bending of spectra in Cu/In_2O_3 interfaces at LT.

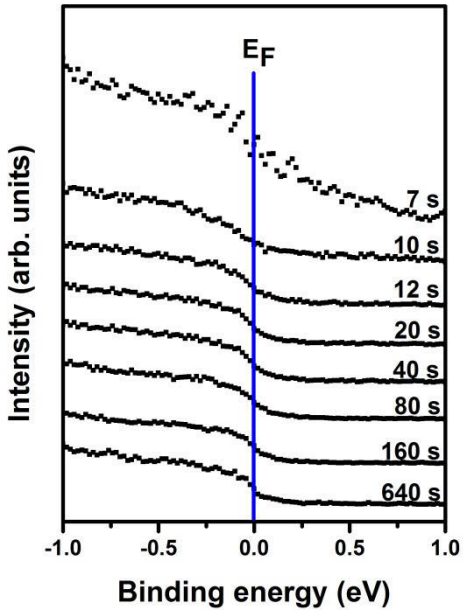

Figure 7.26: Normalized ARPES spectra series near the Fermi energy of the clean In_2O_3 (111) surface and after different evaporation times of Cu recorded at photon energy of 18 eV at LT. No photovoltage effect can be detected for the ohmic Cu/In_2O_3 contacts.

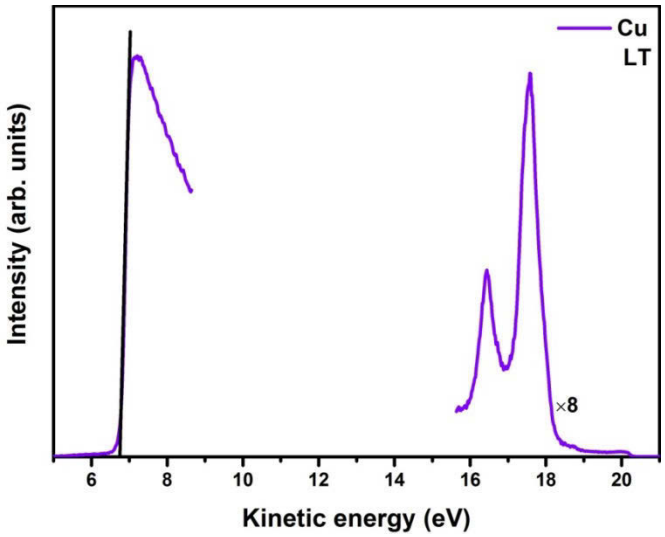

Figure 7.27: Photoemission spectra of a thick Cu film on In_2O_3 taken at excitation energy of 18 eV and a bias voltage 7 V at LT to obtain an in-situ measurement of the work function at LT.

In/In_2O_3 contact

The interfacial electronic structure of In-In_2O_3 contact was also studied, as the widely cited-work function of indium [216] is smaller than that of indium oxide.

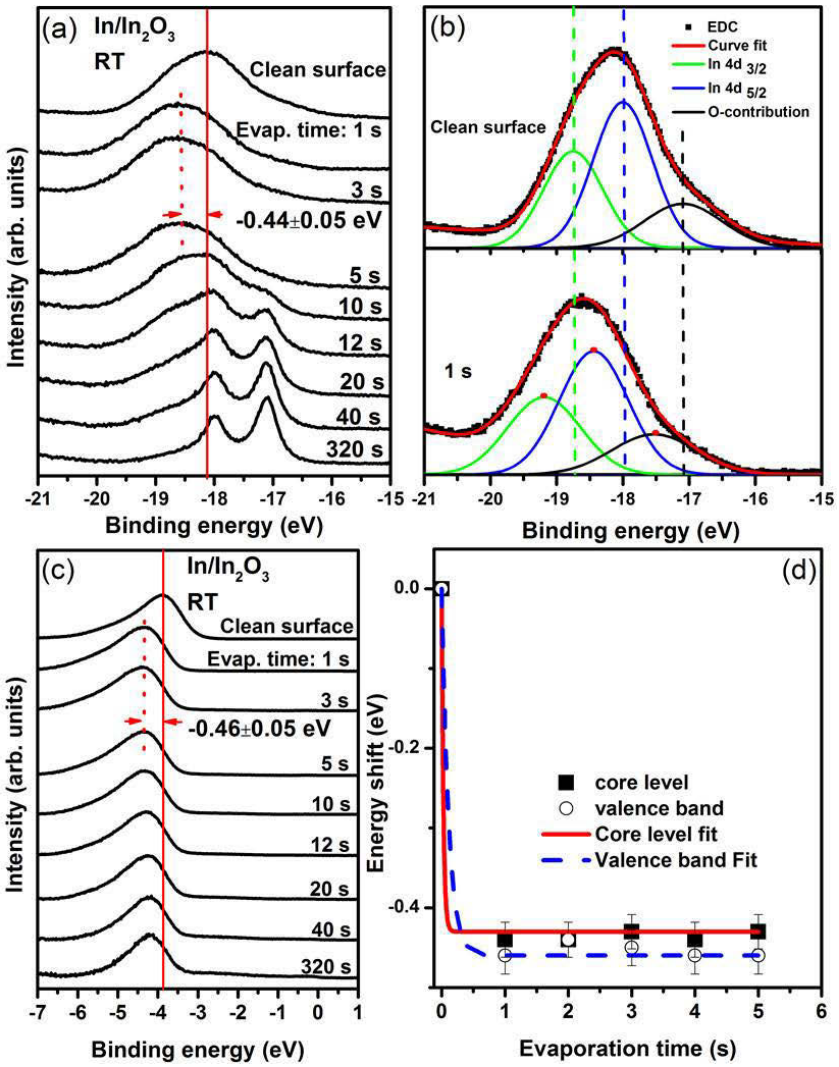

Figure 7.28: (a) Downward band bending of the In 4d-core level of In_2O_3 upon In evaporation at RT and gradual evolution of two distinct In $4d_{5/2}$ and In $4d_{3/2}$ doublets. (b) Two examples of fit results of the core level spectra of the clean surface of In_2O_3 and after 1 s In evaporation at RT. (c) Photoemission spectra of the valence band of In_2O_3 (111) for different In coverages at RT. (d) Summary of the energy shifts of the core level and intensity maximum of the valence band against the evaporation time of In.

Figures 7.28 (a) and (b) show the core level spectra for different In coverages, and two examples of fitting results (as-cleaved and after 1 s of evaporation time), respectively. One can see a clear shift of the three components to higher binding energies after 1 s

indium deposition in panel (b). As shown in Figures 7.28 (a) to (d), metallic indium generates a downward band bending of (-0.44±0.05) eV. As expected no photovoltage effect was observed in this ohmic contact, Fig. 7. 29. The work function of a thick layer of In on In_2O_3 samples was derived to be (4.02±0.05) eV, see Fig. 7. 30.

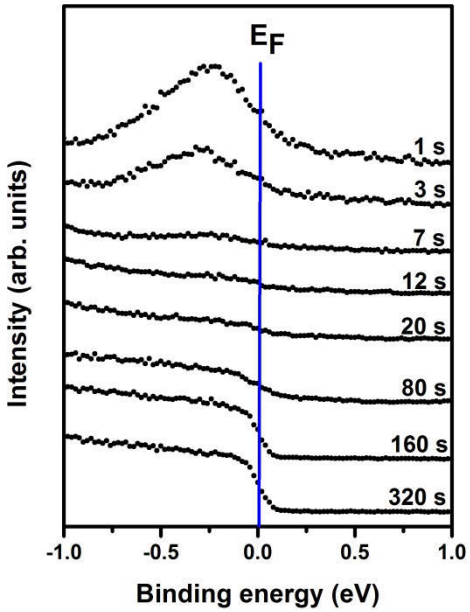

Figure 7.29: Normalized ARPES spectra series E_F of the clean In_2O_3 (111) surface and after different evaporation times of In recorded at photon energy of 18 eV at RT. In addition to the absence of the photovoltage effect, one can observe the emergence of a state near-E_F for low In-covered samples (1 s and 3s of evaporation time).

Substitution of this value and the *in situ*-deduced electron affinity of the studied crystals in equation (7.1) results in barrier height of (-0.16±0.11) eV from the Schottky-Mott rule, once again proving the disagreement between the experimental barrier height and predicted one from the Schottky-Mott rule.

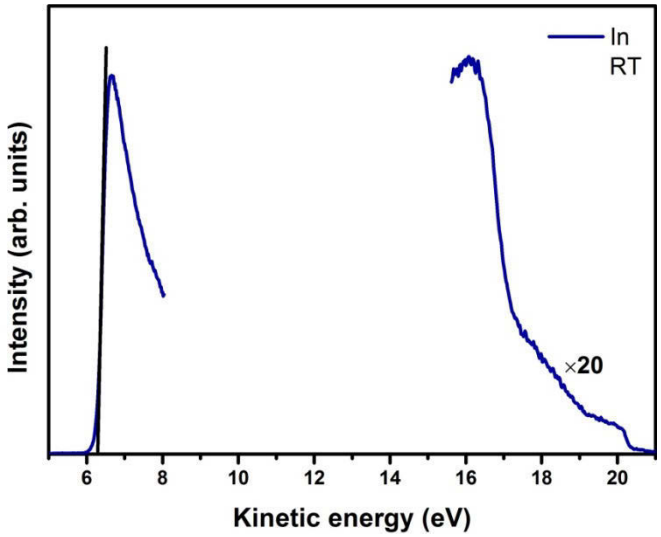

Figure 7.30: Low and high kinetic energy sides of ARPES spectra for a thick In film on In_2O_3 (111), hν=18 eV and bias voltage of 7 V at RT.

Figure 7.31 (a) shows the selected photoemission intensity maps along Γ–N direction of the bulk Brillouin zone for the pristine and the low In-deposited samples near the E_F recorded at hν=18eV. After 1 s of In evaporation, a nearly free-electron state with parabolic dispersion appears. Its intensity increases up to 3 s evaporation time, gradually blurring and vanishing for evaporation times higher than 5 s.

Fig.7. 31 (b) displays the parabola fit of the dispersion of the state in the vicinity of the Fermi energy after 3 s In evaporation. The E_B of the bottom of the band, m^*, and k_F are deduced to be (0.28±0.05) eV, (0.38±0.05) m_0, and ± (0.16±0.02) $Å^{-1}$, respectively [217]. Similar to the 2D state which was observed at Cu/In_2O_3 interfaces, these values differs from those of the two dimensional electron gas which were identified on In_2O_3 (111) thin films [8]. From the panel (c) of the Fig. 7.31 is clear that the state is two dimensional. Its surface charge density is estimated to be 4.08×10^{13} Cm^{-2} using the relation (7.9). This value is comparable with n_{2D} of the 2DEG on the pristine surface of In_2O_3 thin films [8], and much larger than that at classical semiconductor interfaces [213]. As clarified earlier for the case of Cu/In_2O_3 contacts, this state cannot be associated with CB.

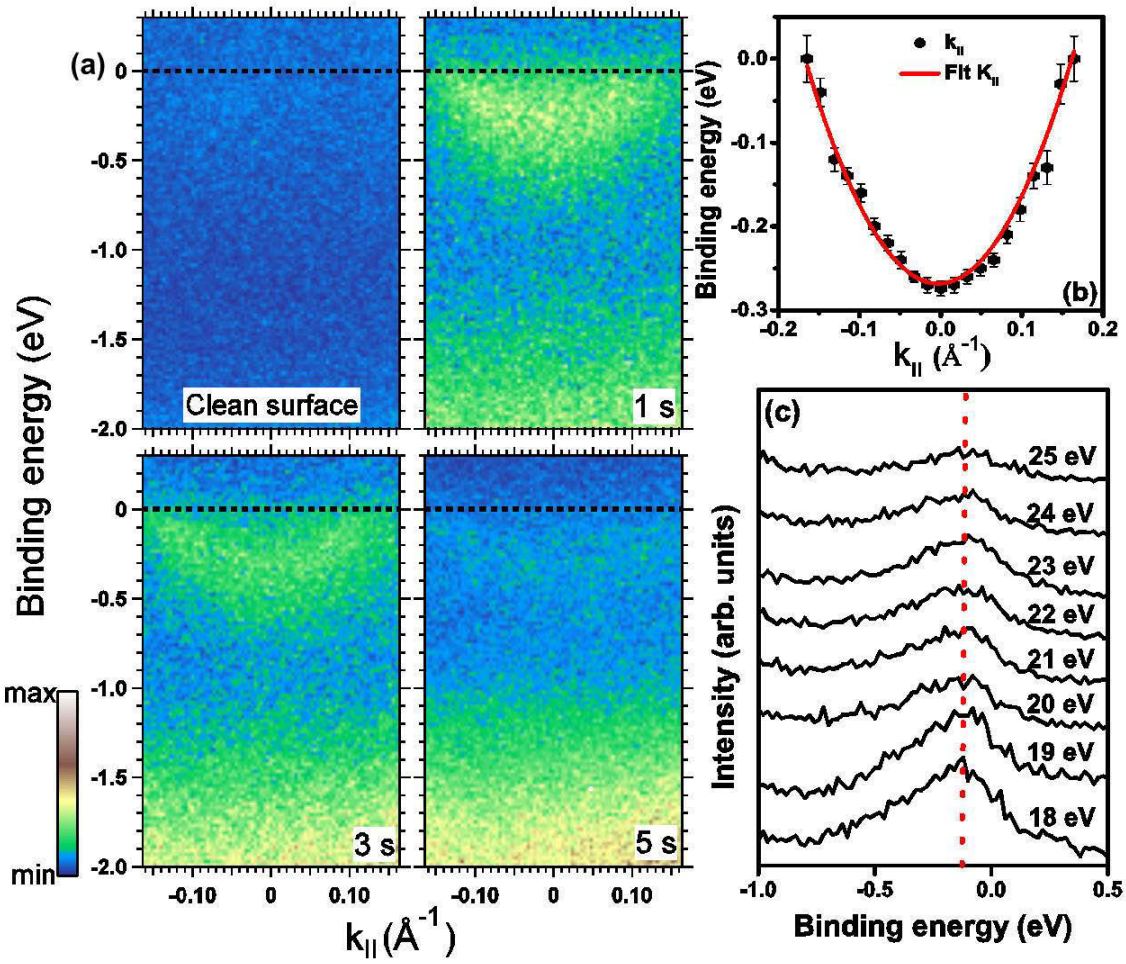

Figure 7.31: (a) ARPES maps of the pristine and the low In thicknesses along Γ–N direction of the bulk Brillouin zone, corresponding to the Fermi energy region and taken at hν=18 eV. (b) Parabola fit using dispersion of the nearly free-electron state near the Fermi region along Γ–N direction for a low In-covered sample (after 3 s of In evaporation time). (c) ARPES spectra in normal emission of near-E_F region of a low In-covered sample at different photon energies from 18 to 25 eV, revealing the two dimensionality of the state near the Fermi level.

Fig. 7.32 represents the ARPES spectra of as-cleaved In_2O_3 as well as thick overlayer of metallic indium on In_2O_3 recorded at excitation energy of 35 eV. The spectra were recorded at the same experimental conditions and normalized in the same way to the acquisition time and to photon flux.

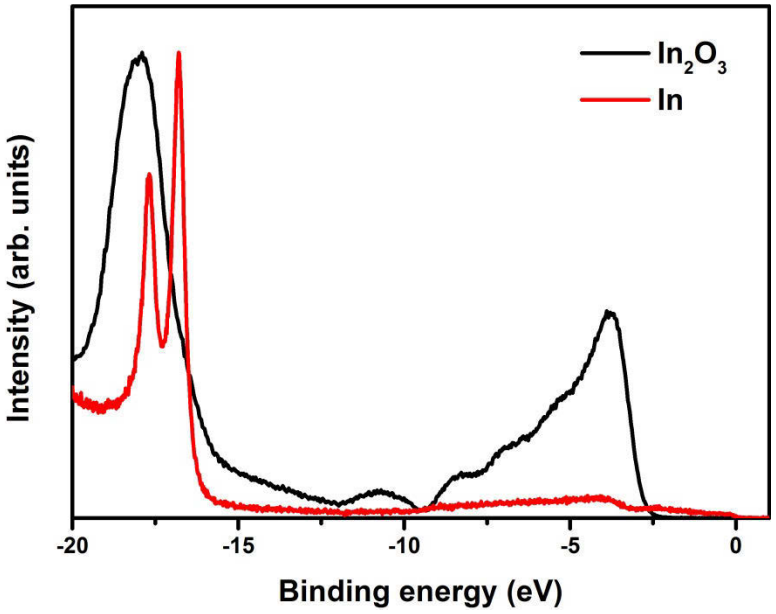

Figure 7.32: EDC spectra of as-cleaved In_2O_3 and also a thick In film (after 320 s of evaporation time).

To examine the temperature-dependence of above-mentioned phenomenology, the measurement was conducted at LT as well, and the data are summarized in Figure 7.31.

Figures 7.33 (a) to (b) imply a downward band bending of (-0.42±0.05) eV of the In 4d and valence band spectra at LT nearly similar to RT results. As shown in Fig. 7.34, SPV does not occur in this ohmic contact at this temperature. Also, a 2DEG appears with the same characteristic of the one at RT. From Fig. 7.35, one can derive the work function of thick In film Φ_{In}= (4.00±0.05) eV, leading to the barrier height of (-0.27±0.11) eV from Schottky-Mott rule at LT. Although the experiment barrier height and the predicted one from Schottky-Mott rule show the ohmic character of the interface at both temperatures, their values are inconsistent.

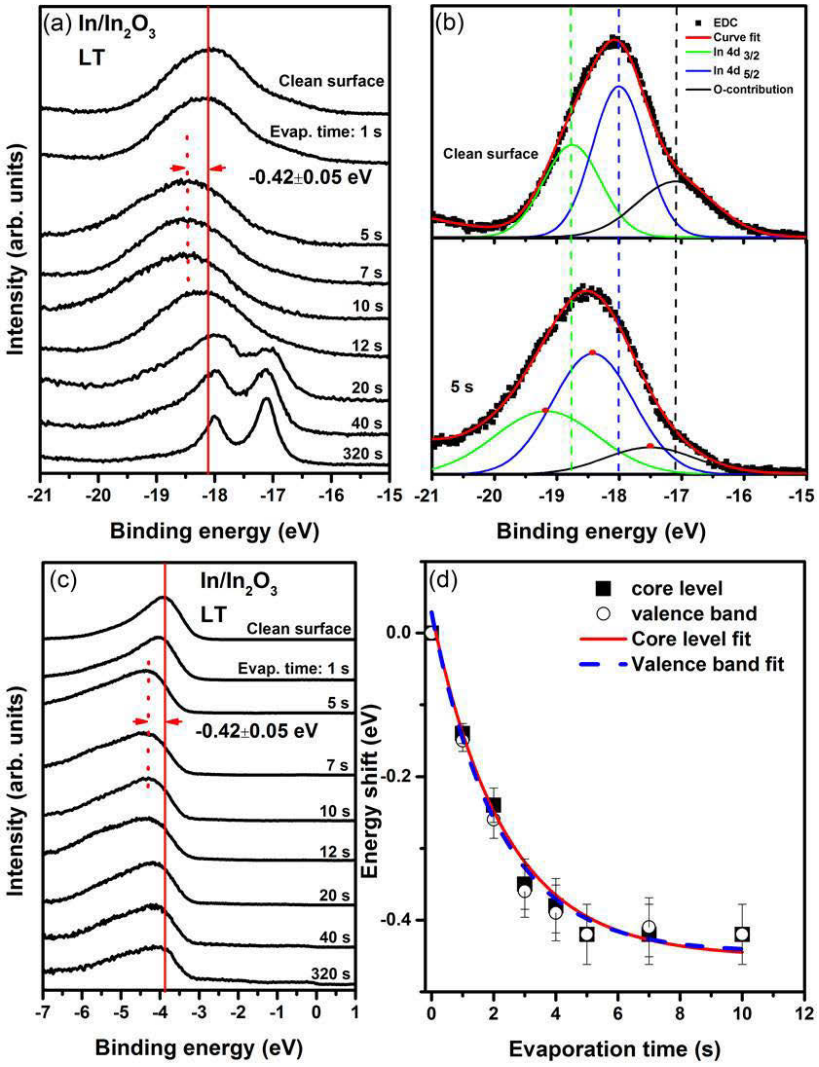

Figure 7.33: (a) In 4d spectra of In/ In_2O_3 (111) contacts for different metal thicknesses at 35 eV photon energy at LT and gradual evolution of two distinct In $4d_{5/2}$ and In $4d_{3/2}$ doublets of metallic indium. (b) Two examples of fit results of the core level spectra of the clean surface of In_2O_3 and after 5 s In evaporation at LT. (c) Valence band spectra of In/In_2O_3 (111) for different In coverages at LT, taken at photon energy of 18 eV. (d) Summary of the energy shifts of the core level and intensity maximum of the valence as a function of evaporation time.

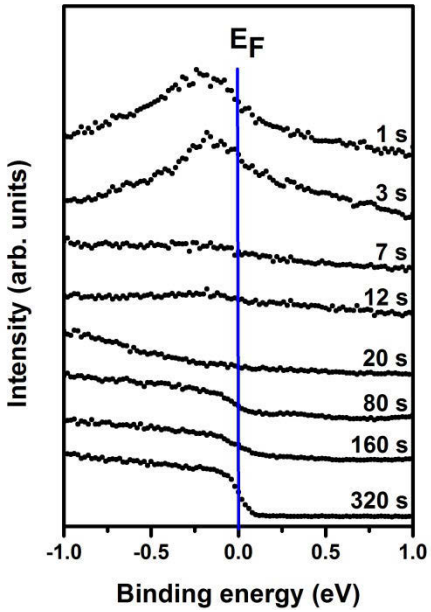

Figure 7.34: Near-E_F ARPES spectra series of In/In_2O_3 (111) contacts for different metal thicknesses at 18 eV photon energy at LT, showing the evolution of a state at initial stages of growth and its disappearance for higher coverages.

This discrepancy is in line with the observation of the 2D state, which shows that the governing conditions of In/In_2O_3 interface is beyond the assumptions underlying behind this rule. By employing the equation (7.4) and the electronegativity of the indium in Miedema unit X_{In}= 3.90 eV [189], the laterally-homogenous barrier height within metal-induced gap states model was determined to be -1.12 eV for this contact. The result also confirms the ohmic character of the interfaces, but the obtained-barrier height via this model is incompatible with the present experimental ones.

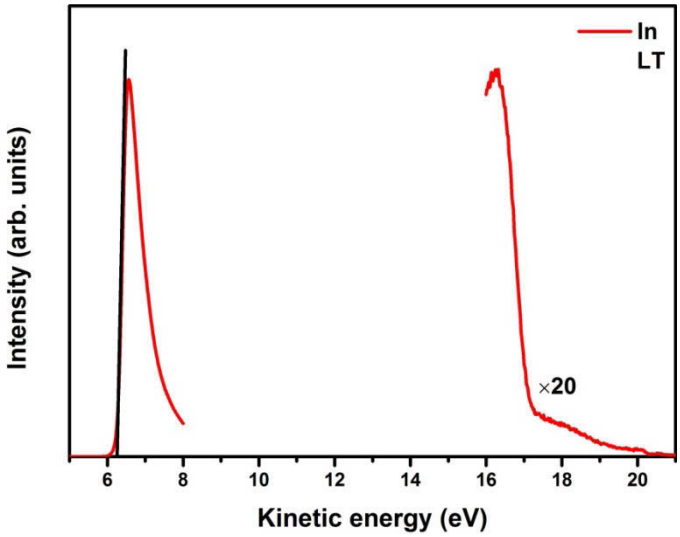

Figure 7.35 Low and high E_{kin} sides of spectra of thick In layer at LT.

Sn/ In_2O_3 contact

Sn was also evaporated on In_2O_3 (111) because it has only one electron more than In in the valence band. The selected EDC spectra in the Sn 4d, In 4d core levels, VB and near-E_F regions are shown in Figures 7.36 (a) to (d), respectively. As shown in panel (a), metallic Sn, whose signature is the spin-orbit split Sn 4d doublet, grows with no sign of a change in the line-shape, Fig. 7.36 (b), an indication that Sn remains metallic throughout the whole thickness range examined and does not oxidize. Sn coverage results in the suppression of the In 4d states. The band bending was determined similar to the other studied interfaces. From Figures 7.36 (b) and (c), one can see that in comparison to In, Sn causes a larger downward band bending of (-0.58±0.05) eV. This larger shift to higher binding can be attributed to stronger donor character of Sn with respect to In. The valence band line-shape changes upon tin deposition, which is located in the same energy region.

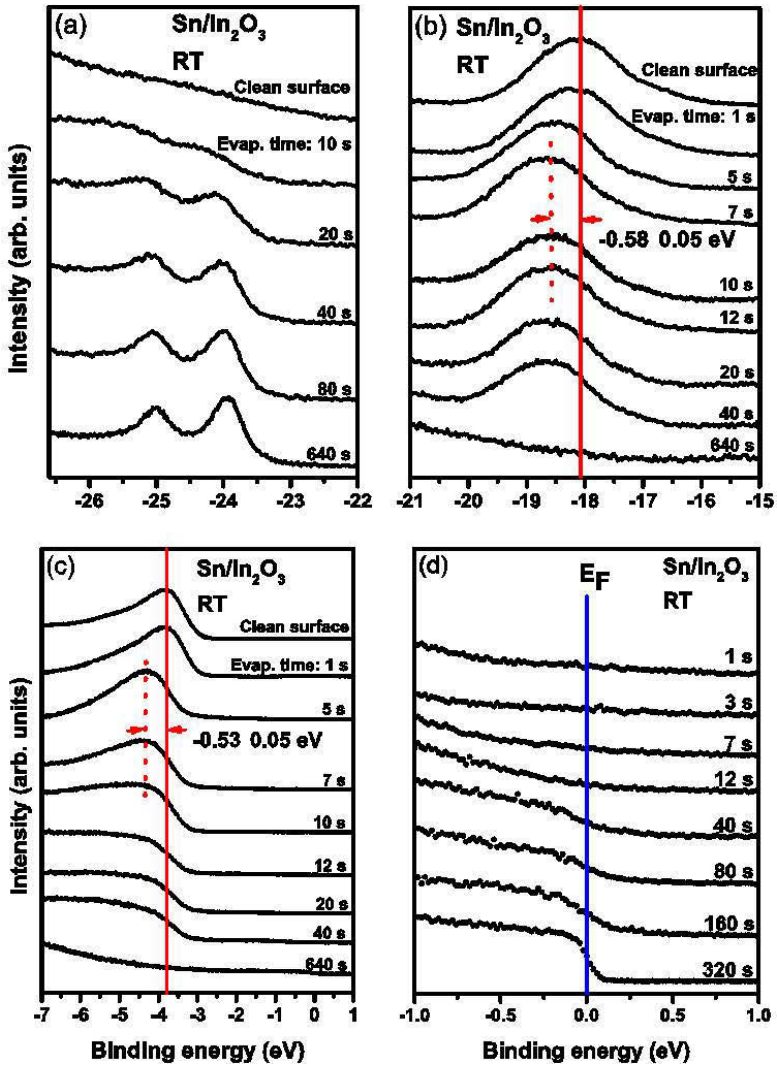

Figure 7.36: (a) Selected EDC series of the Sn 4d core level on Sn/In_2O_3 (111) interfaces at RT, two distinct spin-orbit Sn $4d_{5/2}$-$4d_{3/2}$ doublet of the metallic Sn are observable at binding energy of 24 and 25 eV for high coverages of tin. (b), (c) and (d) Selected ARPES spectra series of In 4d core level, VB and the near-E_F regions of the clean In_2O_3 (111) surface and after different evaporation times at RT.

As opposed to the In/In_2O_3, no state within the band gap could be identified in Sn-covered samples, as depicted in Figure 7.36 (d). The work function of thick layer tin on the studied crystals were determined to be (4.31±0.05) eV at room temperature, Fig. 7.37. The Schottky-Mott rule predicts an SBH of (0.13±0.11) eV, in contrast to the observed downward band bending and accordingly ohmic behavior of the interface [217].

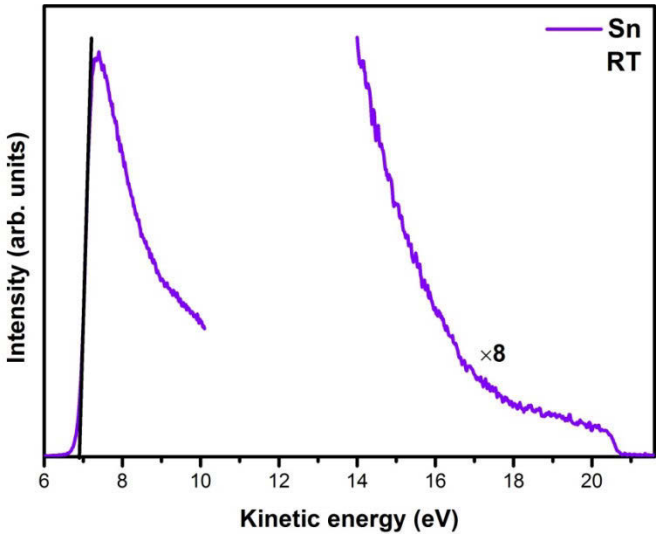

Figure 7.37: Low and high kinetic energy sides of spectra of thick Sn film at RT.

Also, Sn generates a downward band bending of (-0.53±0.05) eV at LT, Figures 7.38 (a) to (d), which is roughly similar to the room temperature results for this interface. As shown in Fig. 7.38 (d), no near-E_F state was identified at ohmic Sn/In_2O_3 interfaces at LT as well. Applying the work function of tin (4.32±0.05) eV at LT, derived from the Fig. 7.39, leading to $\Phi_{Bn}^{S\text{-}M}$ = (0.05±0.11) eV in conflict with experimental data.

Finally, the experimental results of this interface were compared with the MIGS-based model. The laterally-homogenous barrier height was found to be -1.02 eV, where the electronegativity of tin X_{Sn}=4.15 eV in Miedema unit [189]. Although this result states that the Sn/In_2O_3 is ohmic contact, this model predicts higher barrier height compared to the experimental results. As the experimentally-derived barrier heights differ from the predicted barrier heights for all examined contacts, and for the studied ones in Ref. [15] as well as ZnO interfaces [21] within this model and electronegativity concept, it suggests the improvement of the MIGS model and especially CNL concept for In_2O_3 which might be the origin of this discrepancy.

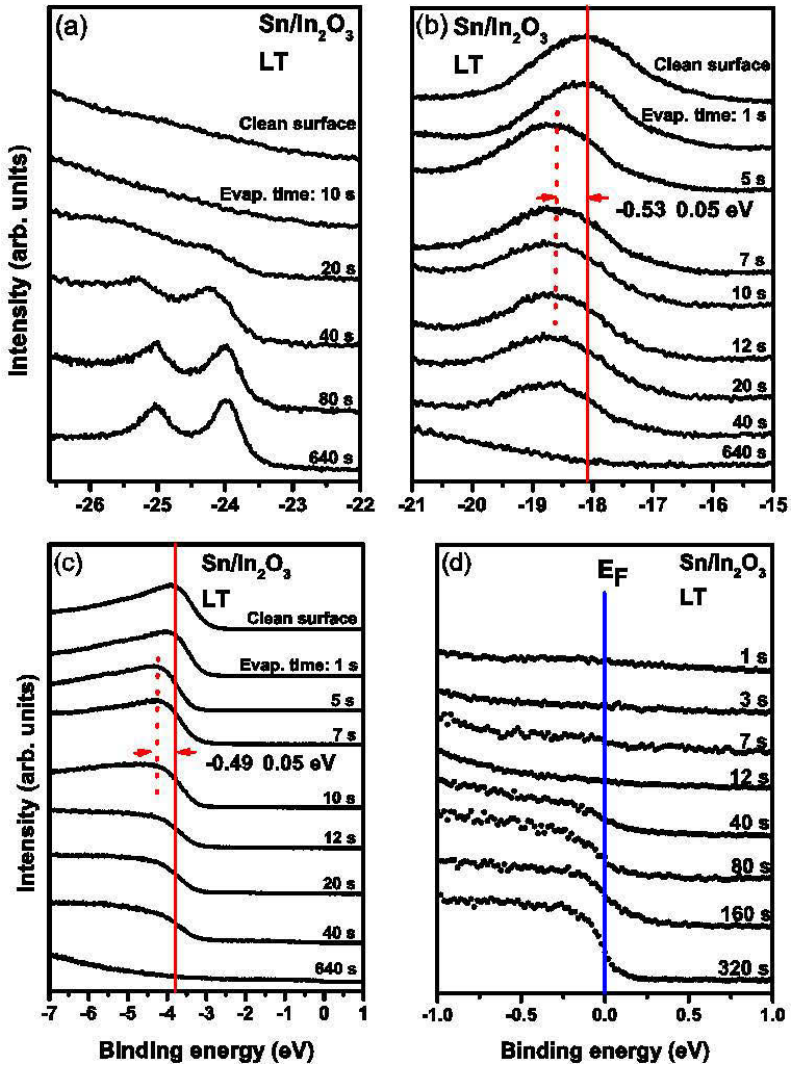

Figure 7.38: (a) Selected EDC series of the Sn 4d core level on Sn/In_2O_3 (111) interfaces at LT, and observation of two distinct spin-orbit Sn $4d_{5/2}$-$4d_{3/2}$ doublet of Sn for high thicknesses of tin. (b), (c) and (d) Selected ARPES spectra series of In 4d core level, VB and near the Fermi-energy region with Sn deposition for the contact prepared at LT.

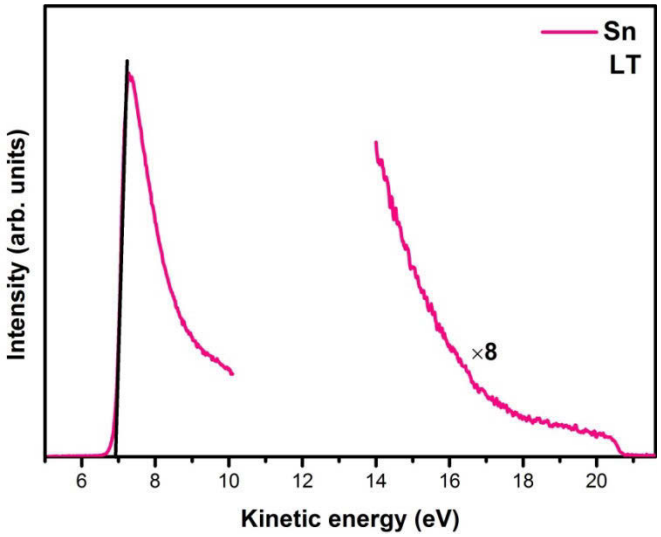

Figure 7.39: Low and high E_{kin} sides of spectra of thick Sn overlayer on In_2O_3 at LT.

7.7 Discussion of the results

As discussed earlier, transparent conductive oxides exhibit mostly unintentional n-type conductivity. The p-type doping has been commonly realized in the oxides with shallow occupied d-states such as $SrCu_2O_2$, $CuAlO_2$ and $CuCrO_2$:Mg [218-224], as opposed to most of the oxides that their VBM is mainly composed of deep lying O 2s. Therefore, identification of the p-type conduction in the typical members of this family requires probably the modification of their valence band structure. The mobility, as well as transparency of the p-type TCOs, which have been found up to now, are not as acceptable as n-type ones leading to their poor performance [225-227]. To open a perspective for In_2O_3 to be exploited as an active component in electronic devices, bipolar doping is lacked. Due to the absence of p-type In_2O_3 and consequently unavailability of its pn-homojunctions, its heterojunction with other p-type oxides such as $ZnCo_2O_4$ and NiO have been applied to fabricate bipolar devices from this oxide and showing promise of In_2O_3 functionality as an active material in bipolar diodes [228]. However, the large valence band offsets of heterojunctions between two oxides as a result of the shallow and deep locations of the VBM in p- and n-type oxides deteriorate their rectification properties [229, 230].

To accomplish this aim, the contact properties of In_2O_3 with other materials like metals should be understood to shed light on its surface and interface properties. Thus, the

electronic structure of the transparent semiconductor In_2O_3 has been studied by ARPES upon deposition of noble metals as well as metallic In and Sn. A small Schottky barrier was observed in Ag and Au/In_2O_3 interfaces with contacts prepared at RT and a larger one in Au/In_2O_3 interfaces with contact prepared at LT. Our measured-Schottky barrier heights of Au/In_2O_3 junction prepared at LT and RT are smaller than the reported one for this interface in Ref. [15]. The Au contacts were prepared on (001) surface of MBE-grown single-crystalline thin films, and a reactive sputtering process in an O_2-containing atmosphere was used prior to the contact preparation in this work [15]. The expected discrepancy in the SBH exhibits a dependence of that on sample orientation as well as surface processing which is consistent with the observed dependence of oxides electron affinity and subsequently their band alignment on the surface orientation [230-233] and also oxygen pressure [229]. By considering the contact preparation, the barrier height of Au/In_2O_3 measured in Ref. [15] is larger than ours, an effect that is compatible with the increase of the barrier due to post-annealing of metal/oxides junctions in oxidizing atmosphere [234, 235]. In contrast to the aforementioned interfaces, Cu, In and Sn/In_2O_3 contacts show ohmic behavior at both temperatures. Moreover, the downward band bending in the ohmic Cu and In/In_2O_3 interfaces was accompanied by the appearance of a surface state at initial stage of growth at RT and LT, while such state was not identified in the other ohmic Sn/In_2O_3 contact. It was demonstrated that the observed near-E_F state at Cu and In/In_2O_3 interfaces differs from previously reported-electron accumulation layer of the In_2O_3 single-crystalline thin films [8] on the basis of the different effective mass found in the present work. The 2DEG at low In and Cu coverage might be formed as a result of the defect formation. The absence of near-E_F state at low Sn-covered samples could be due to the reason that Sn does not deposit on In_2O_3 as uniformly as In and Cu. This lack of order would prevent the formation of a 2DEG at this interface. Further theoretical and experimental studies, especially characterization of the surface structure are essential to realize the origin of these states near the Fermi level at low coverage of In and Cu.

Table (7.1) summarizes the experimental barrier heights of the studied contacts and the ones derived from the Schottky-Mott rule and the model based on the metal-induced gap state concept and CNL.

The ionic semiconductors show commonly weaker Fermi level pinning in comparison with the covalent ones. The Schottky-Mott rule therefore predicts the barrier height of the interfaces on the polar-bonded semiconductors well, and as demanded by this rule the slope parameter should be around 1 at their interfaces. Although In_2O_3 is a predominantly ionic bonded semiconductor [32, 108], our measured barrier heights of metal-In_2O_3 contacts show disagreement with the deduced values from the Schottky-Mott rule as expected from the slope parameter S_x= 0.395 of In_2O_3 [15]. Additionally, the experimentally-derived barrier heights disagree with MIGS-based approach, such discrepancies have been earlier reported at In_2O_3 [15] and ZnO interfaces [21]. Even substitution of high frequency dielectric constant of In_2O_3 ε_∞=4.08 from a recently published research [230] in equation (7.5) instead of ε_∞= 4.42 from Ref. [15] resulting in a larger slope parameter of 0.44 and consequently larger negative homogenous barrier heights and discrepancies with experiment for all interfaces under study, here. Although MIGS model confirms ohmic behavior of Cu, In and Sn/In_2O_3, the obtained barrier heights via this approach are larger negative values. The comparison of our results with the obtained values based on the MIGS model indicates that the Fermi level pinning is not as strong as the one acquired by this approach. This point was also previously noted for ITO and RuO_2/Pb(Zr,Ti)O_3 and also ITO and RuO_2/Pb(Zr,Ti)O_3 heterointerfaces [229].

Incompatibility of the experimental results and predicted ones via Schottky-Mott rule as well as MIGS-based model reveals that the SBH associated with the particular chemistry and atomic structure of each interface. Therefore, theoretical calculations for each specific interface are sought for to quantify the barrier height.

If one considers the electron configuration of these metals (table 7.2), the results might be interpreted as follows:

Au and Ag act as surface acceptors and generate upward band bending (Schottky contact) by hole doping of the surface of In_2O_3, whereas In and Sn act as surface donors and cause downward band bending (ohmic contact) by electron doping of the semiconductor surface. A larger observed barrier height in Sn/In_2O_3 contacts, compared to the In/In_2O_3 ones, is consistent with its one more valence electron. However, this model does not work for Cu/In_2O_3 junctions. Cu as a noble metal should show similar behavior like Ag and Au, i.e. Schottky character, while it generates downward band

Table 7.1: Summary of the measured barrier heights and the derived ones from the Schottky-Mott rule and the MIGS model.

Interface	Substrate temperature	Φ_{Bn}^{exp} (eV)	Φ_{Bn}^{S-M} (eV)	Φ_B^{hom} (eV)	Contact type
Ag/In_2O_3	RT	(0.22±0.07)	(0.12±0.11)	-0.91	Schottky
Au/In_2O_3	RT	(0.21±0.07)	(0.67±0.11)	-0.63	Schottky
	LT	(0.36±0.07)	(0.99±0.11)		Schottky
Cu/In_2O_3	RT	(-0.14±0.07)	(0.33±0.11)	-0.87	Ohmic
	LT	(-0.13±0.07)	(0.27±0.11)		Ohmic
In/In_2O_3	RT	(-0.44±0.07)	(-0.16±0.11)	-1.12	Ohmic
	LT	(-0.42±0.07)	(-0.27±0.11)		Ohmic
Sn/In_2O_3	RT	(-0.58±0.07)	(0.13±0.11)	-1.02	Ohmic
	LT	(-0.53±0.07)	(0.05±0.11)		Ohmic

Φ_{Bn}^{exp}: Experimental barrier height. Φ_{Bn}^{S-M}: Barrier height according to the Schottky-Mott rule.
Φ_B^{hom}: Homogenous barrier height based on the MIGS approach.

bending (ohmic contact) at this interface. Despite of comparable structure of In and Sn, the absence of the free-electron like state in Sn/In_2O_3 contacts is puzzling and we ascribe it to a different growth mode of Sn on In_2O_3, since no evidence of new chemical bonding has been found in thickness-dependent core level photoemission.

Table 7.2: Electron configuration of the studied metals at metal-In_2O_3 interfaces. From [215].

Metal	Electron configuration
Ag	[Kr] $3d^{10}$ $4s^1$
Au	[Xe] $4f^{14}$ $5d^{10}$ 5 s^1
Cu	[Ar] $3d^{10}$ $4s^1$
In	[Kr] $5s^2$ $4d^{10}$ $5p^1$
Sn	[Kr] $5s^2$ $4d^{10}$ $5p^2$

Chapter 8
Conclusion

The present PhD thesis mainly deals with the study of the electronic structure of the transparent semiconductor In_2O_3 bulk single crystal by angle resolved photoemission spectroscopy (ARPES) upon stepwise deposition of noble metals (Cu, Ag and Au) as well as metallic In and Sn on the ultra-high vacuum (UHV) cleaved (111) surface of the semiconductor. High quality and purity single crystals were grown from the melt with the help of an innovative method by our partners at IKZ institute [22, 23]. Prior to the ARPES experiments, the specimens were characterized by the following analysis:

- Energy dispersive X-ray analysis (EDX) to check the composition and stoichiometry.
- Laue diffraction to study the bulk structure of the crystal and its orientation.
- Scanning tunneling microscopy under ultra-high vacuum condition to image the as-cleaved (111) surface in atomic scale of crystals, which reveals the presence of terraces with straight edges and step height of 0.28 nm at the surface and the hexagonal arrangement of the surface consistent with Ref. [101].
- Hall effect measurements to determine the temperature dependence of electron concentration of the studied crystals, which were measured by IKZS' colleagues, showing the n-type semiconductor with free electron concentration of 2×10^{17} cm^{-3} at room temperature (RT) [61]
- Energy dependence of optical transmission measurements at room temperature to acquire the fundamental band gap at this temperature: By considering the optical onset as direct forbidden transitions according to Refs. [5, 55, 141], the optical

band gap of the melt-grown crystals was derived to be around 2.79 eV in very good agreement with previous studies [4, 5, 109].

By means of ARPES the band structure was studied along two high symmetric directions Γ-P, i.e. perpendicular to the (111) surface, and Γ-N, i.e. crystallographic $[1\bar{1}0]$ directions, in valence band region, indicating accordance of the results with Scherer et al. research work [5]. However, the near-Fermi energy emission was not detected for the moderately doped samples in the present study. In order to acquire the surface band gap, the calculated value of 0.07 eV was therefore applied for the energy difference between the Fermi energy and the bottom of the conduction band. Thus, the gap was determined to be (2.87±0.1) eV at the surface in good agreement with the bulk band gap revealing the roughly flat behavior of the bands at the as-cleaved surface of the crystals and contradicting the existence of electron accumulation layer or SEAL at the pristine surface of the investigated specimens.

The barrier heights were obtained by following the band bending of the valence band and core level In 4d spectra with metal thicknesses and corrected for the photovoltage effect. The measurements were conducted for the Ag interfaces only at room temperature and for the other examined contacts at room as well as low temperature (LT). The LT-measurements were performed due to the observed evidence of the possibility of chemical reaction in Au-In_2O_3 interfaces at RT and the observation of two dimensional (2D) states at first seconds of Cu and In evaporation. A rectifying contact forms in Ag and Au/In_2O_3 interface with contact prepared at RT. A larger Schottky barrier height was detected in Au/In_2O_3 junction with contact prepared at LT. In addition to the flat behavior of the bands at the pristine surface, the Schottky character of the aforementioned interfaces as well as the induction of the surface photovoltage effect as a result of the synchrotron radiation in these contacts, verify the absence of the SEAL in the studied as-cleaved melt-grown crystals. As an accumulation layer would cause band bending at the pristine surface of a sample and also hinders Schottky-contact formation, the SEAL is not an intrinsic property of as-cleaved, melt-grown bulk In_2O_3 single crystals and likely produced by growth and post-growth treatment conditions.

The Cu/In_2O_3 demonstrated peculiarly ohmic behavior in comparison to the other noble metal-In_2O_3 contacts. Shockley-like surface states were resolved in thick Au and Cu films deposited on In_2O_3 at RT with comparable characteristic to the metal single

crystals for the case of Au compared to Cu. This identification implies the homogeneity and uniformness of the growth of metallic gold and copper on In_2O_3 at this temperature. A downward band bending of In_2O_3 core level and valence spectra by In coverage and a larger one upon Sn deposition represented that these contacts are ohmic. Ohmic Cu and In/In_2O_3 contacts were accompanied by the emergence of two dimensional electron gas (2DEG) for low coverages of the metals, whereas no 2D state was observed in the other ohmic interface Sn/In_2O_3. The near-E_F states differ from the states which were observed in the clean surface of In_2O_3 single-crystalline bulks [5] and thin films [8]. Additionally, the occupation of the CBM is excluded based on the lack of the $k_\perp$ dispersion as well as the band width of the observed 2D states.

The Schottky-Mott rule agrees well with the experimentally-derived barrier heights just for the case of Ag/In_2O_3 interface and not for the other studied contacts. Moreover, the more complicated approach based on the electronegativity concept and metal-induced gap states (MIGS) also shows disagreement with the present experimental results, indicating the complexity of contact formation mechanism in the examined interfaces.

Since Ag, Au and Cu tend to attract electrons, and In and Sn have in contrast tendency of losing them, the results can be interpreted by a simple model based on the electron configuration of the metal: Ag and Au dope the surface of In_2O_3 by holes and lead to upward band bending, whereas In and Sn donate electrons to the surface of In_2O_3 and thereby generate downward band bending. However, this model is not capable to describe the identified ohmic character of the Cu/In_2O_3 interfaces and the absence of the 2DEG in the ohmic Sn/In_2O_3 contacts. It demonstrates that some other factors should contribute to contact formation in these interfaces in addition to the electron configuration, i.e. electronegativity. The full explanation and clarification of the presented phenomena require ab initio theoretical calculations along with more surface and interface studies on this semiconductor. The realization of these findings opens promising new perspectives of In_2O_3 applications.

Bibliography

[1] T. Minami, Semicond. Sci. Technol. **20**, S35 (2005).

[2] E. Fortunato, P.Barquinha, R.Martins, Adv.Mater. **24**, 2945 (2012).

[3] A. Walsh, J. L. F. Da Silva, S.-H. Wei, C. Körber, A. Klein, L. F. J. Piper, A. DeMasi, K. E. Smith, G.Panaccione, P. Torelli, D. J. Payne, A. Bourlange, and R. G. Egdell, Phys. Rev. Lett. **100**, 167402 (2008).

[4] K. Irmscher, M. Naumann, M. Pietsch, Z. Galazka, R. Uecker, T. Schulz, R. Schewski, M. Albrecht, and R. Fornari, Phys. Status Solidi A **211**, 54 (2014).

[5] V. Scherer, C. Janowitz, A. Krapf, H. Dwelk, D. Braun, and R. Manzke, Appl. Phys. Lett. **100**, 212108 (2012).

[6] I. Hamberg, C. G. Granqvist, K. F. Berggren, B. E. Sernelius, and L. Engstrom, Phys. Rev. B **30**, 3240 (1984).

[7] P. D. C. King, T. D. Veal, D. J. Payne, A. Bourlange, R. G. Egdell, and C. F. McConville, Phys. Rev. Lett. **101**, 116808 (2008).

[8] K. H. L. Zhang, R. G. Egdell, F. Offi, S. Iacobucci, L. Petaccia, S. Gorovikov, and P. D. C. King, Phys. Rev. Lett. **110**, 056803 (2013).

[9] P. D. C. King, T. D. Veal, F. Fuchs, C.Y. Wang, D. J. Payne, A. Bourlange, H. Zhang, G. R. Bell, V. Cimalla, O. Ambacher, R.G. Egdell, F. Bechstedt, and C. F. McConville,Phys. Rev. B **79**, 205211 (2009).

[10] O. Bierwagen, J. S. Speck, T. Nagata, T. Chikyow, Y. Yamashita, H. Yoshikawa, and K. Kobayashi, Appl. Phys. Lett. **98**, 172101 (2011).

[11] S. Lany, A. Zakutayev, T. O. Mason, J. F. Wager, K. R. Poeppelmeier, J. D. Perkins, J. J. Berry, D. S. Ginley, and A. Zunger, Phys. Rev. Lett. **108**, 016802 (2012).

[12] P. Richard, T. Sato, S. Sourma, K. Nakayama, H.W. Liu, K. Iwaya, T. Hitosugi, H. Aida, H. Ding, T. Takahashi, Appl. Phys. Lett. **101**, 232105 (2012).

[13] D. R. Hagleitner et al., Phys. Rev. B **85**, 115441 (2012).

[14] C. Körber, V. Krishnakumar, A. Klein, G. Panaccione, P. Torelli, A. Walsh, J. L. F. Da Silva, S. H. Wie, R. G. Egdell, and D. J. Payne, Phys. Rev. B **81**, 165207 (2010).

[15] H. von Wenckstern, D. Splith, F. Schmidt, M. Grundmann, O. Bierwagen, and J. S. Speck, APL MATERIALS **2**, 046104 (2014).

[16] Ch. Y. Wang et al., Appl. Phys. Lett. **91**, 103509 (2007).

[17] L. C. Chen, C. H. Tien, W. C. Liao, J. Phys. D: Appl. Phys. **44**, 165101 (2011).

[18] M. Higashiwaki, K. Sasaki, A. Kuramata, T. Masui, and S. Yamakoshi, Appl. Phys. Lett. **100**, 013504 (2012).

[19] J. He, S. Xu, Y. K. Yoo, Q. Xue, H. C. Lee, S. Cheng, X. D. Xiang, G. F. Dionne, and I. Takeuchi, Appl. Phys. Lett. **86**, 052503 (2005).

[20] D. Shao, L. Qin, S. Sawyer, IEEE Photonics J. **4**, 715 (2012).

[21] M. W. Allen and S. M. Durbin, Phys. Rev. B **82**, 165310 (2010).

[22] Z. Galazka, R. Uecker, R. Fornari; J. Cryst. Growth **388**, 61 (2014).

[23] Z. Galazka, R. Uecker, K. Irmscher, D. Schulz, D. Klimm, M. Albrecht, M. Pietsch, S. Ganschow, A. Kwasniewski, and R. Fornari, J. Cryst. Growth **362**, 349 (2013).

[24] C.G. Granqvist, Appl. Opt. **20**, 2606 (1981).

[25] E.J. Gilman, and J.S. Preston, Proc. Phys. Soc. London Section B **65**, 649 (1952).

[26] C.M. Lampert, Sol. Energy Mater. **6**, 1 (1981).

[27] D. Ghosh, *Ultrathin metal transparent electrodes for the optoelectronics industry* (Springer Theses, 2013).

[28] T.P. Tyler, R.E. Brock, H.J. Karmel, T.J. Marks, and M.C. Hersam, Adv. Energy Mater., **1**, 785 (2011).

[29] S. Bae, H. Kim, Y. Lee, X. Xu, J.-S. Park, Y. Zheng, and J. Balakrishnan, Nanotechnol. **5**, 574 (2010).

[30] A. Ohtomo, and H. Y. Hwang, Nature **427**, 423 (2004).

[31] T. Minami, T. Kakumu, Y. Takeda, and S. Takata, Thin Solid Films **291**, 1 (1996).

[32] Editors: D. S. Ginley, H. Hosono, and D. C. Paine, *Handbook of Transparent Conductors* (Springer, New York Heidelberg Dordrecht London, 2010).

[33] Editors: A. Luque, and S. Hegedus, *Handbook of Photovoltaic Science and Engineering* (Wiley, New York, 2011).

[34] H. Hosono, M. Yasukawa, and H. Kawazoe, J. Non Cryst. Solids 203, 334 (1996).

[35] P. D. C. King, and T. D. Veal, J. Phys.: Condens. Matter **23**, 334214 (2011).

[36] M. Grundmann, H. Frenzel, A. Lajn, M. Lorenz, F. Schein, and H. von Wenckstern, Phys. Status Solidi A **207**, 1437 (2010).

[37] E. Fortunato, D. Ginley, H. Hosono, and D. C. Paine, MRS Bull. **32**, 242 (2007).

[38] J. B. Varley, A. Janotti, C. Franchini, and C. G. Van de Walle, Phys. Rev. B **85**, 081109(R) (2012).

[39] K. Badeker, Ann. Phys. (Leipzig) **22**, 749 (1907).

[40] P. K. Nayak, M. N. Hedhili, D. Cha, and H. N. Alshareef, Appl. Phys. Lett. **103**, 033518 (2013).

[41] B. Thangaraju, Thin Solid Films, **402**, 71 (2002).

[42] P. Ebert, Z. Zhang, F. Kluge, M. Simon, Z. Zhang, and K. Urban, Phys. Rev.Lett. **83** (1999).

[43] T. Pisarkiewicz, K. Zakrzewska, E. Leja, Thin Solid Films **174**, 217 (1989).

[44] P. Ágoston, *Point defect and surface properties of In_2O_3 and SnO_2: A*

comparative study by first-principles methods (PhD thesis, Technical University of Darmstadt, 2011).

[45] T. Yamamoto, and H. Katayama-Yoshida, Physica B **320-303**, 155 (2001).

[46] T. Yamamoto, and H. Katayama-Yoshida, J. Cryst. Growth **214/215**, 552 (2000).

[47] L. G. Wang, and A. Zunger, Phys. Rev. Lett. **90**, 256401 (2003).

[48] G. Qin, D. Li, Z. Feng, and S. Liu, Thin Solid Films **517**, 3345 (2009).

[49] J. Stankiewicz, F. Villuendas, and R. Alcalá, Appl. Phys. Lett. **96**, 192108 (2010).

[50] C. G. Van deWalle, and J. Neugebauer, Nature **423**, 626 (2003).

[51] D. G.Thomas, and J. J. Lander, J. Chem. Phys. **25**, 1136 (1956).

[52] C. G. Van de Walle, Phys. Rev. Lett. **85**, 1012 (2000).

[53] A. Janotti, and C. G. Van de Walle, Nature Mater. **6**, 44(2007).

[54] D. M. Hofmann, A. Hofstaetter, F. Leiter, H. Zhou, F. Henecker, B. K. Meyer, S. B. Orlinskii, J. Schmidt, and P. G. Baranov, Phys. Rev. Lett. **88**, 045504 (2002).

[55] P. D. C. King et al., Phys. Rev. B **80**, 081201(R) (2009).

[56] S. Limpijumnong, P. Reunchan, A. Janotti, and C. G. van de Walle, Phys. Rev. B **80**, 193202 (2009).

[57] S. F. J. Cox, J. S. Lord, S. P. Cottrell, J. M. Gil, H. V. Alberto, A. Keren, D. Prabhakaran, R. Scheuermann, and A. Stoykov, J. Phys.: Condens. Matter **18**, 1061 (2006).

[58] P. D. C. King, I. McKenzie, and T. D. Veal, Appl. Phys. Lett. **96**, 062110 (2010).

[59] T. Koida, H. Fujiwara, and M. Kondo J. Appl. Phys. **46**, L685 (2007).

[60] T. Koida, M. Kondo, K. Tsutsumi, A. Sakaguchi, M. Suzuki, and H.

Fujiwara, J. Appl. Phys. **107**, 033514 (2010).

[61] Z. Galazka, K. Irmscher, M. Pietsch, T. Schulz, R. Uecker, D. Klimm, and R. Fornari, Cryst. Eng. Commun. **15**, 2220 (2013).

[62] O. Bierwagen, Semicond. Sci. Technol. **30**, 024001 (2015).

[63] O. Bierwagen and J. S. Speck, Appl. Phys. Lett. **97**, 072103 (2010).

[64] M. D. McCluskey and S. J. Jokela J. Appl. Phys. **106**, 071101 (2009).

[65] A. Janotti and C. G. Van de Walle, Appl. Phys. Lett. **87**, 122102 (2005).

[66] S. Lany and A. Zunger, Phys. Rev. Lett. **98**, 045501 (2007).

[67] A. Janotti and C. G. Van de Walle, Nat. Mater. **6**, 44 (2007).

[68] S. M. Evans, N. C. Giles, L. E. Halliburton and L. A. Kappers, J. Appl. Phys. **103**, 043710 (2008).

[69] L. S. Vlasenko and G. D.Watkins, Phys. Rev. B **71**, 125210 (2005).

[70] R. L. Weiher, and R. P. Ley, J. Appl. Phys. **37**, 299 (1966).

[71] A. Klein, Appl. Phys. Lett. **77**, 2009 (2000).

[72] P. Ágoston, P. Erhart, A. Klein, and K. Albe, J. Phys.: Condens. Matter **21**, 455801 (2009).

[73] L. M. Tang, L. L. Wang, D. Wang, J. Z. Liu and K. Q. Chen, J. Appl. Phys. **107**, 083704 (2010).

[74] F. Tuomisto, K. Saarinen, D. C. Look and G. C. Farlow, Phys. Rev. B **72**, 085206 (2005).

[75] F. A. Selim, M. H. Weber, D. Solodovnikov, and K. G. Lynn, Phys. Rev. Lett. **99**, 085502 (2007).

[76] J. H. W. de Wit, J. Solid State Chem. **13**, 192 (1975).

[77] J. Mizusaki, H. Koinuma, J. I. Shimoyama, M. Kawasaki, and K. Fueki, J. Solid State Chem. 88, 443 (1990).

[78] G. Rupprecht, Z. Phys. **139**, 504 (1954).

[79] C. Kılıc¸ and A. Zunger, Phys. Rev. Lett. **88**, 095501 (2002).

[80] D. C. Look, J. W. Hemsky and J. R. Sizelove, Phys. Rev. Lett. **82**, 2552 (1999).

[81] A. K. Singh, A. Janotti, M. Scheffler and C. G. Van de Walle, Phys. Rev. Lett. **101**, 055502 (2008).

[82] A. Janotti and C. G. Van de Walle, Phys. Rev. B **76**, 165202 (2007).

[83] P. Erhart and K. Albe, Appl. Phys. Lett. **88**, 201918 (2006).

[84] G. W. Tomlins, J. L. Routbort and T. O. Mason, J. Appl. Phys. **87**, 117 (2000).

[85] F. Tuomisto, V. Ranki, K. Saarinen and D. C. Look, Phys. Rev. Lett. **91**, 205502 (2003).

[86] E. Korhonen, F. Tuomisto, O. Bierwagen, J. S. Speck, and Z. Galazka, Phys. Rev. B **90**, 245307 (2014).

[87] Y. S. Kim, and C. H. Park, Phys. Rev. Lett. **102**, 086403 (2009).

[88] K. G. Godinho, A. Walsh and G. W. Watson, J. Phys. Chem. C 113, 439 (2009).

[89] N. F. Mott, Can. J. Phys. **34**, 1356 (1956).

[90] N. F. Mott, Philos. Mag. **6**, 287 (1961).

[91] E. Burstein, Phys. Rev. **93**, 632 (1954).

[92] J. G. Lu et al., J. Appl. Phys. **101**, 083705 (2007).

[93] P. H. Jefferson, S. A. Hatfield, T. D. Veal, P. D. C. King, C. F. McConville, J. Zuniga-Pérez, and V. Munoz-Sanjosé, Appl. Phys. Lett. **92**, 022101 (2008).

[94] K. F. Berggren and B. E. Sernelius, Phys. Rev. B **24**, 1971 (1981).

[95] Editors: J. Jupille, and G. Thornton, *Defects at oxide surfaces* (Springer series in surface sciences, Vol. 58, Princeton Berlin Jülich, Genova, 2015).

[96] A. Walsh, J. L. F. Da Silva, and S. H. Wei, Phys. Rev. B **78**, 075211 (2008).

[97] M. Mohamed, *The electronic properties of β-Ga_2O_3* (Doctoral thesis, HU zu Berlin, 2012).

[98] H. Yamaura, T. Jinkawa, J. Tamaki, K. Moriya, N. Miura, and N. Yamazoe, Sens. Actuators B: Chem. **36**, 325 (1996).

[99] T. Takada, K. Suzuki, M. Nakane, Sens. Actuators B: Chem. **13**, 404 (1993).

[100] A. Galdikas, Z. Martunas, A. Setkus, Sens. Actuators B: Chem. **7**, 633 (1992).

[101] M. Wagner, S. Seiler, B. Meyer, L. A. Boatner, M. Schmid, and U. Diebold, Adv. Mater. Interfaces **7**, 1400289 (2014).

[102] E. H. Morales, Y. He, M. Vinnichenko, B. Delley, and U. Diebold, New J. Phys. **10**, 125030 (2008).

[103] E. H. Morales and U. Diebold, Appl. Phys. Lett. **95**, 253105 (2009).

[104] O. Bierwagen, M. E. White M E, M. Y. Tsai, and J. S. Speck, Appl. Phys. Lett. **95**, 2682105 (2009).

[105] Ch. Y. Wang, Y. Dai, J. Pezoldt, B. Lu, Th. Kups, V. Cimalla, and O. Ambacher, Cryst. Growth Des. **8**, 1257 (2008).

[106] E. J. Tarsa, J. H. English, and J. S. Speck, Appl. Phys. Lett. **62**, 2332 (1993).

[107] M. Marezio, Acta Cryst. **20**, 723 (1966).

[108] S. Zh. Karazhanov, P. Ravindran, P. Vajeeston, A. Ulyashin, T. G. Finstad, and H. Fjellvåg, Phys. Rev. B **76**, 075129 (2007).

[109] C. Janowitz et al., New J. Phys. **13**, 085014 (2011).

[110] P.W. Tasker, J. Phys. C-Solid State Phys. **12**, 4977 (1979).

[111] K. H. L. Zhang, A. Walsh, C.R.A. Catlow, V.K. Lazarov, and R.G. Egdell, Nano Lett. **10**, 3740 (2010).

[112] A. Walsh, and C.R.A. Catlow, J. Mater. Chem. **20**, 10438 (2010).

[113] R. L. Weiher, J. Appl. Phys. **33**, 2834 (1962).

[114] N. Imanakaa, T. Masuia, Y. W. Kima, and G. y. Adachib, J. Cryst. Growth **264**, 134 (2004).

[115] J. P. Remeika, and E. G. Spencer, J. Appl. Phys. **35**, 2803 (1964).

[116] *www. ww3.nd.edu*

[117] M. Eckert, Ann. Phys. **524**, 5 (2012).

[118] A. Paulheim, *Photoemission am ternären Schichthalbleitersystem* ZrS_xSe_{2-x} (Diploma thesis, HU zu Berlin, 2010).

[119] E. Preuss, B. Krahl-Urban, and R. Butz, *Laue Atlas* (Universitätsverlag Düsseldorf, 1974).

[120] G. Binning, H. Rohrer, C. Gerber, and E. Weibel, Phys. Rev. Lett. **49**, 57 (1982).

[121] J. Bardeen, Phys. Rev. Lett. **6**, 57 (1961).

[122] A. D. Gottlieb, L. Wesoloski, Nanotechnology **17**, R57 (2006).

[123] *www.ase.tufts.edu*

[124] Editors: G. Bracco, and B. Holst, *Surface science techniques* (Springer series in surface sciences, Vol. **51**, Springer-Verlag, Berlin Heidelberg, 2013).

[125] E. H. Hall, Am. J. Math **2**, 287 (1879).

[126] C. K. Poole, H. A. Farach, and R. J. Creswick, *Handbook of Superconductivity* (Academic Press, 1999).

[127] *Lake Shore 7500/9500 Series Hall System User's Manual.*

[128] P. Drude, Annalen der Physik **306**, 3 (1900).

[129] N. W. Ashcroft, and N. D. Mermin, *Solid state physics* (Harccurt, 1976).

[130] *www.academia.edu.*

[131] K. Seeger, *Semiconductor physics* (Springer-Verlag, Berlin, 1985).

[132] *www.nist.gov*.

[133] H. K. Müller, Phys. Status Solidi **27**, 723 (1968).

[134] M. Fox, *Optical Properties of Solids* (Oxford master series in condensed matter physics, 2001).

[135] D. K. Schroder, *Semiconductor material and device characterization* (A wiely-Interscience-Publication, 1990).

[136] D. F. Mott, E. A. Davis, *Electorn process in non-crystalline materials* (Clarendon. Oxford, 1979).

[137] J. Tauc, A. Menth, J. Non-Cryst Solids **8-10**, 7569 (1972).

[138] M. Moustafa, *Band Gap Engineering and Electronic Structure Study of ZrS_xSe_{2-x} Novel Materials for Solar Cell Applications* (Doctoral thesis, HU zu Berlin, 2012).

[139] M. DiDomenico, S.H. Wemple, J. Appl. Phys. **40**, 720 (1969).

[140] O. Medenbach, T. Siritanon, M. A. Subramanian, R. D. Shannon, R. X. Fischer, and G. R. Rossman, Materials Research Bulletin **48**, 2240 (2013).

[141] F. Fuchs, and F. Bechstedt, Phys. Rev. B **77**, 155107 (2008).

[142] P. Erhart, A. Klein, R. G. Egdell, and K. Albe, Phys. Rev. B **75**, 153205 (2007).

[143] H. Hertz, Ann. Physik **31**, 983 (1887).

[144] A. Einstein, Ann. Physik **17**, 132 (1905).

[145] S. Hüfner, *Photoelectron Spectroscopy principles and application* (Springer, 3rd edition, 2003).

[146] S. D. Kevan, *Angle Resolved Photoemission–Theory and Current Applications* (Elsevier Science, Amsterdam, 1992).

[147] A. Damascelli, Physica Scripta. **T109**, 61 (2004).

[148] F. Reinert and S. Hüfner, New J. Phys. **7**, 97 (2005).

[149] G. Margaritondo, Physics Today **41** (4), 66 (1988).

[150] W. Zhang, *Photoemission spectroscopy on high temperature superconductor* (Springer Science & Business Media, 2012).

[151] J. Végh. J. Electron. Spectrosc. Relat. Phenom. **151 (3)**, 159 (2006).

[152] M. P. Seah and W. A. Dench, Surf. Interf. Anal. **1**, 1 (1979).

[153] *www.helmholtz-berlin.de.*

[154] C. Janowitz, T. Zandt, Le. Dudy, R. Manzke, and G. Reichardt, Nuclear Instr. and Methods in Phys. Research A **693**, 160 (2012).

[155] J. Samson, *Techniques of Vacuum UltraViolet Spectroscopy* (Wiley, New York, 1967).

[156] L. E. Duddy, *Nature and organization of the CuO_2-plane as experimentally probed in the prototype high-temperature superconductor Bi2201* (Diploma thesis, HU zu Berlin, 2008).

[157] S. Hüfner, *Very high resolution photoelectron spectroscopy* (Springer, 2007).

[158] M. May, *Two ways of suppressing charge density waves in 1 T-$TiSe_2$* (Diploma thesis, HU zu Berlin, 2010).

[159] *PREVAC Ltd. Company -ARPES system BEST-technical manual.*

[160] S. Thürmer, *Der Einuss von Wasseradsorption auf die elektronische Struktur der Titan-Dichalkogenide* (Diploma thesis, Humboldt Universität zu Berlin, 2009).

[161] *www.Casaxps.com.*

[162] J.C.C. Fan, and J.B. Goodenough, J. Appl. Phys. **48**, 3524 (1977).

[163] I. Tanaka, M. Mizuno, and H. Adachi, Phys. Rev. B **56**, 3536 (1997).

[164] H. Odaka, S. Iwata, N. Taga, S. Ohnishi, Y. Kaneta, and Y. Shigesato, Jpn. J. Appl. Phys., Part 1 **36**, 5551 (1997).

[165] V. Brinzari, G. Korotcenkov, M. Ivanov, V. Nehasil, V. Matolin, K. Mašek, and M. Kamei, Surf. Sci. **601**, 5585 (2007).

[166] Y. Ohhata, F. Shinoki, and S. Yoshida, Thin Solid Films **59**, 255 (1979).

[167] J. Szczyrbowski, A. Dietrich, and H. Hoffmann, Phys. Status Solidi A-Appl. Res. **78**, 243 (1983).

[168] A. Bourlange, D. J. Payne, R. G. Egdell, J. S.Foord, P. P.Edwards, M. O. Jones, A. Schertel, P. J. Dobson, and J. L. Hutchison, Appl. Phys. Lett. **92**, 092117 (2008).

[169] F. Bechstedt, F. Fuchs, J. Furthmuller, Phys. Status Solidi A-Appl. Mat. **207**, 1041 (2010).

[170] H. L. Mosbacker, Y. M. Strzhemechny, B. D. White, P. E. Smith, D. C. Look, D. C. Reynolds, C. W. Litton, and L. J. Brillson, Appl. Phys. Lett. **87**, 012102 (2005).

[171] E. Defresart, J. Darville, and J. M. Gilles, Surf. Sci. **126**, 518 (1983).

[172] J. Szuber, G. Czempik, R. Larciprete, D. Koziej, and B. Adamowicz, Thin Solid Films **391**, 198 (2001).

[173] M. Noguchi, K. Hirakawa, and T. Ikoma, Phys. Rev. Lett. **66**, 2243 (1991).

[174] I. Mahboob, T. D. Veal, C. F. McConville, H. Lu, and W. J. Schaff, Phys. Rev. Lett. **92**, 036804 (2004).

[175] P. D. C. King, T. D. Veal, C. F. McConville, J. Zúñiga-Pérez, .V. Muñoz-Sanjosé. M. Hopkinson, E. D. L. Rienks, M. F. Jensen, and P. Hofmann, Phys. Rev. Lett. **104**, 256803 (2010).

[176] W. Meevasana, P. D. C. King, R. H. He, S-K. Mo, M. Hashimoto, A. Tamai, P. Songsiriritthigul, F. Baumberger, and Z-X. Shen, Nature Materials **10**, 114 (2011).

[177] A. Walsh, Appl. Phys. Lett. **98**, 261910 (2011).

[178] W. Siemons, G. Koster, H. Yamamoto, W. A. Harrison, G. Lucovsky, T. H. Geballe, D. H. A. Blank, and M. R. Beasley, Phys. Rev. Lett. **98**, 196802 (2007).

[179] A. Kalabukhov, R. Gunnarsson, J. Börjesson, E. Olsson, T. Claeson, and D. Winkler, Phys. Rev. B. **75**, 121404 (2007).

[180] F. Braun, Pogg. Ann. **153**, 556 (1874).

[181] W. Mönch, *Electronic structure of Metal-Semiconductor contacts* (Springer, Netherlands, 1990).

[182] W. Mönch, *Semiconductor surfaces and interfaces* (Springer-Verlag, Berlin Heidelberg, 1993).

[183] S. M. Sze and K. K. Ng, *Physics of Semiconductor Devices* (John-Wiley & Sons Hoboken, 3rd edition, 2007).

[184] J. Bardeen, Phys. Rev. **71**, 717 (1947).

[185] R.T.Tung, J. vac. sci. technol. B **11**,1546 (1993).

[186] W. Mönch, J. Appl. Phys. **109**, 113724 (2011).

[187] V. Heine, Phys. Rev. **138**, A1689 (1965).

[188] H. Lüth, *Surfaces and interfaces of solids* (Springer-Verlag, Berlin Heidelberg, 2nd edition, 1993).

[189] A. R. Miedema, P. F. de Châtel, and F. R. de Boer, Physica B &C **100**, 1 (1980).

[190] R. T. Tung, Phys. Rev. Lett. **52**, 461 (1984).

[191] D. R. Heslinga, H. H. Weitering, D. P. van der Werf, T. M. Klapwijk, and T. Hibma, Phys. Rev. Lett. **64**, 1589 (1990).

[192] H. Fujitani and S. Asano, Phys. Rev. B **42**, 1696 (1990).

[193] M. van Schilfgaarde and N. Newman, Phys. Rev. Lett. **65**, 2728 (1990).

[194] R. G. Dandrea and C. B. Duke, J. Vac. Sci. Technol. B **11**, 1553 (1993).

[195] R.T.Tung, Appl. Phys. Rev. **1**, 011304 (2014).

[196] D. K. Schroder, Meas.Sci.Technol. **12**, R16-R31 (2001).

[197] W. H. Brattain, and J. Bardeen, Syst. Tech. J. **321**, 1 (1953).

[198] M. Alonso, R. Cimino, and K. Horn, Phys. Rev. Lett. **64**, 1947 (1990).

[199] M. Mohamed, K. Irmscher, C. Janowitz, Z. Galazka, R. Manzke, and R. Fornari, Appl. Phys. Lett. **101**, 132106 (2012).

[200] M. H. Hecht, Phys. Rev. B **41**, 7918 (1990).

[201] H. C. Gatos and J. Lagowski, J. Vac. Sci Technol **10**, 130 (1973).

[202] *www.rsl.eng.usf.edu.*

[203] M. Nazarzadehmoafi, S. Machulik, F. Neske, V. Scherer, C. Janowitz, Z. Galazka, M. Mulazzi, and R. Manzke, Appl. Phys. Lett. **105**, 162104 (2014).

[204] M. W. Allen, S. M. Durbin, and J. B. Metson, Appl. Phys. Lett. **91**, 053512 (2007).

[205] C. T. Tsai, R. S. Williams, J. Mater. Res. **1**, 352/60 (1986).

[206] J. Hölzel and F. K. Schulte, *"Work functions of metals," in Solid Surface Physics,* Springer Tracts in Modern Physics (Springer, Berlin, 1979).

[207] J. Henk, M Hoesch, J Osterwalder, A Ernst, and P Bruno, J. Phys.: Condens. Matter **16**, 7581 (2004).

[208] W. Shockley, Phys. Rev. **56 (4)**, 317 (1939).

[209] G. Bihlmayer, O. Rader and R. Winkler, New J. Phys. **17**, 050202 (2015).

[210] J. E. Demuth, W. J. Thompson, N. J. DiNardo, and R. Imbihl, Phys. Rev. Lett. **56**, 1408 (1986).

[211] E. Cox, M. Li, P. Chung, C. Ghosh, T. S. Rahman, C. J. Jensk, J. W. Evans, and P. A. Thiel, Phys. Rev. B **71**, 115414 (2005).

[212] L. F. J. Piper, L. Colakerol, P. D. C. King, A. Schleife, J. Zúñiga-Pérez, P. A. Glans,1 T. Learmonth, A. Federov, T. D. Veal, F. Fuchs, V. Muñoz-

Sanjosé, F. Bechstedt, C. F. McConville, and K. E. Smith, Phys. Rev. Lett. B **78**, 165127 (2008).

[213] T. Ando, A. B. Fowler, and F. Stern, Rev. Mod. Phys. **54**, 437 (1982).

[214] F. Reinert, G. Nicolay, S. Schmidt, D. Ehm, and S. Hüfner, Phys. Rev. B. **63**, 115415 (2001).

[215] *www.periodictable.com*.

[216] D. R. Lide, *CRC hand book of chemistry and physics version 2008.*

[217] M. Nazarzadehmoafi, F. Titze, S. Machulik, C. Janowitz, Z. Galazka, R. Manzke, and M. Mulazzi,, Phys. Rev. B **93**, 081303 (R) (2016).

[218] H. Kawazoe, H. Yanagi, K. Ueda, H. Hosono, MRS Bulletin **2**, 285 (2000).

[219] Editors: A. Facchetti, T.J. Marks, *Transparent Electronics: From Synthesis to Application* (John Wiley & Sons, Chichester, 2010).

[220] H. Kawazoe, M. Yasukawa, H. Hyodo, M. Kurita, H. Yanagi, H. Hosono, Nature **389**, 939 (1997).

[221] K. Ueda, S. Inoue, S. Hirose, H. Kawazoe, H. Hosono, Appl. Phys. Lett. **77**, 2701 (2000).

[222] A. Kudo, H. Yanagi, H. Hosono, H. Kawazoe, Appl. Phys. Lett. **73**, 220 (1998).

[223] R. Nagarajan, N. Duan, M. K. Jayaraj, J. Li, K. A. Vanaja, A. Yokochi, A. Draeseke, J. Tate, and A. W. Sleight, Internationl Journal of Inorganic Materials **3**, 265 (2001).

[224] A. Banerjee and K. Chattopadhyay, Prog. Cryst. Growth Charact. Mater. **50**, 52 (2005).

[225] S. Sheng, G. Fang, C. Li, S. Xu, and X. Zhao, Physica status solidi (a) **203**, 1891 (2006).

[226] J. Robertson, R. Gillen, and S. Clark, Thin Solid Films **520**, 3714 (2012).

[227] H. von Wenckstern, D. Splith, S. Lanzinger, F. Schmidt, S. Müller, P. Schupp, R. Karsthof, and M. Grundmann, Adv. Electron. Mater. **1**, 1400026 (2015).

[228] J. Deuermeier, J. Gassmann, J. Brötz, A. Klein, J. Appl. Phys. **111**, 113704 (2011).

[229] A. Klein, Thin Solid Films **520**, 3721 (2012).

[230] M. Feneberg, J. Nixdorf, C. Lidig, R. Goldhahn, Z. Galazka, O. Bierwagen, and J. S. Speck, Phys. Rev. B **93**, 045203 (2016).

[231] A. Klein, C. Körber, A. Wachau, F. Säuberlich, Y. Gassenbauer, S.P. Harvey, D.E. Proffit, T.O. Mason, Materials **3**, 4892 (2010).

[232] C. Körber, P. Ágoston, A. Klein, Sensors and Actuators B **139**, 665 (2009).

[233] M.V. Hohmann, P. Ágoston, A. Wachau, T.J.M. Bayer, J. Brötz, K. Albe, A. Klein, J. Phys. Condens. Mattter **23**, 334203 (2011).

[234] R. Schafranek, S. Payan, M. Maglione, A. Klein, Phys. Rev. B **77**, 195310 (2008).

[235] C. Körber, S.P. Harvey, T.O. Mason, A. Klein, Surf. Sci. **602**, 3246 (2008).

Publications and Conferences

Papers

- **M. Nazarzadehmoafi**, F. Titze, S. Machulik, C. Janowitz, Z. Galazka, R. Manzke, and M. Mulazzi, ‘’Comparative study of the electronic structures of the In and Sn/In_2O_3 (111) interfaces’’, Phys. Rev. B **93**, 081303 (R) (2016).

- V. Scherer, C. Janowitz, Z. Galazka, **M. Nazarzadehmoafi**, and R. Manzke, ‘’Polaron character of the near-E_F band of cleaved In_2O_3 (111) single crystals’’, EPL **113**, 2 (2016).

- **M. Nazarzadehmoafi**, S. Machulik, F. Neske, V. Scherer, C. Janowitz, Z. Galazka, M. Mulazzi, and R. Manzke, ‘’Schottky contact by Ag on In_2O_3 (111) single crystals’’, Appl. Phys. Lett. **105**, 162104 (2014).

Publication in Preparation

- A. Siebert, R. Schewski, **M. Nazarzadehmoafi**, C. Janowitz, M. Albrecht, Z. Galazka, and M. Mulazzi, ‘’ Discovery of a new surface termination in β-Ga_2O_3 (100) ’’, in preparation.

Oral presentation

- **M. Nazarzadehmoafi**, A. Siebert, F. Titze, C. Janowitz, Z. Galazka, R. Manzke, and M. Mulazzi, ‘Electronic properties of metal-In_2O_3 interfaces’’, Gr_aFO_x-PhD-Workshop, Berlin, Germany, Jan. 2017.

- **M. Nazarzadehmoafi**, A. Siebert, F. Titze, C. Janowitz, Z. Galazka, M. Mulazzi, and R. Manzke, ''Peculiar electronic properties of metal-In_2O_3 interfaces'', Graduate student workshop on transparent conducting oxide semiconductors, Berlin, Germany, Nov. 2015.

- **M. Nazarzadehmoafi**, F. Titze, M. Mohamed, S. Machulik, C. Janowitz, M. Mulazzi, Z. Galazka, and R. Manzke, ''Schottky character of noble metal-In_2O_3 single interfaces'', International workshop on gallium oxide and related materials 2015, Kyoto, Japan, Nov. 2015.

- **M. Nazarzadehmoafi,** C. Janowitz, M. Mulazzi, Z. Galazka, and R. Manzke, ''Schottky and ohmic contacts on In_2O_3 (111) bulk single crystals'', Science slam, RACIRI summer school 2015, Rügen island, Germany Aug. 2015.

- **M. Nazarzadehmoafi,** C. Janowitz, M. Mulazzi, S. Machulik, Z.Galazka, and R. Manzke, ''Au-Schottky contacts on In_2O_3 single crystals'', DPG Spring Meeting, Berlin, Germany, Mar. 2015.

- **M. Nazarzadehmoafi**, S. Machulik, F. Neske, C. Janowitz, Z. Galazka, and R. Manzke, ''Barrier height of Ag on In_2O_3 (111) single crystals'', DPG Spring Meeting, Dresden, Germany, Apr. 2014.

Poster presentation

- **M. Nazarzadehmoafi**, A. Siebert, F. Titze, C. Janowitz, Z. Galazka, R. Manzke, and M. Mulazzi, ''Electronic properties of In and Sn/In_2O_3 interfaces, user meeting, Bessy II, Helmholtz zentrum, Berlin, Germany, Dec. 2015.

- C. Janowitz, V. Scherer, Z. Galazka, **M. Nazarzadehmoafi**, and R. Manzke, ''Three-dimensional polaron state at E_F in In_2O_3 single crystals'', Contribution in

poster presentation, international workshop on gallium oxide and related materials 2015, Kyoto, Japan, Nov. 2015.

- **M. Nazarzadehmoafi,** C. Janowitz, M. Mulazzi, Z. Galazka, and R. Manzke, ''Two dimensional near-E_F state at Cu and In/In_2O_3 (111) single crystals'', RACIRI summer school 2015, Rügen island, Germany Aug. 2015.

- **M. Nazarzadehmoafi**, M. Mulazzi, C. Janowitz, S. Machulik, Z. Galazka, and R. Manzke, ''Ohmic contacts to In_2O_3 single crystals'', DPG Spring Meeting, Berlin, Germany, Mar. 2015.

- **M. Nazarzadehmoafi**, M. Mulazzi, C. Janowitz, Z. Galazka, and R. Manzke, ''The noble metal-In_2O_3 interface: growth and barrier heights'', Bessy user meeting, Bessy II, Helmholtz zentrum Berlin, Germany, Dec. 2014.

- **M. Nazarzadehmoafi**, M. Mulazzi, C. Janowitz, Z. Galazka, and R. Manzke, ''Barrier height of nobel metal-In_2O_3 (111) interfaces'', Adlershof Research Forum, Berlin, Germany, Nov. 2014.

- **M. Nazarzadehmoafi**, S. Machulik, F. Neske, C. Janowitz, Z. Galazka, and R. Manzke, ''Schottky barrier height by Ag on In_2O_3 (111) single crystals'', Bessy user meeting, Bessy II, Helmholtz zentrum Berlin, Germany, Dec. 2013.

- S. Machulik, **M. Nazarzadehmoafi**, A. Siebert, M. Mohamed, C. Janowitz, Z. Galazka, and R. Manzke, ''Metal contacts on the beta-Ga_2O_3 single crystals (001) surface'', Bessy user meeting, Bessy II, Helmholtz zentrum Berlin, Germany, Dec. 2013.

Selbständigkeitserklärung

Hiermit versichere ich, die vorliegende Arbeit selbständig und ohne unerlaubte fremde Hilfe angefertigt zu haben. Ich versichere, mich nicht anderweitig um einen Doktorgrad beworben zu haben. Die dem Verfahren zu Grunde liegende Promotionsordnung der Mathematisch-Naturwissenschaftlichen Fakultät I der Humboldt-Universität zu Berlin habe ich zur Kenntnis genommen.

Maryam Nazarzadehmoafi

Berlin, den